IN VIVO IMAGING APPROACHES TO UNCOVER THE CELLULAR PATHOPHYSIOLOGY OF ISCHEMIC STROKE

Gian Marco Calandra

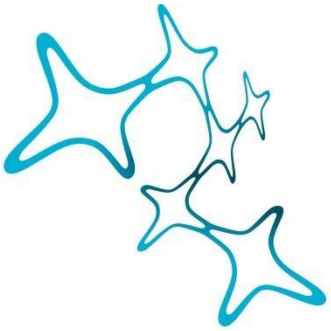

Graduate School of Systemic Neurosciences

LMU Munich

Dissertation at the
Graduate School of Systemic Neurosciences Ludwig-Maximilians-Universität München

24th of July, 2025

Supervisor and first reviewer:

Prof. Dr. med. Nikolaus Plesnila

Institute for Stroke and Dementia Research

Second reviewer:
Dr. Alessio Attardo
Leibniz-Institut für Neurobiologie

External reviewer:
Prof. Dr. Frank Kirchhoff
Saarland University

Date of Submission: 24.07.2025
Date of Defense: 27.11.2025

Table of Contents

Abstract

This work combines two complementary studies that examine the impact of focal brain injury on cortical network function. Applying *in vivo* chronic calcium imaging, we aimed to understand the circuit-level mechanisms underlying functional reorganization following stroke. Further, with the development of a novel genetic tool we provide alternative approaches to better understand cortical functional reorganization that occurs following cortical spreading depolarization (CSD)

In study I, we investigated how ischemic stroke induces contralateral cortical suppression, a phenomenon known as diaschisis. We focused on transcallosal neurons that project from the contralateral hemisphere to the site of infarction and vice versa. Applying *in vivo* chronic functional imaging, immunohistochemistry, and molecular analysis, we identified a progressive hyperactivation of contralateral transcallosal neurons following stroke, accompanied by a long-term suppression in their surrounding local circuits. Our data suggest that, while transcallosal neurons remained structurally intact, their spontaneous activity promoted maladaptive inhibitory remodeling in the contralateral cortex, resulting in reduced responsiveness to sensory input and impaired neurovascular coupling. These findings support an active model of diaschisis in which interhemispheric imbalance is perpetuated by the hyperexcitability of surviving transcallosal neurons, rather than simply reflecting passive loss of input.

In study II, we developed and validated the GluTrooper, a ROSA26 knock-in reporter mouse line expressing the glutamate sensor iGluSnFR3. In contrast to viral-based delivery methods, the GluTrooper enabled stable, widespread, and cell-type-specific expression of iGluSnFR3 across cortical and subcortical regions. Widefield glutamate imaging in awake mice confirmed reliable detection of both spontaneous and evoked glutamate release, with high signal-to-noise ratio and spatiotemporal resolution. We applied this tool to characterize glutamate dynamics during CSD, noticing the great sensitivity of our novel reporter line to enable the observation of interhemispheric inhibition that occurs following CSD. Together, these studies highlight the maladaptive mechanisms which the brain undergoes following stroke and CSD. With this work, we are acquiring a better knowledge of this compensatory mechanisms, and providing a new tool to better understand their nature.

1 Introduction

1.2 Stroke

1.2.1 Stroke epidemiology

According to several epidemiological studies, stroke is the second leading cause of death and third cause for disability worldwide [1]. In current projections, an estimated 13.7 million individuals will suffer from a stroke every year with 5.5 million deaths being recorded [1]. In terms of subtypes, ischemic strokes remain the most prevalent as it represents the two-thirds of total cases globally [1]. It is also important that the burden of stroke is not equally shared as it disproportionately impacts low to middle income countries. This can largely be attributed to the gaps in socioeconomic status along with limited healthcare infrastructure or access to preventive measures [2, 3]. Germany, being a high-income country, also reports stroke as one of the leading causes of mortality. Recent studies have shown that 340,000 stroke cases are reported annually [4]. The growing population, diabetes and atrial fibrillation also contribute to this situation in Germany [1]. Furthermore, recent studies suggest that by 2030, the estimate of people suffering from their first ischemic stroke will reach 10 million worldwide [5].

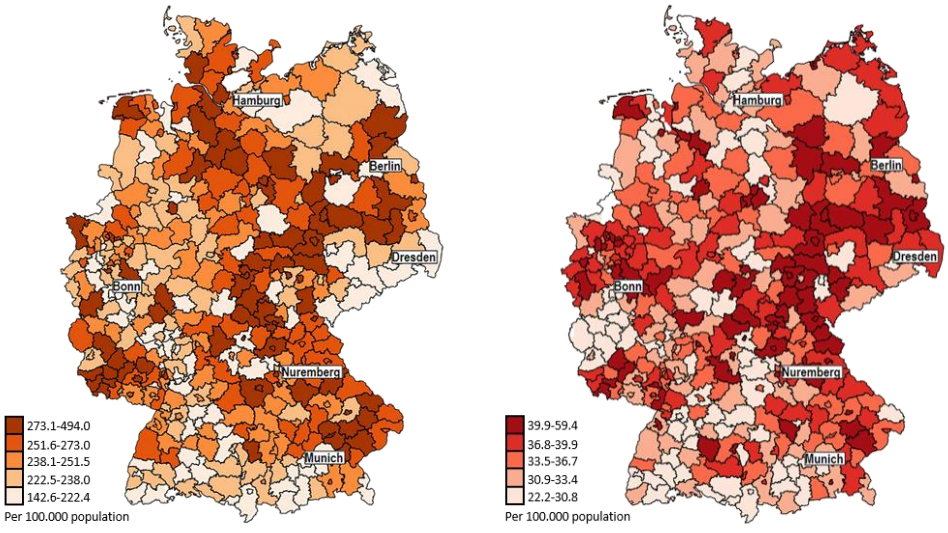

Fig 1. D*istribution of German ischemic stroke cases (on the left) and registered deaths due to ischemia (on the right) per 100.000 people. Adapted from Hans Belau et al., 2023 [6]. (Licensed under CC BY 4.0.; DOI: 10.1186/s42466-023-00232-0).*

The phenomenon of stroke recurrence remains a matter of great concern in Germany since 7.4% of patients experience a second event within the first year after their first ischemic stroke [7]. The financial burden of this issue is also considerable, with average lifetime costs per case estimated to be at €43,000 and an overall cost of €108.6 billion [8]. Despite the progress in rehabilitation services, access to care continues to differ between regions in Germany. Lifestyle-related risk factors such as smoking and physical inactivity still contribute significantly to the stroke incidence [8].

1.2.2 Pathophysiology of ischemic stroke

When blood flow into an intracranial vessel is interrupted, the brain's access to oxygen and glucose is drastically impaired, leading to severe metabolic dysfunction [9]. As described in prior studies, the infarct core is subject to irreversible injury, while the adjacent region, known as the penumbra, retains the potential for functional recovery due to collateral blood flow which keeps the tissue alive for a limited period of time [10]. Under physiological conditions, neuronal ion gradients are sustained by ATP-dependent pumps, particularly via the Na^+/K^+-ATPase pump [11]. However, when ATP levels drop due to ischemia, these gradients collapse, triggering uncontrolled neuronal depolarization, excessive neurotransmitter release, and ultimately, excitotoxicity [12, 13]. This pathological depolarization also causes calcium overload within cells, which initiates damaging cascades involving proteolytic activity and generation of reactive oxygen species [13]. While neurons in the penumbra maintain limited metabolic function [14], elevated extracellular glutamate levels from the infarct core can trigger waves of spreading depolarizations. These waves extend the area of injury by promoting glutamate-mediated toxicity [15]. As apoptosis proceeds, the penumbra experiences further disruptions, including nuclear fragmentation, chromatin condensation, and inflammatory responses [16]. In the chronic phase, typically beginning around three months after stroke, glial scar formation and tissue remodeling become prominent features [17, 18]. The glial scar plays a protective role by confining the damaged area and limiting the risk of further tissue loss or infection [19]. Despite this, the chronic phase is characterized by minimal regeneration and progressive neurodegeneration [20]. A hallmark of this stage is Wallerian degeneration, marked by the gradual breakdown of axons distal to the site of injury [21, 22]. This axonal

disconnection may impair communication between the affected region and distant, yet interconnected, brain areas, a phenomenon termed diaschisis [23].

1.3. Diaschisis

Diaschisis was introduced for the first time in 1914 by the Russian-swiss neuropathologist Constantin von Monakow. He described a phenomenon of local brain damage, with the consequent metabolic and functional deficit in anatomically separate but functional related areas to the infarct region [24]. This concept highlighted the idea that stroke-related deficits are not restricted to the damaged region, but also spread to unaffected areas.

In the early 80s, PET studies have revealed hypoperfusion and hypometabolism in distant brain regions, especially in areas with strong anatomical connections to the infarcted area [25-27]. One of the first and well documented manifestations of diaschisis is the cross cerebellar diaschisis, defined by the reduction of contralateral cerebellar activity [25]. These studies proved that diaschisis has significant implications in stroke pathophysiology and that it is not just a theoretical concept. Recent imaging studies gave a better understanding of the acute and chronic phase of diaschisis. Reduction in cerebral blood flow and neuronal activity impairment in hub regions such as thalamus and cerebellum were observed in the acute phases of diaschisis [28, 29]. Ipsilateral thalamic disfunction was observed and documented performing CT perfusion imaging, emphasizing how focal lesions perturb metabolism in functionally connected areas [30]. Diaschisis is considered as an indicator of brain malfunction, however, functional improvement is associated with the resolution of diaschisis [31, 32]. These studies proved that diaschisis can obstacle or promote functional recovery, highlighting its importance in stroke pathophysiology. Stroke pathophysiology is not limited to the direct infarct area. Diaschisis is caused primarily by Wallerian degeneration, an aberrant process characterized by axonal degradation remote from the site of injury [33]. After stroke, neurons placed in the infarcted region undergo a cascade of degenerative events that target their connecting white matter fibers tract. These events are not limited to the ipsilesional hemisphere, but extend to the contralateral hemisphere through transcallosal fibers [34]. Modern imaging approaches such as diffusion tensor imaging (DTI), have shown that contralateral

white matter undergoes degeneration following unilateral stroke [34]. These white matter structural alterations are highly correlated with neurological impairments, such as motor and cognitive deficits, highlining their crucial role in clinical outcomes [35].

Axonal degeneration promotes calcium-mediated cascades which trigger mitochondrial dysfunction and cytoskeletal breakdown within distal axons and the infarct core [36]. Notably, the preservation of contralateral white matter significantly correlates with a better functional recovery [37, 38]. In contrast, extensive degeneration of contralateral white matter fibers tract impacts neural reorganization negatively, interfering with crucial interhemispheric connections [23].

Several studies, involving functional magnetic resonance imaging (fMRI), have shown changes in contralateral connectivity following unilateral stroke, especially between homotypic regions [39, 40]. The altered contralateral connectivity is potentially mediated by the degeneration of transcallosal fibers [41]. Moreover, recent studies have shown that alterations in contralateral connectivity are confined in “hub” regions, such as sensorimotor cortex, which show increased local connectivity as a compensatory mechanism to the lack of interhemispheric signaling [42, 43]. Collectively, these studies showed the complexity of the mechanisms that are involved during diaschisis. However, diaschisis is a crucial yet poorly understood feature of stroke pathophysiology, therefore, a better understanding of its underlying cellular and molecular mechanisms is crucial for improving therapeutic options for stroke patients.

1.3.1 Promising therapies

During the last decade, various therapeutic interventions were employed to promote recovery in stroke patients, with the choice of therapeutic targets depending on the time passed from the ischemic event. In fact, acute interventions are manly focused on resolving the vascular cause through thrombolytic or anticoagulant therapy, post-acute strategies are more diverse and include molecular, neuromodulatory, and behavioral approaches. Among the most promising of these is transcranial magnetic stimulation (rTMS), a non-invasive brain stimulation technique which aims to restore functional connectivity of the lesioned hemisphere.

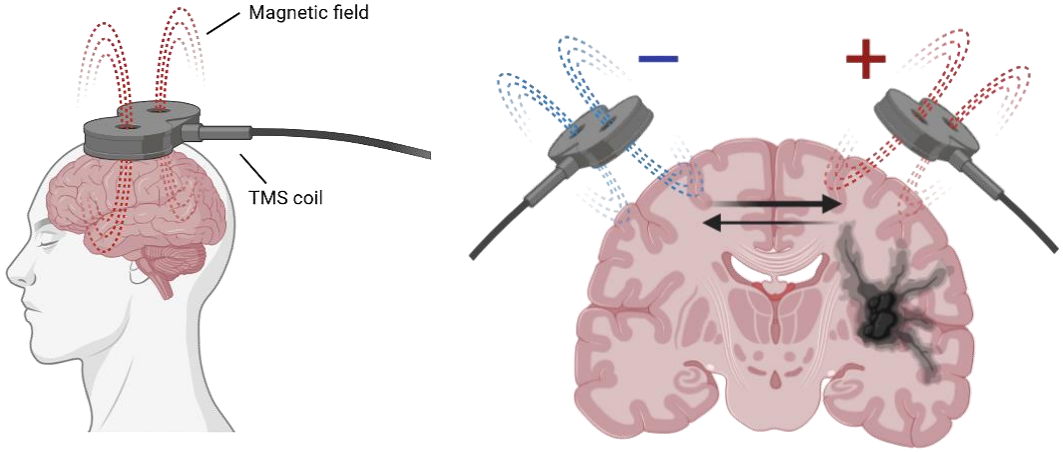

Fig 2. *Representation of TMS rehabilitation approach. The generation of the magnetic field is induced by a magnetic coil that is placed in the proximity of the unaffected hemisphere (on the left). On the right, combination of excitatory and inhibitory TMS applied respectively on the affected and unaffected hemisphere. Adapted with permission from Webster et al., 2006 [44] (License number: 6058700767299) and prepared with Biorender.com.*

After stroke, excessive inhibitory input from the unaffected hemisphere can suppress activity in the lesioned hemisphere, and TMS has been shown to restore this imbalance either by enhancing excitability in the damaged regions or inhibiting the overactive contralateral cortex [45, 46]. Compared to transcranial direct current stimulation (tDCS), TMS offers greater focality and depth of stimulation, making it efficient in modulating specific cortical circuits involved in interhemispheric inhibition. Functional improvements following TMS have been documented both acutely and over repeated

sessions, with reports of single-session gains up to 10% and cumulative improvements of 20–30% in motor evoked potential [47, 48]. In addition to TMS, molecular therapies addressing neurotransmitter balance [49] and promoting vascular or glial repair [50, 51] have been explored, as well as cell-based approaches such as neural stem cell transplantation, though the approach remains largely experimental. Behavioral interventions also play an important role. Notably, constraint-induced movement therapy (CIMT) was first demonstrated to elicit significant and enduring improvements in motor function in stroke patients, promoting long-lasting effects on motor function [52, 53]. These therapies rely on repetition to induce plasticity, a principle supported by studies showing that training, such as complex motor tasks in rodents can lead to synaptic and structural reorganization [54-56]. Furthermore, studies showed that pairing TMS with specific motor or language tasks may enhance reactivation and facilitate adaptive reorganization, as illustrated by interventions that recruit the contralesional hemisphere to support recovery in aphasia [57]. The timing of these interventions is critical, as plasticity mechanisms peak in the subacute phase post-stroke. Both animal and human studies suggest that initiating therapy around five days post-injury results in the best outcomes [58-63]. Overall, while various strategies contribute to post-stroke rehabilitation, TMS holds particular promise due to its unique capacity to rebalance cortical excitability and modulate maladaptive interhemispheric communication, offering a powerful tool for promoting recovery after stroke.

However, despite the significant clinical implementation of TMS, the mechanisms by which it produces therapeutic effects remain to be fully elucidated. In particular, the chronic functional and structural adaptations of local and transcallosal neurons in the contralateral hemisphere have not been systematically studied. This gap, precludes a mechanistic understanding of how TMS modulates interhemispheric circuits and limits the development of targeted neuromodulatory interventions. The present study aims to address this critical gap by providing a comprehensive investigation of the structural, functional, and molecular reorganization that occurs in contralateral local and transcallosal neurons following stroke. Elucidating the adaptation of these neuronal populations may offer crucial insights into the mechanisms underlying TMS efficacy and support the development of more effective, circuit-specific therapeutic strategies to support functional regeneration after ischemic stroke and other focal brain injuries.

1.4 Cortical spreading depolarization

Cortical spreading depolarization (CSD) is a neurophysiological event which involves a propagating wave of depolarization across the cerebral cortex [64]. While performing his historic experiment in 1944, Aristides Leão placed electrodes on the surface of a rabbit cortex and delivered electrical stimulation while recording bipolar electrocorticogram (ECoG) activity.

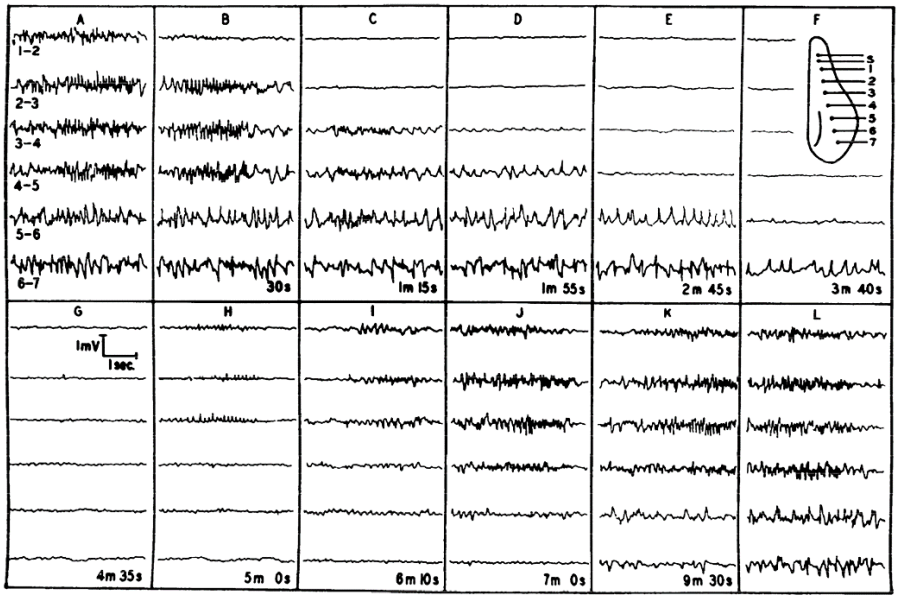

Fig 3. *Pioneering experiment conducted by Leão in 1944, representing the gradual progression of cortical spreading depression across the implanted cortical electrodes. Adapted from Leão et al., 1944 [64]. (License number: 6077020411460)*

Instead of the anticipated epileptic discharges, Leão noted a dramatic suppression of spontaneous ECoG activity. This suppression began at the point of stimulation and, following a delay, propagated slowly to adjacent areas, with recovery of activity following the same spatial trajectory. This event, later termed "cortical spreading depression," is a moving wave of cortical silencing that takes approximately 3–6 minutes [65]. The initial observation of CSD conducted by Leão suggested that this phenomenon was strictly mediated by the neuronal population. However, in vitro

studies, involving pharmacological and electrophysiological approaches, demonstrated also the astrocytic involvement in CSD propagation [66-68]. Moreover, several studies showed that the progression of CSD actively disturbs membrane resistance and ionic gradients [69, 70], and it is followed by a biphasic vascular response characterized by initial oligemia and succeeded by transient hyperemia [71]. Following the passage of the CSD wave, neurons fall into a long-lasting refractory period due to sustained depolarization above threshold levels [72]. In normal tissue, CSD does not typically result in cellular damage. However, the role of CSD in promoting harmful events stays controversial. In fact, some studies suggest that CSD could trigger effects that worse stroke recovery [73, 74]. In contrast, other studies indicate that its effect can vary depending on the pathophysiological condition and could have a neutral or protective effect [75]. After Leão's discovery, studies aimed to elucidate the molecular mechanisms of CSD. In 1956, Grafstein proposed the "potassium hypothesis", whereby neurons release excess K^+ into the extracellular space during CSD, thereby reducing excitability [76]. The concentration of extracellular K^+ depolarizes adjacent neurons and results in the slow propagation of the depolarization wave [77]. Later in 1970, van Harreveld and Fifkova shifted the attention towards neurotransmitter mechanisms and proposed that the release of extracellular glutamate could be the key mechanism of CSD initiation.

Potassium and glutamate are now considered as the major key players for CSD initiation [78-81]. Following stroke or brain injury the extracellular K^+ concentration raises above the 12 mM due to neuronal depolarization [76, 82-85]. During CSDs, extracellular K^+ concentrations may even reach 50 mmol/L [70, 84, 86-89], while extracellular levels of Na^+, Cl^-, and Ca^{2+} are significantly reduced [82, 90, 91]. Elevated focal extracellular K^+ concentrations then promote depolarization of adjacent cells, facilitating CSD initiation [76, 82]. Glutamate also contributes to CSD propagation; once released into the extracellular space, it activates NMDA and AMPA receptors, driving Ca^{2+} influx. Preclinical electrophysiological studies further reveal differential receptor roles in CSD: repetitive CSDs leave NMDA receptor responsiveness unaffected but drastically impair AMPA receptors, compromising synaptic efficacy and long-term potentiation [80].

1.4.1 Evolving strategies to monitor CSD

Among the most applied methodologies to monitor CSD, electrocorticography (ECoG) is considered the gold standard, allowing the measurement of slow potential shifts correlated to neuronal depolarization [92]. Despite its sensitivity, ECoG requires invasive electrode implantation, limiting its application in longitudinal and minimal invasive studies. In parallel, electroencephalography (EEG) has been adopted as a non-invasive method for recording neuronal activity and remains widely employed in both clinical and pre-clinical settings. However, EEG presents limitations, due to the filtering effect of the skull and dura mater, which attenuate slow voltage shifts like those produced by CSD. As a result, to avoid limitations related to signal attenuation and invasive approaches, increasing attention has been directed toward imaging-based methodologies that offer both high spatial resolution and the ability to monitor cortical dynamics with minimal invasiveness. One of those methodologies is the intrinsic optical signal imaging (IOS) which allows the monitoring of cortical neuronal circuitry by capturing fluctuations in intrinsic signals [93]. IOS is a widely applied imaging approach in pre-clinical research, providing crucial insights in cortical connectivity in physiological [94-96] and pathophysiological conditions [97-101]. IOS monitors changes in reflected light to measure fluctuations in oxy-, deoxyhemoglobin and cerebral blood flow [102, 103], promoted by different cellular populations such as neurons [104, 105] and astrocytes [106]. Due to the different absorption spectra, 540 nm for the oxy- and 660 nm for the deoxyhemoglobin, their fluctuation can be detected via light absorption [103]. Despite the high sensitivity of ECoG and the minimal invasiveness of EEG and IOS, these methodologies cannot disentangle specific aspects of neuronal activity, and therefore provide limited information about synaptic transmission as ECoG and EEG offer a general overview of bulk cortical excitability, while IOS monitors cortical responses indirectly through hemodynamic fluctuations. More recently, widefield imaging using calcium reporter transgenic lines, such as Thy1-GCaMP6 [107], has provided valuable insights into cortical connectivity under both physiological [107] and pathophysiological conditions [108]. Its application in the study of CSD offers significant advantages, combining minimal invasiveness with the ability to visualize large-scale cortical activity [108]. However, calcium imaging is limited to monitoring intracellular calcium transients and does not distinguish between excitatory

and inhibitory neurotransmission. These limitations have been addressed by the development of genetically encoded neurotransmitter sensors, such as iGABASnFR [109], iGluSnFR [110], and GRAB_NE [111], among others. These sensors enable more precise investigations of synaptic transmission in both physiological [112] and pathophysiological contexts [113, 114], providing a deeper understanding of neuronal circuit dynamics. However, so far these sensors, specifically iGluSnFR, have only been used to track changes of neuronal transmission in small tissue volumes which do not allow to draw any conclusion about the brain wide effects of CSDs, which spread over the entire cortex.

Therefore, one of the aims of the current study was to design and create a novel transgenic mouse line that expresses the genetically encoded glutamate sensor iGluSnFR3 in the whole cerebral cortex. Designed to enable minimally invasive, widefield imaging of cortical glutamate dynamics, this novel genetic tool opens new opportunities for studying excitatory neurotransmission across a range of experimental models. Its application to conditions such as stroke and CSD would demonstrate its potential to reveal how glutamatergic signaling adapts during cortical dysfunction and recovery.

1.5 Neurons

1.5.1 Morphology and physiology

In 1873, Camillo Golgi developed a technique of silver staining that enabled the histological investigation of neurons in their entirety [115] . This breakthrough provided a foundation for Santiago Ramón y Cajal to postulate that the nervous system is composed by distinct units, crucial for brain function [116]. His proposal later was termed as the “neuron doctrine” [117, 118] a crucial concept of modern neuroscience. Currently, with extensive transcriptomic and morphological research, approximately 70 different neuronal types have been identified in the human cortex [119].

Despite differences in their composition, neurons have a common architectural design. They are composed of a soma that contains the nucleus and controls metabolic functions; dendrites that manage incoming signals and an axon that transmits electrical impulses to downstream targets[120, 121]. Communication from neuron to neuron relies to a great extent on the generation of action potentials, rapid electrical events

that originate in the proximity of the soma and propagate along the axon. The spikes are of similar size and shape; their frequency and timing, however, convey specific information [122]. In order to maintain signal fidelity, action potentials are actively regenerated as they propagate along the axon. This process comes at considerable metabolic expense, occupying more than 20% of the brain's overall energy budget [123, 124]. The majority of synapses rely on chemical transmission, although some neurons communicate via electrical synapses [125] formed by gap junctions [126, 127]. In chemical synapses [128], the arrival of an action potential at the axonal terminal causes neurotransmitters to be released into a gap termed synaptic cleft. The neurotransmitters then interact with postsynaptic receptors, altering the ionic conductance and membrane potential of the postsynaptic membrane.

While this type of transmission is accompanied by a minor latency, it provides an opportunity for sophisticated modulation of the neuronal response. The major neurotransmitters in this case are glutamate [129], GABA [130, 131], and glycine [132]. Each of these neurotransmitters stimulates a distinct group of receptors; for instance, glutamate stimulates AMPA, NMDA, and kainate receptors [133-137], whereas GABA binds to $GABA_A$ [138] and $GABA_B$ receptors [139-141] and glycine stimulates glycine receptors [142]. Glutamatergic synapses are excitatory, whereas GABAergic and glycinergic synapses are inhibitory by causing hyperpolarization.

Different ions, such as Na^+, K^+ and Cl^- are crucial for the initiation and propagation of the action potential. However, Ca^{2+} stands out as a key ion responsible not only for the modulation of the membrane voltage, but also for neurotransmitter release, thereby allowing the translation of electrical signals into chemical transmission [143].

The strong involvement of Ca^{2+} in neuronal activation, brought scientist to develop Genetic Encoded Calcium Indicators (GECI) to measure neuronal activity [144, 145]. Once the presynaptic terminal is depolarized, voltage-gated calcium channels (VGCCs) open, leading to a rapid increase in intracellular Ca^{2+} concentration [146].

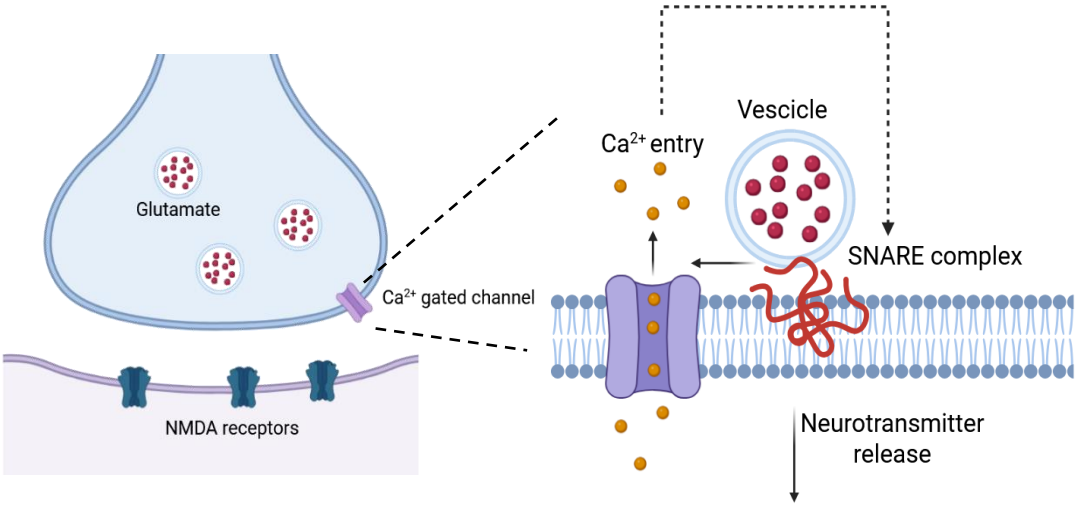

Fig. 4. *Representation of the interaction between Ca2+ and SNARE complex proteins which promotes the fusion of synaptic vesicles and the consequent release of neurotransmitters in the extracellular space. Adapted, from Catterall et al., 2008 [147]* (License number: 6058700160429) and prepared with Biorender.com.

The raise of Ca^{2+} in the cytosol of the presynaptic button, promotes its interaction with SNARE proteins, such as synaptotagmin, triggering the fusion of synaptic vesicles with the pre-synaptic membrane. This process results in the release of neurotransmitters into the synaptic cleft and transmission of information to the adjacent postsynaptic spine [143, 148].

The role of Ca^{2+} is not limited to promoting neurotransmitter release from the presynaptic terminal. In fact, upon binding of neurotransmitters to postsynaptic receptors, the intracellular Ca^{2+} concentration of activated neurons increases from 50–100 nM to 0.5–1 μM, promoting the efflux of additional Ca^{2+} ions from internal stores, such as the endoplasmic reticulum (ER) [149, 150]. This phenomenon is triggered by Ca^{2+} interaction with ryanodine receptors (RyRs) located in the ER membrane [150, 151], thereby promoting synaptic plasticity and learning [152, 153]. In the postsynaptic terminal, Ca^{2+} plays a different role, promoting dendritic excitability and gene expression regulation via glutamatergic receptors [154, 155]. The influx of Ca^{2+} into dendrites [156, 157] can promote long-term potentiation and depression [158-161]. Many studies have shown that, with long-term potentiation, morphological and

molecular changes occur in neurons, such as an increased number of AMPA receptors, which facilitate synaptic transmission [162], and an increased number of spines, therefore promoting excitability and plasticity [163]. Altogether, these functional and structural adaptations, exert a strong modulation on neuronal network function, profoundly shaping vital skills such as spatial and associative memory [164].

1.6 Approaches to measure neuronal activity *in vivo*

The shift from *in vitro* to *in vivo* measurements of neuronal activity represents an important evolution in the field of neuroscience. The groundbreaking approach of electrophysiology, involving voltage-clamp measurements, developed by Hodgkin and Huxley in the 50s [165] and refined in the 70s by Neher and Sakmann [166], allowed the observation of single-channel currents, significantly enhancing our understanding of cellular physiology [167-173]. However, the limitations of *in vitro* and *ex vivo* measurements in preserving the complex network connectivity of the brain became increasingly apparent. The need to understand neuronal circuits in their native environment, with the preservation of blood flow and the three-dimensional architecture of neuronal networks, facilitated the development of advanced microscopy methodologies, particularly two-photon microscopy introduced by Denk in 1990 [174]. This, together with the development of calcium-selective indicators [175] (e.g. BAPTA), and genetically encoded calcium/neurotransmitter sensors, such as GCaMP [176] and iGluSnFR [110], allowed scientist to gain deeper insights into neuronal activity and neuronal transmission without affecting the brain's physiological properties.

1.6.1 Two-photon microscopy

The theoretical foundation of two-photon microscopy was first proposed by Maria Goeppert-Mayer in her 1931 doctoral thesis [177], where she described the possibility that two photons could be simultaneously absorbed by a single molecule, resulting in the emission of energy in a single quantum event. For several decades, this phenomenon remained purely theoretical, as available light sources could not generate the high photon densities required for efficient two-photon absorption. It was not until 1961, with the emergence of laser technology, that Kaiser and Garrett experimentally validated the two-photon effect using a ruby laser [178].

Despite this early demonstration, the inherently low probability of two-photon absorption, characterized by absorption cross-sections typically in the range of 10^{-50} to 10^{-56} $cm^4 \cdot s$/photon, rendered the technique impractical for biological imaging until the development of mode-locked pulsed lasers. These lasers, particularly Ti:Sapphire systems, can deliver pulses with durations of ~100 femtoseconds, repetition rates around 80 MHz, and pulse energies in the range of 1–10 nanojoules. This combination of high peak intensity and moderate average power enabled sufficient photon flux to induce localized two-photon excitation, without causing significant thermal damage to biological tissue [179].

In 1990, Denk and colleagues implemented laser-scanning microscopy with two-photon excitation [174]. In this approach, infrared pulsed lasers are used to excite fluorophores via simultaneous absorption of two lower-energy photons, typically with excitation wavelengths between 700–1,050 nm, which are approximately twice the wavelength required for single-photon excitation. Because the probability of two-photon absorption scales quadratically with photon density, excitation is confined to a narrow focal volume, where photon flux is highest [180]. Ti:Sapphire lasers are widely used in this modality due to their ability to generate ultrashort pulses (~100 fs) with high repetition rates, making them ideally suited for efficient and localized excitation [180, 181]. Two-photon microscopy offers several advantages over conventional one-photon confocal microscopy. Since excitation occurs only at the focal point, there is no need for a pinhole to reject out-of-focus fluorescence, allowing all emitted light to be collected. Moreover, scattered emission photons can still contribute to the detected signal, because the excitation is highly localized [174]. This spatial restriction minimizes photobleaching and phototoxicity outside the imaging plane [182]. Additionally, the use of longer excitation wavelengths in the near-infrared range allows for deeper tissue penetration, due to reduced scattering and lower absorption by biological chromophores [183]. Today, two-photon microscopy is widely employed in combination with functional imaging techniques, such as calcium imaging and genetically encoded neurotransmitter sensors, enabling high-resolution observation of neuronal activity in both in vitro and in vivo preparations [144, 180, 184].

1.6.2 Calcium imaging

Calcium imaging is a widely employed technique that allows the optical observation of neuronal activity in real time. Since intracellular Ca^{2+} concentration rapidly increases during neuronal activation due to the crucial role of calcium in action potential dynamics, this method allows both qualitative and quantitative measurements of neuronal activity [145]. These indicators are divided into two main categories: genetically encoded calcium indicators (GECIs) and synthetic chemical dyes. Chemical dyes such as Fluo-4 are known for their fast kinetics and have been widely employed, particularly in ex vivo preparations. However, their lack of cell-type specificity and the invasiveness of their delivery (e.g. intracortical injections) have limited their utility in chronic in vivo experiments [144]. GECIs, by contrast, offer various advantages, including long-term monitoring, genetic targeting for cell-type specific expression, and minimal invasiveness once expressed. Among these, GCaMP has emerged as the most commonly used GECIs. First developed by Junichi Nakai in 2001, GCaMP is a synthetic fusion protein consisting of three domains: a circularly permuted green fluorescent protein (cpGFP), calmodulin (CaM), and the M13 peptide derived from myosin light-chain kinase [176].

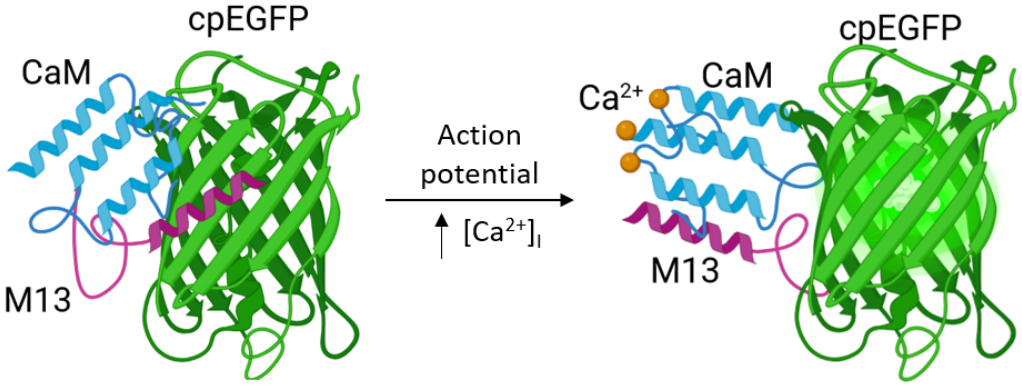

Fig 6. Schematic showing the GCaMP conformational change and fluorescence emission upon calcium binding. Adapted from Akerboom et al., 2009 [185] and prepared with Biorender.com. (Licensed under CC BY 4.0.; DOI: 10.1074/jbc.M807657200).

At low intracellular calcium levels (50–100 nM), GCaMP remains in a minimally fluorescent state due to cpGFP protonation. Upon neuronal activation, intracellular Ca^{2+} levels rise, leading to CaM–Ca^{2+} binding. This interaction induces a conformational shift that brings CaM into closer proximity with the M13 peptide, promoting the deprotonation of the cpGFP, and its enhanced fluorescence intensity [186].

The application of GECIs has revolutionized *in vivo* experimental neuroscience, enabling the simultaneous visualization of activity across large neuronal populations in living animals [144, 145]. However, calcium signals must be interpreted with caution, as Ca^{2+} influx can also occur independently of action potentials, such as through subthreshold events or receptor-mediated signaling [144]. Furthermore, chronic expression of GECIs via viral vectors can lead to cytotoxicity, especially at high expression levels or extended durations of time [187]. Despite these limitations, GCaMP remains a powerful and reliable tool for probing neuronal network dynamics with high spatial and temporal resolution [144, 145].

1.6.3 Glutamate measurements

Among the excitatory neurotransmitters in the brain, glutamate is the most prominent, promoting neuronal activation and plasticity [129]. Once released, glutamate interacts with postsynaptic NMDA and AMPA receptors [188], triggering the influx of positively charged ions such as calcium and sodium, thereby facilitating neuronal depolarization [189].

Over the last decades, the most widely used methodologies to measure neurotransmitters in living animals have been microdialysis and biochemical sensors. First conceptualized by Bito in the 60s [190] and refined by Delgado in the 70s [191], microdialysis became the gold standard for the sampling of neurotransmitters and neuropeptides in living animals [192-194]. This technique involves the implantation of a small probe presenting a semi-permeable membrane. Once the probe is inserted in the targeted brain region, a physiological solution is perfused through the probe, allowing small molecules, such as glutamate or GABA, to diffuse across the membrane from the extracellular fluid into the dialysate, which is then collected for subsequent analysis [195].

Microdialysis is not limited to detection; it also enables local drug delivery, allowing researchers to monitor drug effects in living systems [196, 197]. However, microdialysis presents several disadvantages. First, microdialysis is invasive and depending on the brain region targeted, probe insertion causes gliosis, which can reduce membrane efficiency [198, 199]. Moreover, the probe can induce local infection and inflammation [200]. Another significant drawback is the potential damage to the blood–brain barrier (BBB), which may confound experimental measurements [201, 202].

Furthermore, a key limitation of microdialysis is that sampling occurs primarily in the extrasynaptic space. Studies using the sodium channel blocker TTX have shown that microdialysis measurements of basal extracellular glutamate are largely independent of neuronal activity, suggesting contamination of the signal from non-neuronal sources [203-205].

To address the need for more direct measurement of synaptic glutamate release, researchers developed electrochemical biosensors. These consist of electrodes coated with glutamate oxidase, which catalyzes the oxidation of glutamate to α-ketoglutarate and hydrogen peroxide. The latter is detected amperometrically, producing a current proportional to glutamate concentration [206, 207]. In contrast to microdialysis, which reflects mostly tonic and extrasynaptic glutamate levels, microsensors are sensitive to TTX application, allowing for the detection of activity-dependent glutamate release [207].

Although this technique improved temporal sensitivity, early glutamate microsensors faced several limitations and required further optimization [208, 209]. In particular, issues with sensor reproducibility and false-positive signals due to interfering substances (e.g., ascorbate) presented technical challenges, especially for chronic experiments [209].

This persistent challenge underscored the need for a more robust and versatile method of glutamate detection. This need was met by the development of the intensity-based Glutamate Sensing Fluorescent Reporter (iGluSnFR), introduced by Marvin and colleagues in 2013 [110], and further refined in 2023 with the release of iGluSnFR3 [210].

iGluSnFR3 consists of a circularly permuted enhanced green fluorescent protein (cpEGFP) fused to a bacterial periplasmic glutamate-binding protein (GltI), anchored to the neuronal membrane via a PDGFR-derived transmembrane domain [210]. In the absence of extracellular glutamate, iGluSnFR3 remains in a resting, weakly fluorescent state. Upon glutamate binding, conformational changes in GltI induce a robust increase in cpEGFP fluorescence, which is proportional to the extracellular glutamate concentration [110, 210, 211].

The spatial localization of iGluSnFR3 is not random. The presence of the PDFGR peptide promotes membrane targeting with the glutamate-binding domain oriented extracellularly [210]. Additional anchoring domains, Glycosylphosphatidylinositol (GPI) and Stargazin (SGZ), further enhance spatial specificity by promoting localization to postsynaptic terminals [210].

As a result, iGluSnFR3 enables precise measurements of synaptic glutamate release, facilitating detailed study of synaptic transmission [110, 210]. Earlier versions of iGluSnFR exhibited relatively slow kinetics, with decay times in the tens of milliseconds, limiting their ability to capture rapid glutamate dynamics [110, 211]. In contrast, iGluSnFR3 demonstrates much faster kinetics, with decay times of 2–4 ms and rise times around 13 ms, enabling the detection of rapid synaptic events under both physiological and pathological conditions [184, 211, 212]. Given its improved spatial and temporal resolution, iGluSnFR3 is a powerful tool for studying cytotoxicity and glutamate dysregulation in pathophysiological conditions such as stroke or traumatic brain injury, including phenomena such as CSD [212].

At present, the expression of iGluSnFR3 can only be achieved via adeno-associated viruses (AAV). AAVs offer substantial advantages, including the ability to target specific brain regions or cell types and to monitor neuronal activity within a relatively short time after delivery. However, AAV-based approaches also present notable disadvantages. In particular, AAVs could promote cytotoxicity, disrupt endogenous signaling and trigger inflammatory responses [213-215]. To avoid these limitations, researchers have developed transgenic mouse lines that express fluorescent sensors from a defined genomic locus [107]. Such models provide stable, non-toxic expression across time and allow for longitudinal studies without the variability or adverse effects associated with viral vectors [107].

Despite the widespread adoption of iGluSnFR sensors [216-219], no transgenic mouse lines expressing the iGluSnFR have been developed. To fill this gap, the present work introduces and characterizes the GluTrooper, a novel glutamate reporter mouse line that enables the stable and widespread expression of iGluSnFR3. This model allows for high-resolution, cortex-wide imaging of glutamate dynamics under both physiological and pathophysiological conditions, offering new avenues to study excitatory neurotransmission and brain functional reorganization in living animals.

2 Aims

Despite the clinical efficacy of TMS in post-stroke rehabilitation, its circuit-level mechanisms remain poorly understood. Importantly, chronic adaptations in contralateral cortical networks, particularly in local circuits and transcallosal neurons, have not been systematically mapped in stroke pathophysiology. This gap impedes the understanding of post-stroke interhemispheric reorganization mechanisms and limits the development of targeted neuromodulation protocols or the improvement of the existing strategies. Furthermore, contemporary preclinical methodologies for the investigation of global cortical circuitry in stroke pathophysiology face significant limitations. They are confined to assessing neuronal activation via calcium reporter lines or, when examining neurotransmission, necessitate viral vector-based delivery systems, limiting the study to a restricted area and can potentially damage the system due to the side effects of AAVs.

To address this gap, the present thesis aims two main objectives:

1. To understand the molecular mechanisms underlying brain functional reorganization in stroke pathophysiology, we performed functional, structural, and molecular analyses of contralateral transcallosal and local circuits across the acute, subacute, and chronic post-stroke phases. Using longitudinal two-photon microscopy combined with viral labeling strategies, we monitored these two distinct contralateral neuronal populations for a period of three months. This approach aimed to elucidate the mechanisms underlying interhemispheric reorganization and to open new avenues for improving already existing clinical applications and to identify critical windows for effective therapeutic intervention.

2. Given the technical limitations in monitoring whole-cortex neurotransmission in preclinical research, we aimed to develop and characterize the GluTrooper, a novel transgenic mouse line expressing the genetically-encoded sensor iGluSnFR3. With this novel glutamate reporter line, we aimed to circumvents the limitations associated with AAVs delivery, such as invasive intracortical injections and potential cytotoxic effects. As the availability of transgenic lines for studying neurotransmission remains limited, the GluTrooper represents a

valuable alternative to existing calcium reporter lines, which only reflect neuronal activation rather than direct synaptic transmission. To demonstrate the broad utility of this model, we characterized the GluTrooper under both physiological and pathophysiological conditions, in order to highlight its potential applications in a wide range of experimental contexts.

3. Articles

3.1 Study I: Stroke leads to chronic contralateral neuronal suppression

Gian Marco Calandra[1,3#], Susana Valero-Freitag[1,3#], Alessio Ricci[1,3], Severin Filser[1,4], Athanasios Lourbopoulos[1], Fatma B Seker[1,3], Bernhard K Groschup[1,3], Benno Gesierich[1], Joshua J Shrouder[1,3], Antonia Wehn[1,3], Igor Khalin[1,3], Marco Düring[1,3], Martin Dichgans[1,3], Arthur Liesz[1,3], Farida Hellal[1,2,3] & Nikolaus Plesnila[1,3]

1) Institute for Stroke and Dementia Research (ISD), University Hospital, Ludwig-Maximilians University (LMU) Munich, Germany. 2) Institute for Intelligent Biotechnologies (iBIO), Helmholtz Center Munich, Neuherberg, Germany. 3) Munich Cluster for Systems Neurology (SyNergy), Munich, Germany. 4) Deutsches Zentrum für Neurodegenerative Erkrankungen (DZNE), Light Microscope Facility (LMF), Bonn, Germany

# These authors contributed equally to this study.

Abstract

Ischemic stroke induces neurological deficits not only by focal tissue damage but also through effects on distant brain areas not directly affected by ischemia, a process known as diaschisis. To elucidate the mechanisms underlying diaschisis, we developed a mouse model of diaschisis by investigating the homotypic cerebral cortex contralateral to an ischemic infarct. Biochemical and histological data indicate that deafferented contralateral transcallosal neurons connected to the infracted cerebral cortex do not undergo cell death but rather exhibit synaptic reorganization towards hyperexcitability, while contralateral neurons not connected to the infarcted brain display a shift towards a more inhibitory phenotype within three months after stroke. On the functional level, longitudinal in vivo Ca^{2+} imaging revealed that transcallosal neurons become hyperactivated after stroke, thereby inducing a widespread inhibition in surrounding, local neuronal populations. This process results in a long-lasting decrease in cortical perfusion, a clinical hallmark of diaschisis. The identification of this maladaptive process in the contralateral hemisphere may provide new avenues for the treatment of chronic neuronal dysfunction following focal brain injuries.

Introduction

Neurons communicate both locally and across distant networks. As a result, the effects of focal brain injuries, e.g., caused by cerebral ischemia or trauma, extend far beyond the immediate site of damage. This phenomenon, termed "diaschisis" by Constantin von Monakow in the early 20th century, manifests as impairment of neurological function in anatomically distinct but functionally related brain areas[1]. Although imaging studies have documented diaschisis in stroke patients by demonstrating hypoperfusion and hypometabolism in contralateral brain regions[2], the underlying cellular and molecular mechanisms are only poorly understood.

To study long-range neuronal connections in the cerebral cortex transcallosal neurons mediating interhemispheric inhibition across the corpus callosum[3] represent a good model system[4,5], but biochemical and functional studies specifically addressing the effect of a focal injury on distant neuronal populations are largely missing. To fill this gap, we performed morphological and biochemical analysis and stained contralateral transcallosal and local neuronal networks genetically and with adeno-associated viruses and imaged these cells longitudinally for up to three months after cerebral ischemia by in vivo two-photon microscopy. Our results suggest that neurons losing their projections due to a distant focal injury do not die but undergo synaptic reorganization thereby suppressing their local network and causing a phenotype compatible to diaschisis in patients.

Results

Experimental stroke leads to contralateral cortical thinning

To investigate whether ischemic stroke affects distant brain areas, i.e. the contralateral hemisphere, we used MRI to assess atrophy of the brain up to three months after inducing stroke via filament MCA occlusion, which induces large strokes including the cerebral cortex and the basal ganglia (fMCAo; Fig. 1A). We observed volume reductions in both ipsilateral (-32%) and contralateral (-11%) hemispheres (Fig. 1B). To assess whether these structural changes were driven by brain areas known to be connected to the contralateral hemisphere through specific pathways, e.g. the cerebral cortices which are homotypically connected through transcallosal projections, we measured the thickness of the contralateral cortex following distal MCA occlusion, a stroke model which induces isolated cortical infarcts (dMCAo, Fig. 1A). Indeed, isolated cortical infarcts induced a reduction of the homotopic contralateral cortex by 10% (Fig. 1C) suggesting that the loss of ipsilateral projection fields by the ischemic lesion caused atrophy of the connected contralateral cortex. These findings demonstrate that ischemic stroke lesions induce structural changes, i.e. atrophy, in the contralateral hemisphere, thereby providing us with an experimental model to study diaschisis.

Stroke triggers contralateral neuropil atrophy without neuronal loss

Based on these findings we hypothesized that the contralateral atrophy following stroke is caused by the loss of neurons due to retrograde degeneration. To test this hypothesis, we counted neurons in the contralateral barrel cortex, the homotopic region of the infarct, and examined the size of neuronal somata. We found no significant changes in neuronal density (Fig. 2A) or distribution of neuronal cell soma size (Fig. 2B), indicating that no retrograde degeneration occurred and the contralateral neuronal network was preserved.

Consequently, we hypothesized that the observed contralateral atrophy after stroke must be caused by a reduction of the volume of the neuropil, which contains axons and dendrites. Binarization and segmentation of all cellular structures in the homotopic contralateral cortex allowed us to quantify the neuropil volume (Fig. 2C) and revealed a 14% reduction in neuropil volume two month after dMCAo (Fig. 2D). These findings

suggest that contralateral atrophy after stroke does not result from retrograde degeneration and death of neurons disconnected from their infarcted projection fields, but rather from changes in the surrounding neuropil.

Ischemia induces corpus callosum atrophy

Based on the conclusions drawn from these data, only contralateral neurons actually connected to the infarcted hemisphere should be affected by the observed changes. For the next step we therefore aimed to focus our investigation to this specific neuronal population. Fist, we labeled all neurons of the cortex contralateral to the infarct by injecting an adeno-associated virus (AAV) which induced the expression of a green fluorescent protein under a neuronal promoter (AAV1-hSyn-EGFP; Addgene 37825-AAV1) into the contralateral barrel cortex (Fig. 3A) and investigated the transcallosal projections of these specific neurons three months after ischemic stroke. Our analysis revealed multiple local axonal swellings suggestive of classical axonal dystrophy along the corpus callosum (Fig. 3B). Consequently, the thickness of the ipsi- and contralateral corpus callosum was significantly reduced by about 25% after stroke as compared to sham-operated controls (Fig. 3C). These findings support our hypothesis that ischemic damage causes disconnection of contralateral transcallosal neurons, leading to callosal and contralateral cortical atrophy. To investigate contralateral transcallosal neurons connected to the ischemic lesion more specifically, we labelled them with GFP by injecting a retrograde AAV (rAAV-CAG-GFP; Addgene 37825-AAVrg) into the future infarct site one month before ischemia (Fig. 3D). This approach allowed us to specifically label only those contralateral neurons which indeed projected into the infarct (Fig. 3E). When investigating these neurons three month after stroke, we realized that their number was unchanged (data not shown), as well as their soma size, although some transcallosal neurons appear to be atrophic three months after stroke (Fig. 3E). These data indicate that neurons of the contralateral hemisphere sending transcallosal projections into the infarct area could become slightly atrophic three months after stroke, but otherwise stay alive and may still be functional.

Excitation-inhibition imbalance in the contralateral cortex following stroke

In a first step to investigate the functional properties of deafferented transcallosal contralateral neurons, we determined the inhibitory/excitatory ratio of their synaptic connections. We specifically identified the dendritic arbor of deafferented transcallosal contralateral neurons by their GFP expression and quantified the dendritic spines contacted by excitatory (vGlut1-positive) or inhibitory (Gad65-67-positive) presynaptic axonal boutons using immunohistochemistry and high-resolution Airyscan confocal microscopy (Fig. 4A). Disconnected transcallosal neurons of the contralateral hemisphere showed significantly fewer Gad65-67-positive boutons compared to non-disconnected neurons three months after stroke (Fig. 4B), while vGlut1-positive boutons increased (Fig. 4C). The excitatory/inhibitory synapse ratio nearly doubled in disconnected transcallosal neurons (Fig. 4D), indicating a substantially increased excitability of these cells after ischemia.

To determine whether the hyperexcitability of disconnected transcallosal neurons influences the surrounding neuronal network, we quantified inhibitory and excitatory presynaptic boutons in the homotopic area contralateral to the infarct up to ninety days post-stroke or sham-surgery (Fig. 4E). Quantification of synaptic markers at one, seven, fourteen-, and ninety-days post-stroke revealed dynamic changes in synaptic composition (Fig. 4F, G). At twenty-four hours post-insult, we observed a general loss of both inhibitory and excitatory synapses, indicative of acute disconnection between the contralateral and infarcted hemispheres. Synaptic markers normalized by day seven, followed by a doubling of inhibitory Gad65-67-positive synapses at ninety days post-stroke (Fig. 4F). Concurrently, vGlut1-positive excitatory synapses decreased by more than 50% (Fig. 4G). Hence, at ninety days post-ischemia, we observed a network-wide increase in inhibitory (Gad65-67^{+}) synapses throughout layers II-V of the contralateral cortex, accompanied by a decrease in excitatory (vGlut1^{+}) synapses. Changes in synaptic balance were accompanied by alterations in mRNA expression of GABA receptor subunits associated with phasic (α1-3 and γ2) and tonic (α4-5 and δ) inhibition (Fig. 4H, I). At twenty-four hours post-stroke, both phasic and tonic subunits decreased in ipsilateral and contralateral hemispheres. By ninety days, phasic inhibition normalized to sham levels bilaterally, while tonic inhibition increased

contralaterally (Fig. 5I). These data are fully in line with our immunohistochemical data and suggest that the disconnection and subsequent hyperexcitability of contralateral transcallosal neurons may trigger a network-wide reorganization towards increased tonic inhibition in the surrounding neuronal network.

Stroke causes hyperactivation of contralateral transcallosal neurons

To characterize the excitation-inhibition imbalance observed in the contralateral hemisphere on the functional level, we quantified the activity of transcallosal and local contralateral neurons by measuring changes of the intracellular calcium concentration $[Ca^{2+}]_i$ using Thy1-GCaMP6s transgenic mice [107] and *in vivo* multiphoton imaging (Fig. 5A, left panel). To be able to identify transcallosal neurons, a retrograde AAV inducing the expression of tdTomato under the ubiquitous CAG promoter (Addgene, 59462-AAVrg) was injected into the prospective stroke area (Fig. 5A, left panel). Following a two-week recovery period and a two-week training phase to acclimate mice to the awake imaging setup (Fig. 5A, right panel), we performed baseline imaging. Mice were then subjected to dMCAo, and the same regions of interest (ROIs) were tracked for three months post-ischemia. Cortical neurons were identified by the green fluorescence of the genetically expressed Ca^{2+} sensor (GCaMP6s) (Fig. 5B, arrow 3), while double labelling with tdTomato identified transcallosal neurons (Fig. 5B, arrow 1). Using this approach, we observed an obvious increase in the number of spontaneous calcium transients in transcallosal neurons twenty-one days after stroke as compared to the baseline recorded in the same mice before stroke. Neurons without transcallosal connections did not show any changes in spontaneous neuronal activity (Fig. 5C). Quantification of the data using an investigator-independent script for peak detection, revealed a more than two-fold increase (+126%) in the number of spontaneous calcium transients in transcallosal neurons of mice subjected to stroke as compared to those who underwent sham surgery (Fig. 5D). The amplitude of the $[Ca^{2+}]_i$ events was not changed suggesting that the generation of action potentials was not affected (Fig. 5E). No changes in spontaneous activity were observed in local transcallosal neurons, i.e. those cells without transcallosal connections to the infarct area (Fig. 5F&G). Together with our previous immunohistochemical and biochemical

findings our functional data clearly indicate that contralateral transcallosal neurons become hyperactive in the chronic phase after ischemic stroke.

Stroke triggers chronic weakening in contralateral neuronal response

To understand whether the observed hyperactivity of transcallosal neurons affects the function of the local neuronal network, we monitored activity-dependent intracellular Ca2+ transients in transcallosal and local neurons of the hemisphere contralateral to the ischemic infarct (Fig. 6A). Neuronal activation by whisker stimulation resulted in a robust increase in the number of Ca transients in the barrel cortex (Fig. 6B) which lasted for the duration of the stimulation, i.e. 20s (Fig. 6C). Observing the evoked contralateral neuronal activity, we noticed that whisker stimulation increased the number of Ca^{2+} transients in the majority of the neurons, however, the response was significantly diminished over time after stroke (Fig. 6D). Notably, we observed a progressive weakening in the induced global neuronal response which reached a highly significant reduction of 36% 2.5 months post-stroke (Fig. 6E). In contrast, contralateral transcallosal neurons did not exhibit a significant change in activity upon whisker stimulation as compared to baseline (Fig. 6F). These findings are well in line with the observed global increase in GAD65-positive synapses in the contralateral barrel field three months after cerebral ischemia by immunohistochemistry. Collectively, these findings support the concept that injury to one cerebral hemisphere induces hyperactivity of transcallosal neurons which then induce global inhibitory remodeling of local neurons in the contralateral hemisphere. Accordingly, our data suggest that hyperactive transcallosal neurons are the cellular mechanisms underlying diaschisis.

Stroke induces chronic impairment of neurovascular coupling in the contralateral hemisphere

To investigate whether the inhibitory remodeling of the contralateral cortex induces changes in local cortical perfusion, the main characteristic of diaschisis, we measured cortical cerebral blood flow (CBF) in response to whisker stimulation by laser speckle contrast imaging repetitively for up to ninety days post-stroke (Fig. 6A). We generated

high-resolution heat maps to analyze the spatiotemporal evolution of CBF responses. At 5 days post-ischemia, the CBF response remained unchanged compared to sham controls. However, by day 14, neurons in the contralateral barrel field exhibited a stronger response, aligning with the increased expression of vGlu1-positive boutons in this region. This enhanced response persisted until one-month post-stroke. Strikingly, at three months post-stroke, whisker stimulation induced a significantly lower CBF response in the barrel cortex and surrounding areas compared to controls (Fig. 6B) as also shown by quantitative analysis. These findings support the chronic weakening of neuronal responses observed in our *in vivo* calcium imaging data and the overexpression of GAD65-67 positive synapses observed in the contralateral barrel field column at ninety days following stroke.

Discussion

In the present study, we investigated the cellular and molecular mechanisms underlying diaschisis, the changes occurring in anatomically separate but functionally related brain areas after ischemic stroke. Using two different experimental models of cerebral ischemia, we found that ischemic stroke, in the chronic phase, is characterized by atrophy of the ipsilateral, and the contralateral brain area homotopic to the infarct. The contralateral atrophy was followed by a reduction in neuronal activity, mirroring diaschisis observed in stroke patients[1]. We reveal that the cellular and molecular substrate of diaschisis is induced by the disconnection of contralateral transcallosal neurons from their projection area, which then remodel their dendrites towards hyperexcitability. Our results suggest that both ischemia-induced tissue damage and remodeling of disconnected transcallosal neurons contribute to functional deficits after stroke. While some elegant studies have focused on tissue atrophy in the ischemic hemisphere after stroke or brain injury[7], few studies have addressed changes in distant brain areas, particularly the contralateral hemisphere[8,9]. Our study expands these observations to the contralateral hemisphere, demonstrating that cortical infarcts trigger contralateral cortical thinning through the disconnection of transcallosal neurons. Using viral labeling strategies to mark contralateral transcallosal neurons, we observed morphological evidence of disconnection, including dystrophy and retraction bulbs along the corpus callosum up to three months post-stroke, in line with previous reports[10]. Importantly, this disconnection did not result in death of the transcallosal neurons in the homotopic contralateral cortex, as evidenced by the lack of significant changes in neuron density or soma size distribution.

Our in vivo calcium imaging experiments provided crucial details into the temporal dynamics of neuronal activity changes in the contralateral hemisphere. We observed a chronic elevation in calcium events in disconnected transcallosal neurons, compared to sham operated animals. This hyperactivation was specific to the transcallosal population and not observed in the global neuronal population, suggesting that stroke induces a targeted effect on inter-hemispheric communication pathways. These findings corroborate recent studies demonstrating that, following a lesion, contralateral transcallosal neurons undergo hyperactivation due to reduced inhibitory modulation from the affected hemisphere[8,9]. The observed hyperexcitability was observed not only

functionally, but also structurally. In fact, we found that ischemic stroke affects inhibitory input in disconnected transcallosal neurons, as evidenced by an increased ratio of vGlut1/GAD65-67 on existing synapses three months post-ischemia. This enhanced presynaptic excitability may have been triggered by decreased contralateral GABAergic inhibition due to retrograde degeneration of transcallosal neurons projecting from the infarcted tissue[11,12].Our calcium imaging data revealed a progressive weakening in the global neuronal response to whisker stimulation in the contralateral hemisphere, starting at twenty-one days post-stroke, supporting our post-mortem quantifications showing an increase in GAD65-positive synapses within the contralateral barrel field at ninety days post-ischemia. The discrepancy between the hyperactivation of transcallosal neurons and the weakened response of the global neuronal population suggests a complex remodeling of the contralateral cortical network. These findings show a biphasic reorganization underlying diaschisis. Initially, we observed a period of global contralateral hyperexcitation after stroke, followed by decreasing activity and even hypoactivation of the contralateral cortex, as assessed by functional hyperemia at three months post-stroke. This aligns with human data assessed during the same time window after stroke by fMRI and finger-thumb opposition task[13]. The enhanced activation occurring early after stroke may contribute to partial symptom resolution through potentiation of uncrossed cortical pathways. However, also the hyperactive contralateral cortex could inhibit the function of the damaged cortex[14]. This hypothesis has led to therapeutic approaches using inhibitory neuromodulation in humans[14]. The strength of interhemispheric inhibition has been found to correlate with motor impairment, and reducing contralateral excitability has been shown to promote hand function recovery[15]. Our results have important implications for therapeutic approaches to stroke recovery. The biphasic nature of the contralateral cortex reorganization suggests that inhibition of hyperexcitation may be therapeutically useful in the first weeks after focal injury. However, months later, excitation may be the more beneficial approach. This concept is supported by failed therapeutic attempts with inhibitory drugs in chronic stroke patients[16,17]. Our current findings explain why attempts to inhibit contralateral cortex activity and restore neurological function were not effective after focal brain injury[18].

In conclusion, our study shows that contralesional cortical atrophy following ischemic stroke results from the remodeling of transcallosal neurons that lose their axonal

projections. These neurons become hyperexcitable thereby promoting overall inhibitory remodeling in the surrounding neuronal network. Our findings elucidate the cellular and molecular basis of diaschisis and emphasize the need for therapeutic interventions that account for the biphasic temporal profile of post-stroke reorganization. This approach could potentially alleviate chronic functional impairments following stroke and other focal brain injuries.

Methods

Animals

C57BL/6J and Thy1-GCaMP6s mice, aged 2-4 months, were used in this study. The animals were group-housed (4-5 mice per cage) under specific-pathogen-free conditions in the animal facility of the Center of Stroke and Dementia Research. Mice were maintained on a 12/12-hour light/dark cycle at 21 ± 1°C with ad libitum access to standard laboratory chow and water. All experiments were conducted in accordance with the ARRIVE guidelines and approved by the German National Guidelines for Animal Protection. Experimenters were blinded to group allocation during data collection and analysis.

Stroke models

Stroke models were implemented using two distinct procedures: distal middle cerebral artery occlusion (dMCAo) for permanent focal cerebral ischemia, and filament middle cerebral artery occlusion (fMCAo) for transient cerebral ischemia. For both procedures, mice were anesthetized with 4% isoflurane (balanced with 30% O2 and 65% N2), maintained at 1.5-2% isoflurane throughout surgery, and body temperature was kept at 37°C using a feedback-controlled heating pad. Analgesia (Buprenorphine, 100µg s.c) was administered 30 minutes pre-surgery. For dMCAo model, the skull was exposed via skin excision, and a burr hole was drilled in the temporal bone. The middle cerebral artery was permanently occluded using high-frequency electrocoagulation forceps. For fMCAo, the left middle cerebral artery was occluded for 60 minutes using a silicon-coated filament (#701912PK5Re, Doccol), followed by reperfusion. Occlusion was confirmed by monitoring decreased regional cerebral blood flow with a laser Doppler probe fixed above the MCA territory. Vital parameters were monitored via pulse oximeter. Post-procedure care for both models included wound treatment with Povidone-iodine, suturing, and subcutaneous saline injection (1 ml). Mice were placed in a 32°C recovery chamber until full motor function returned, then transferred to home cages with ad libitum access to water and food. Sham surgeries followed identical procedures without MCA occlusion.

Ex vivo MRI imaging

Ex vivo MRI was performed using a 3T nanoScan® PET/MR system (Mediso, Münster, Germany) equipped with a cryogen-free 3 Tesla magnet (bore size 2350 mm, >450mT/m maximum gradient) and a 42 mm internal diameter quadrature mouse body coil. Brains stored in PBS were secured in custom-made holders during scanning. Coronal T2-weighted images (T2WI) of the entire cerebrum were acquired using a 2D fast-spin echo (FSE) sequence with the following parameters: TR/TE = 3000/65.3ms; 17 averages; matrix size = 272 × 272; field of view = 38 mm × 38 mm; resolution 140 x 140 x 660 µm³. Stroke lesion areas were identified on T2WI, and ipsilateral and contralesional hemispheric volumes were manually measured on 12 consecutive sections using ImageJ software (polygon tool; NIH). Volumes were calculated using the equation: $V = d*(A_1/2 + A_2 + A_3 + ... + A_n/2)$, where d is the inter-section distance in mm and A is the measured area. Three-dimensional reconstructions of representative MRI images were generated using Imaris software.

Brain thickness and neuropil fraction measurements

To assess brain atrophy, we measured the thickness of the contralesional cortex and corpus callosum at bregma 0, -0.5, and -1.5mm levels in Nissl-stained sections. Sections were air-dried overnight, incubated for 45 minutes at 60°C in 0.05% Cresyl fast violet/0.05% acetic acid solution, differentiated through graded alcohols, cleared in xylene, and coverslipped with DPX. Cortical thickness was evaluated by placing 15 perpendicular lines from white matter to pial surface across the sensorimotor cortex, including primary visual, primary motor, and lateral entorhinal cortices, using a 5X objective. Corpus callosum surface area was measured bilaterally at bregma level as previously described. Measurements were averaged across three sections per animal for statistical comparisons between groups.

Neuropil fraction, an indirect measure of connectivity, was quantified in layers II/III of the homotopic region to the lesion. High-resolution images of Nissl-stained sections were inverted, converted to 8-bit, and binarized using ImageJ software. The non-stained area, representing neuropil space containing glial and neuronal processes, was extracted and quantified. Results are expressed as mean cortical thickness (µm),

corpus callosum surface coverage, and neuropil fraction. All analyses were performed by experimenters blinded to the experimental conditions, and measurements were averaged across three sections per animal for statistical comparisons.

Cell density and soma size

To assess neuronal density and morphology, we analyzed three coronal brain sections (bregma 0, -0.5, and -1.5 mm) immunostained for NeuN and counterstained with DAPI. Four regions of interest per section were delineated in layers II/III and V of the contralesional cortex, homotopic to the lesion site. Neuronal counts were performed manually identifying NeuN-positive cells. Neuronal soma size was quantified by tracing cell bodies using ImageJ software (NIH). The frequency distribution of neuronal soma sizes was subsequently analyzed using Microsoft Excel.

AAVs and stereotactic injections

We used several AAVs for specific labeling and imaging purposes. The following table summarizes the viral constructs, their injection sites, and their reference:

Viral vector	Injection site	Reference
AAVrg-CAG-eGFP	Ipsilateral hemisphere	Addgene: 37825-AAVrg
AAV1-CAG-eGFP	Contralateral hemisphere	Addgene: 37825-AAV1
AAVrg-CAG-tdTomato	Ipsilateral hemisphere	Addgene: 59462-AAVrg

For all injections, a total volume of 0.5µl of viral suspension (diluted 1:10 in PBS to a final concentration of 1x10^12 vg/ml) was injected at a rate of 50nl/min using a Nanoliter 2020 Injector (World Precision Instruments). For contralateral injections, we used the following coordinates relative to bregma: -1.1 mm rostro-caudal, +3.3 mm lateral, and -0.25 mm dorsoventral, while for ipsilateral injections: -1.1 mm rostro-caudal, -3.3 mm lateral, and -0.25 mm dorsoventral. All injections were performed using pulled glass micropipettes (World Precision Instruments). After each injection, the micropipette was left in place for 5 minutes to allow for AAVs diffusion before withdrawal.

Cortical cranial window implantation

Surgical tools were sterilized in a glass-bead sterilizer (Fine Science Tools) prior to use. Mice were anesthetized via intraperitoneal injection of medetomidine (0.5 mg/kg), midazolam (5 mg/kg), and fentanyl (0.05 mg/kg). The animals were then placed on a heating pad (36°C) with their heads fixed in a stereotactic frame. Eye ointment was applied to prevent drying (Bepanthen, Bayer). After cleansing the scalp with 70% ethanol, scalp was excised and the periosteum removed. A 3 mm diameter craniotomy site over the contralateral barrel cortex was marked and surrounded by a thin layer of dental acrylic (iBond Self Etch, Heraeus Kulzer), which was hardened with an UV polymerization lamp (Demi Plus, Kerr). The skull was thinned using a dental drill (Schick Technikmaster C1, Pluradent), and the bone flap was removed under sterile PBS.). A 3 mm circular coverslip was secured over the craniotomy with histoacryl adhesive (Aesculap). The exposed skull was covered with dental acrylic (Tetric Evoflow A1 Fill, Ivoclar Vivadent) and a headplate was attached for following imaging sessions. Post-surgery, mice received subcutaneous Carprophen (7.5 mg/kg) for analgesia. Anesthesia was reversed using Atipamezol (2.5 mg/kg), Naloxone (1.2 mg/kg), and Flumazenil (0.5 mg/kg) intraperitoneally. Animals recovered in a 35°C warming chamber before returning to their home cages.

Immunofluorescence and confocal imaging

Sections were incubated with guinea pig anti-Vesicular glutamate transporter 1 (vGlut1; Millipore AB5905) and rabbit anti-glutamic acid decarboxylase 65/67 (Gad65/67; Sigma G5163) antibodies (both at 1:5000 dilution), followed by Alexa Fluor 647-conjugated donkey anti-guinea pig and Alexa Fluor 488-conjugated donkey anti-rabbit secondary antibodies (1:1000). Images were acquired using a Zeiss LSM 880 confocal laser scanning microscope equipped with GaAsP and Airyscan detectors, using EC Plan-Neofluar 40x/1.30 Oil DIC M27 and Plan-Apochromat 100x/1.46 Oil DIC objectives. Quantification of vGlut1 and Gad65/67 puncta was performed in the homotopic contralesional cortex on three representative sections (bregma 0, -0.5, and -1.5 mm). Seven regions of interest (30 µm z-stack; 42.43 µm width) spanning the full cortical column from marginal zone to corpus callosum were analyzed per section. Puncta were counted using the Find Maxima function in FIJI ImageJ software (noise

tolerance: 15 for vGlut1, 20 for Gad65/67). The average count from three sections per animal was used for statistical comparisons between groups. Additionally, we manually quantified vGlut1 and Gad65/67 puncta overlapping with GFP-positive spines from labeled transcallosal neurons in the region homotopic to the lesion.

Real-time PCR

RNA extraction and quantitative RT-PCR analysis were performed to assess GABAA receptor subunits expression. At specified time points post-stroke, 3 mm diameter biopsy punches were used to collect tissue from the ipsilateral cortical lesion area and the homotopic contralesional cortex. Total RNA was isolated using the RNeasy Mini kit (Qiagen) following the manufacturer's protocol and quantified spectrophotometrically. DNase I-treated RNA (1000 ng) was reverse transcribed using oligo(dT)12-18 primers and Superscript II Reverse Transcriptase (Omniscript First-Strand Synthesis System, Qiagen). Real-time PCR was performed using the LightCycler QuantiNova SYBR Green RT-PCR Kit (Qiagen) with 20 ng cDNA template and 20pmol of each primer. Intron-spanning primers were designed for GABAA receptor subunits mediating phasic (α1, α2, δ) and tonic (α4, α5, γ2) inhibition (Table S1). Reactions were run in triplicate on a Light Cycler 480 Instrument (Roche). Melting curve analysis confirmed PCR product specificity. Expression levels were calculated using the 2^-ΔΔCT method, with GAPDH as the reference gene. Crossing point (CP) values were averaged from three independent reactions. Fold changes in expression were determined relative to sham-operated controls. To obtain overall measures of phasic and tonic inhibition, relative expression values of subunits mediating each type of inhibition were averaged for each animal.

In vivo calcium imaging

In vivo calcium imaging was conducted one-month post-cranial window implantation and AAV injection using a Leica SP8 DIVE 2-photon microscope equipped with a tunable and a fixed laser, a 25x water immersion objective (NA 1.0), and a motorized stage (Scientifica). GCaMP6s and tdTomato were excited at 940 nm and 1045 nm, respectively, with emission collected at 500-550 nm for GCaMP6s and 600-650 nm for tdTomato. To minimize phototoxicity, laser power was maintained at approximately

40mW below the objective. During imaging sessions, awake mice were head-fixed on a circular imaging platform (Gramophone, Femtonics Ltd). Single-plane time-lapse series (27.87 Hz) with 512 x 512 pixels per frame were recorded at a depth of 250-300 µm below the cortical surface. Following a 9-minute baseline recording, whisker stimulation (5 Hz, 80ms duration) was applied for 20 seconds using a Picospritzer (Parker-Hannifin Corporation). Image processing and subsequent analysis were performed post-experiment.

Calcium imaging data analysis

Time-lapse acquisitions of GCaMP6s and tdTomato-positive cells were analyzed using established Python software for calcium imaging data analysis. Videos were initially denoised using DeeplCAD-RT[19] to remove artifacts and enhance signal intensity changes. Subsequently, motion correction was applied using NoRMCorre[20] to mitigate motion artifacts. Following preprocessing, neuron detection and signal extraction were performed using Suite2p[21]. Distinction between GCaMP6s and tdTomato-positive cells was done manually using the Suite2p graphical user interface. The extracted ΔF/F calcium signals were then deconvolved using FOOPSI algorithm[22] to estimate underlying neural activity and remove additional artifacts. Peak detection was carried out using SciPy's peak detection module (Python). Neuronal responses after whisker stimulation were averaged to obtain the bulk response. Bulk response was then normalized and peak amplitude was detected using Python.

Laser speckle contrast imaging

We employed laser speckle contrast imaging to monitor cerebral blood flow (CBF) responses triggered by whisker stimulation in lightly sedated mice. The left whiskers were stimulated five times (1-2 Hz for 40 seconds, 3-minute intervals) while CBF responses were recorded in the right somatosensory cortex through a previously implanted cranial window. A PeriCam PSI High-Resolution Laser Speckle system acquired images at 44 frames/second, with numerical values generated using PIMSoft software. Data processing and analysis were performed using custom MATLAB scripts (R2016b, The MathWorks). A spherical region of interest (ROI) encompassing the exposed cortex was manually defined. The perfusion signal time-series for each pixel within the ROI was high-pass filtered (cutoff frequency: 0.004 Hz) using a Chebyshev Type I filter (order 2) to remove signal drift. Stimulation periods were automatically detected using Otsu's method and visually verified. To account for potential ramp-like increases at stimulation onset, the perfusion signal was averaged between 10-30 seconds post-stimulation and normalized to the baseline (average signal 40-10 seconds pre-stimulation). Normalized responses were averaged across stimulation periods for each animal, then across animals within experimental groups. For inter-animal comparisons, images were resized to a 120 x 120-pixel matrix.CBF responses for each 30-second stimulation were normalized to a 20-second pre-stimulation baseline. Individual and averaged responses for sham and stroke groups were analyzed. Heat maps were generated for individual animals to better understand response variations (Fig. S4). Exclusion criteria were implemented due to within-group variations in sham responses. Datasets were included only if a connected area of pixels covering at least 5% of the ROI showed a response above 10% of baseline intensity. One sham animal was excluded due to unrelated signal fluctuations

References

1 E. Carrera, G. Tononi, Diaschisis: past, present, future. Brain : a journal of neurology 137, 2408-2422 (2014)..

2 Guggisberg AG, Koch PJ, Hummel FC, Buetefisch CM. Brain networks and their relevance for stroke rehabilitation. Clin Neurophysiol. 2019 Jul;130(7):1098-1124. doi: 10.1016/j.clinph.2019.04.004. Epub 2019 Apr 15. PMID: 31082786; PMCID: PMC6603430.

3 Doron KW, Bassett DS, Gazzaniga MS. Dynamic network structure of interhemispheric coordination. Proc Natl Acad Sci U S A. 2012 Nov 13;109(46):18661-8. doi: 10.1073/pnas.1216402109. Epub 2012 Oct 29. PMID: 23112199; PMCID: PMC3503189.

4 Johnston DG, Denizet M, Mostany R, Portera-Cailliau C. Chronic in vivo imaging shows no evidence of dendritic plasticity or functional remapping in the contralesional cortex after stroke. Cereb Cortex. 2013 Apr;23(4):751-62. doi: 10.1093/cercor/bhs092. Epub 2012 Apr 11. PMID: 22499800; PMCID: PMC3657384.

5 Takatsuru Y, Fukumoto D, Yoshitomo M, Nemoto T, Tsukada H, Nabekura J. Neuronal circuit remodeling in the contralateral cortical hemisphere during functional recovery from cerebral infarction. J Neurosci. 2009 Aug 12;29(32):10081-6. doi: 10.1523/JNEUROSCI.1638-09.2009. PMID: 19675241; PMCID: PMC6664978.

6 Dana H, Chen TW, Hu A, Shields BC, Guo C, Looger LL, Kim DS, Svoboda K. Thy1-GCaMP6 transgenic mice for neuronal population imaging in vivo. PLoS One. 2014 Sep 24;9(9):e108697. doi: 10.1371/journal.pone.0108697. PMID: 25250714; PMCID: PMC4177405.

7 Lourbopoulos A, Mamrak U, Roth S, Balbi M, Shrouder J, Liesz A, Hellal F, Plesnila N. Inadequate food and water intake determine mortality following stroke in mice. J Cereb Blood Flow Metab. 2017 Jun;37(6):2084-2097. doi: 10.1177/0271678X16660986. Epub 2016 Jan 1. PMID: 27449604; PMCID: PMC5464703.

8 Wang Y, Chen Z, Ma G, Wang L, Liu Y, Qin M, Fei X, Wu Y, Xu M, Zhang S. A frontal transcallosal inhibition loop mediates interhemispheric balance in visuospatial processing. Nat Commun. 2023 Aug 25;14(1):5213. doi: 10.1038/s41467-023-40985-5. PMID: 37626171; PMCID: PMC10457336.

9 Empl L, Chovsepian A, Chahin M, Kan WYV, Fourneau J, Van Steenbergen V, Weidinger S, Marcantoni M, Ghanem A, Bradley P, Conzelmann KK, Cai R, Ghasemigharagoz A, Ertürk A, Wagner I, Kreutzfeldt M, Merkler D, Liebscher S, Bareyre FM. Selective plasticity of callosal neurons in the adult contralesional cortex following murine traumatic brain injury. Nat Commun. 2022 May 12;13(1):2659. doi: 10.1038/s41467-022-29992-0. PMID: 35551446; PMCID: PMC9098892.

10 Nikić I, Merkler D, Sorbara C, Brinkoetter M, Kreutzfeldt M, Bareyre FM, Brück W, Bishop D, Misgeld T, Kerschensteiner M. A reversible form of axon damage in experimental autoimmune encephalomyelitis and multiple sclerosis. Nat Med. 2011 Apr;17(4):495-9. doi: 10.1038/nm.2324. Epub 2011 Mar 27. PMID: 21441916.

11 Nagendran T, Larsen RS, Bigler RL, Frost SB, Philpot BD, Nudo RJ, Taylor AM. Distal axotomy enhances retrograde presynaptic excitability onto injured pyramidal neurons

via trans-synaptic signaling. Nat Commun. 2017 Sep 20;8(1):625. doi: 10.1038/s41467-017-00652-y. PMID: 28931811; PMCID: PMC5607003.

12 Jacobs KM, Donoghue JP. Reshaping the cortical motor map by unmasking latent intracortical connections. Science. 1991 Feb 22;251(4996):944-7. doi: 10.1126/science.2000496. PMID: 2000496.

13 Marshall RS, Perera GM, Lazar RM, Krakauer JW, Constantine RC, DeLaPaz RL. Evolution of cortical activation during recovery from corticospinal tract infarction. Stroke. 2000 Mar;31(3):656-61. doi: 10.1161/01.str.31.3.656. PMID: 10700500.

14 Dancause N, Touvykine B, Mansoori BK. Inhibition of the contralesional hemisphere after stroke: reviewing a few of the building blocks with a focus on animal models. Prog Brain Res. 2015;218:361-87. doi: 10.1016/bs.pbr.2015.01.002. Epub 2015 Mar 30. PMID: 25890146.

15 Grefkes C, Nowak DA, Wang LE, Dafotakis M, Eickhoff SB, Fink GR. Modulating cortical connectivity in stroke patients by rTMS assessed with fMRI and dynamic causal modeling. Neuroimage. 2010 Mar;50(1):233-42. doi: 10.1016/j.neuroimage.2009.12.029. Epub 2009 Dec 18. PMID: 20005962; PMCID: PMC8020334.16

16. Lazar RM, Berman MF, Festa JR, Geller AE, Matejovsky TG, Marshall RS. GABAergic but not anti-cholinergic agents re-induce clinical deficits after stroke. J Neurol Sci. 2010 May 15;292(1-2):72-6. doi: 10.1016/j.jns.2010.01.024. Epub 2010 Feb 20. PMID: 20172537; PMCID: PMC2849134.

17 Lazar RM, Fitzsimmons BF, Marshall RS, Berman MF, Bustillo MA, Young WL, Mohr JP, Shah J, Robinson JV. Reemergence of stroke deficits with midazolam challenge. Stroke. 2002 Jan;33(1):283-5. doi: 10.1161/hs0102.101222. PMID: 11779924.

18 Verley DR, Torolira D, Hessell BA, Sutton RL, Harris NG. Cortical Neuromodulation of Remote Regions after Experimental Traumatic Brain Injury Normalizes Forelimb Function but is Temporally Dependent. J Neurotrauma. 2019 Mar 1;36(5):789-801. doi: 10.1089/neu.2018.5769. Epub 2018 Oct 4. PMID: 30014759; PMCID: PMC6387565.

19 Li X, Li Y, Zhou Y, Wu J, Zhao Z, Fan J, Deng F, Wu Z, Xiao G, He J, Zhang Y, Zhang G, Hu X, Chen X, Zhang Y, Qiao H, Xie H, Li Y, Wang H, Fang L, Dai Q. Real-time denoising enables high-sensitivity fluorescence time-lapse imaging beyond the shot-noise limit. Nat Biotechnol. 2023 Feb;41(2):282-292. doi: 10.1038/s41587-022-01450-8. Epub 2022 Sep 26. PMID: 36163547; PMCID: PMC9931589..

20 Pnevmatikakis EA, Giovannucci A. NoRMCorre: An online algorithm for piecewise rigid motion correction of calcium imaging data. J Neurosci Methods. 2017 Nov 1;291:83-94. doi: 10.1016/j.jneumeth.2017.07.031. Epub 2017 Aug 3. PMID: 28782629.

21 Marius Pachitariu, Carsen Stringer, Mario Dipoppa, Sylvia Schröder, L. Federico Rossi, Henry Dalgleish, Matteo Carandini, Kenneth D. Harris. Suite2p: beyond 10,000 neurons with standard two-photon microscopy. bioRxiv. 2017. doi: https://doi.org/10.1101/061507

22 Vogelstein JT, Packer AM, Machado TA, Sippy T, Babadi B, Yuste R, Paninski L. Fast nonnegative deconvolution for spike train inference from population calcium imaging. J

Neurophysiol. 2010 Dec;104(6):3691-704. doi: 10.1152/jn.01073.2009. Epub 2010 Jun 16. PMID: 20554834; PMCID: PMC300765

Author Contributions

GMC, SVF, SF, FH, NP contributed to the study design. GMC and SF established the in vivo functional imaging methodologies performed in the manuscript. GMC, SVF, FH, BKG and FBS performed the experiments, acquired and quantified the data, and performed the statistical analysis. AL, BG, JJS and UM provided technical support. GMC, SF and NP implemented and finalized the manuscript previously written by SVF and FH with input and revision from all authors.

Competing Interests

The authors declare no competing interests.

Data availability

The data generated during the study are available from the corresponding author upon request.

Figures

Figure 1

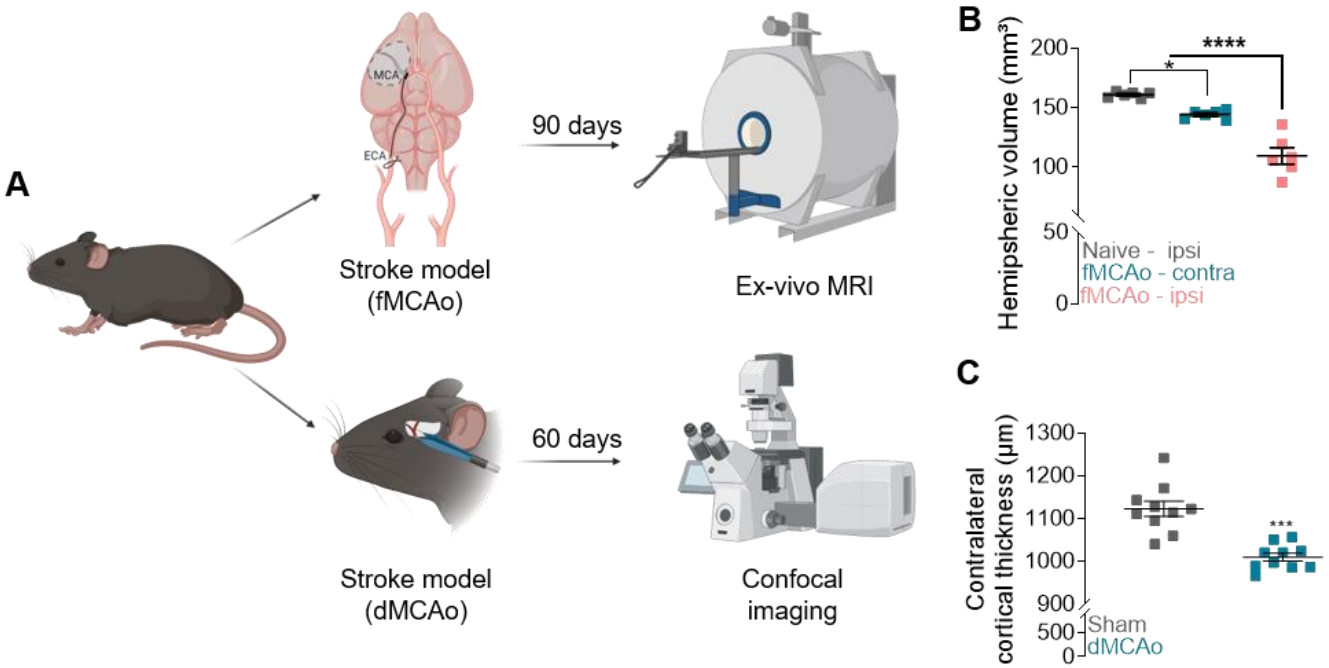

Figure 2

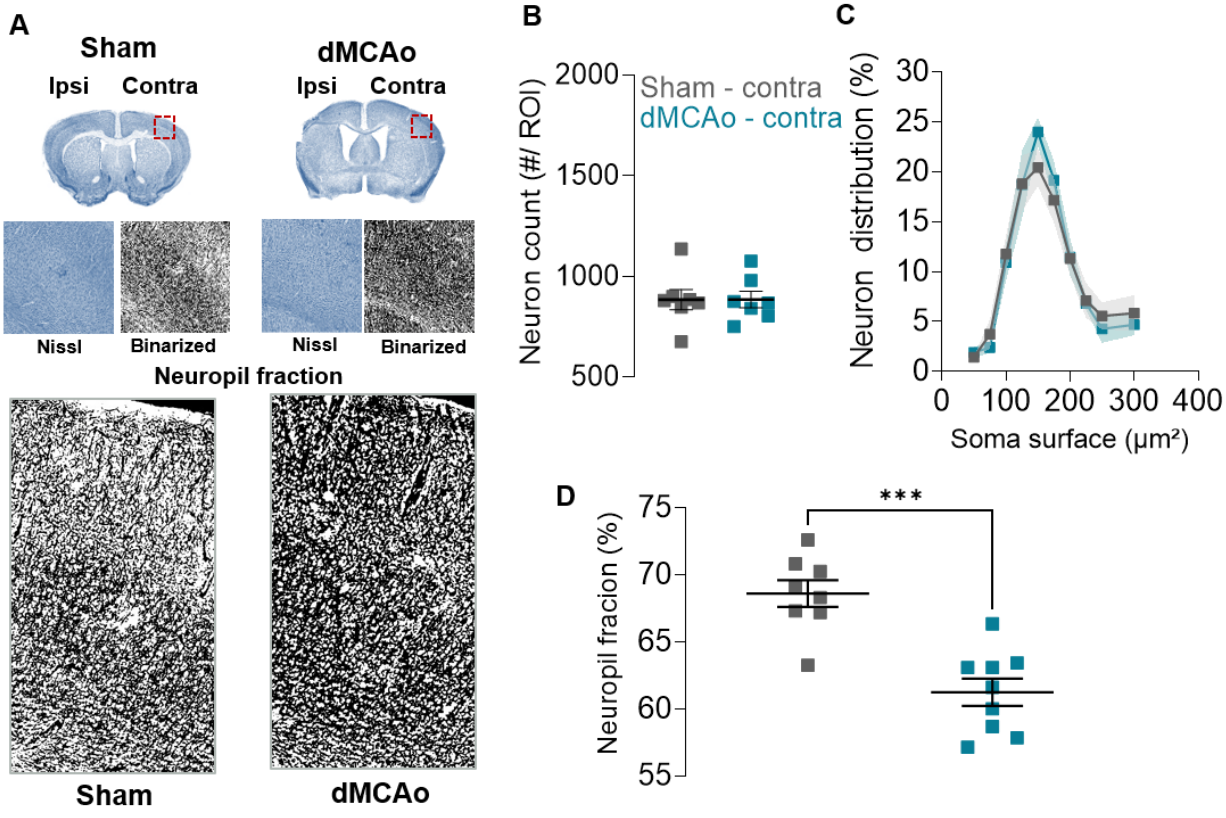

Figure 3

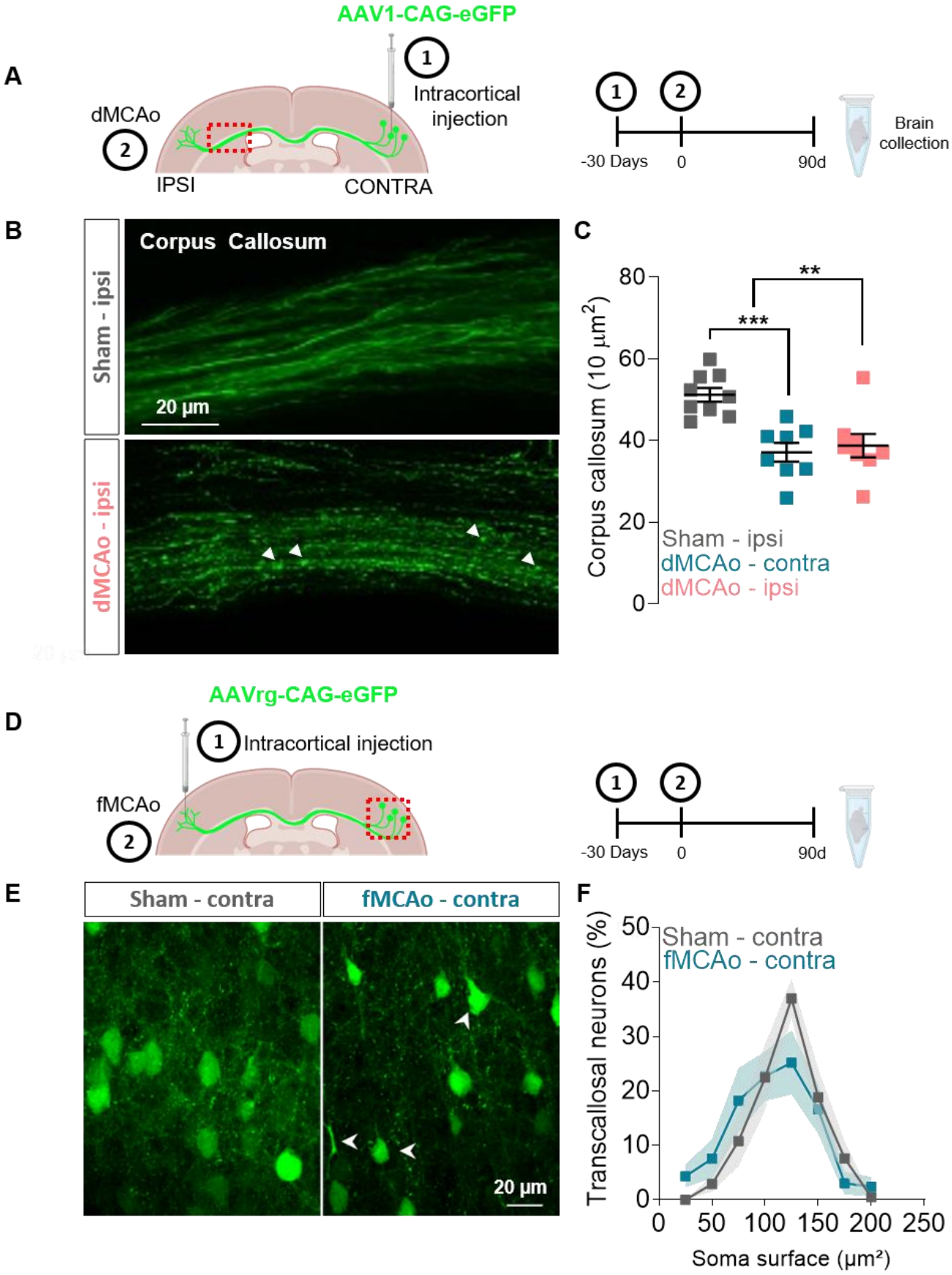
A
AAV1-CAG-eGFP
1
Intracortical injection
dMCAo
2
IPSI
CONTRA
1
2
-30 Days
0
90d
Brain collection
B
Sham - ipsi
Corpus Callosum
20 µm
dMCAo - ipsi
C
Corpus callosum (10 µm²)
80
60
40
20
0
**
***
Sham - ipsi
dMCAo - contra
dMCAo - ipsi
D
AAVrg-CAG-eGFP
1
Intracortical injection
fMCAo
2
1
2
-30 Days
0
90d
E
Sham - contra
fMCAo - contra
20 µm
F
Transcallosal neurons (%)
50
40
30
20
10
0
Sham - contra
fMCAo - contra
0
50
100
150
200
250
Soma surface (µm²)

Figure 4

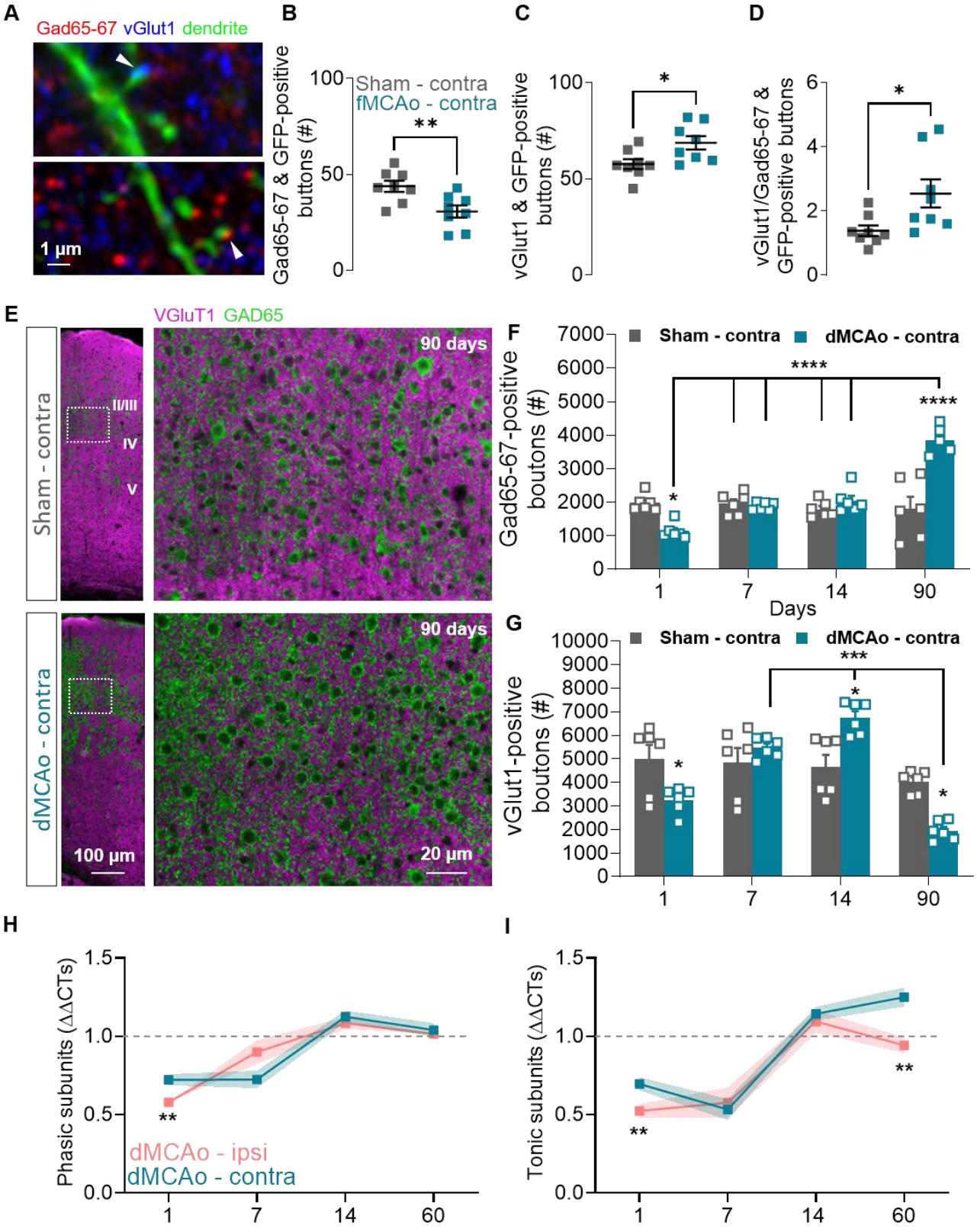
A
Gad65-67 vGlut1 dendrite
1 µm
B
Gad65-67 & GFP-positive buttons (#)
Sham - contra
fMCAo - contra
C
vGlut1 & GFP-positive buttons (#)
D
vGlut1/Gad65-67 & GFP-positive buttons
E
VGluT1 GAD65
Sham - contra
dMCAo - contra
II/III
IV
V
90 days
100 µm
20 µm
F
Gad65-67-positive boutons (#)
Sham - contra
dMCAo - contra
Days
G
vGlut1-positive boutons (#)
H
Phasic subunits (ΔΔCTs)
dMCAo - ipsi
dMCAo - contra
I
Tonic subunits (ΔΔCTs)

Figure 5

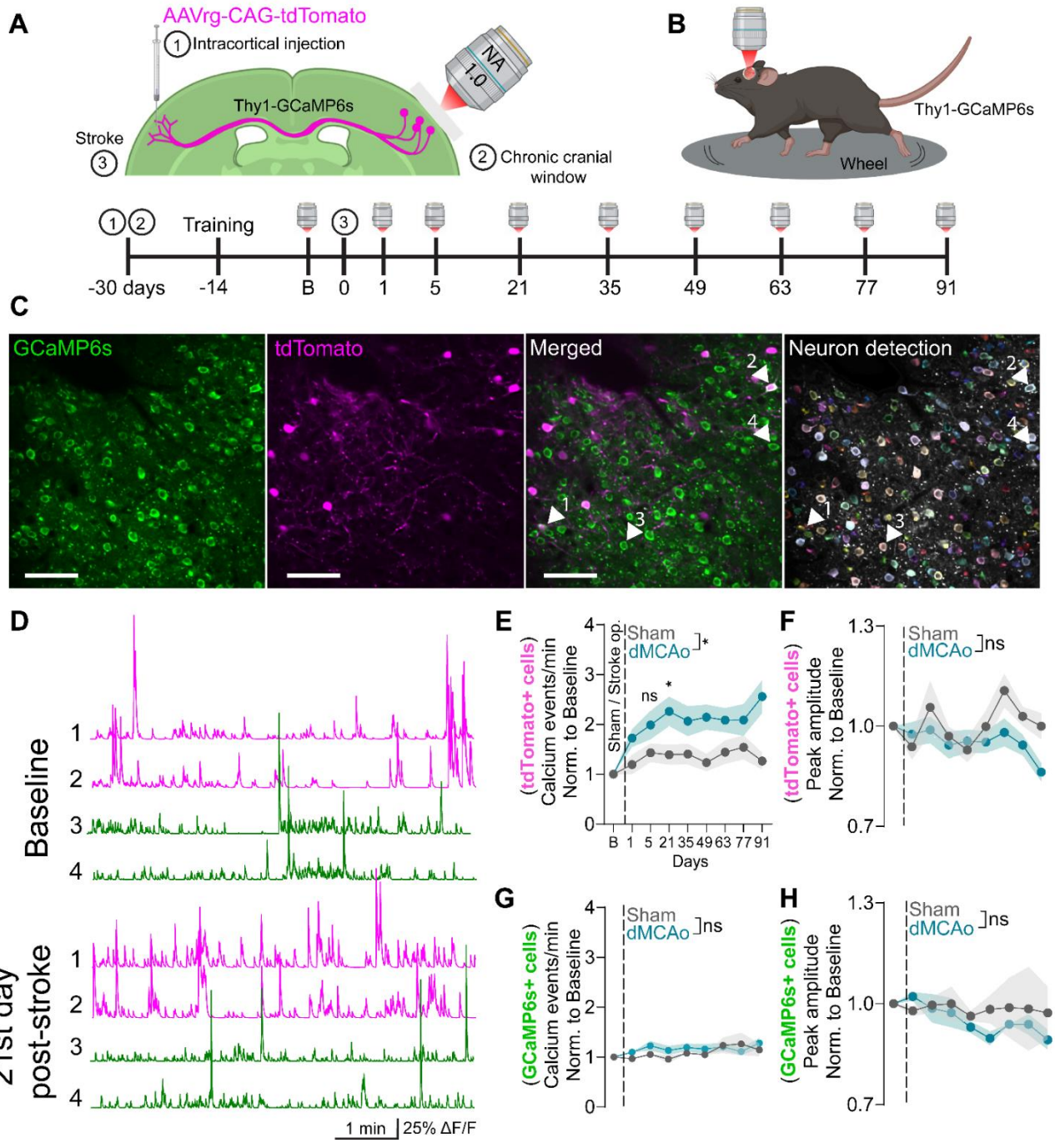
A
AAVrg-CAG-tdTomato
1 Intracortical injection
Thy1-GCaMP6s
Stroke 3
2 Chronic cranial window
NA 1.0
B
Thy1-GCaMP6s
Wheel
1 2 Training 3
-30 days -14 B 0 1 5 21 35 49 63 77 91
C
GCaMP6s
tdTomato
Merged
Neuron detection
D
Baseline
21st day post-stroke
1 min 25% ΔF/F
E
(tdTomato+ cells) Calcium events/min Norm. to Baseline
Sham / Stroke op.
Sham
dMCAo
*
ns
Days
F
(tdTomato+ cells) Peak amplitude Norm. to Baseline
ns
G
(GCaMP6s+ cells) Calcium events/min Norm. to Baseline
H
(GCaMP6s+ cells) Peak amplitude Norm. to Baseline

Figure 6

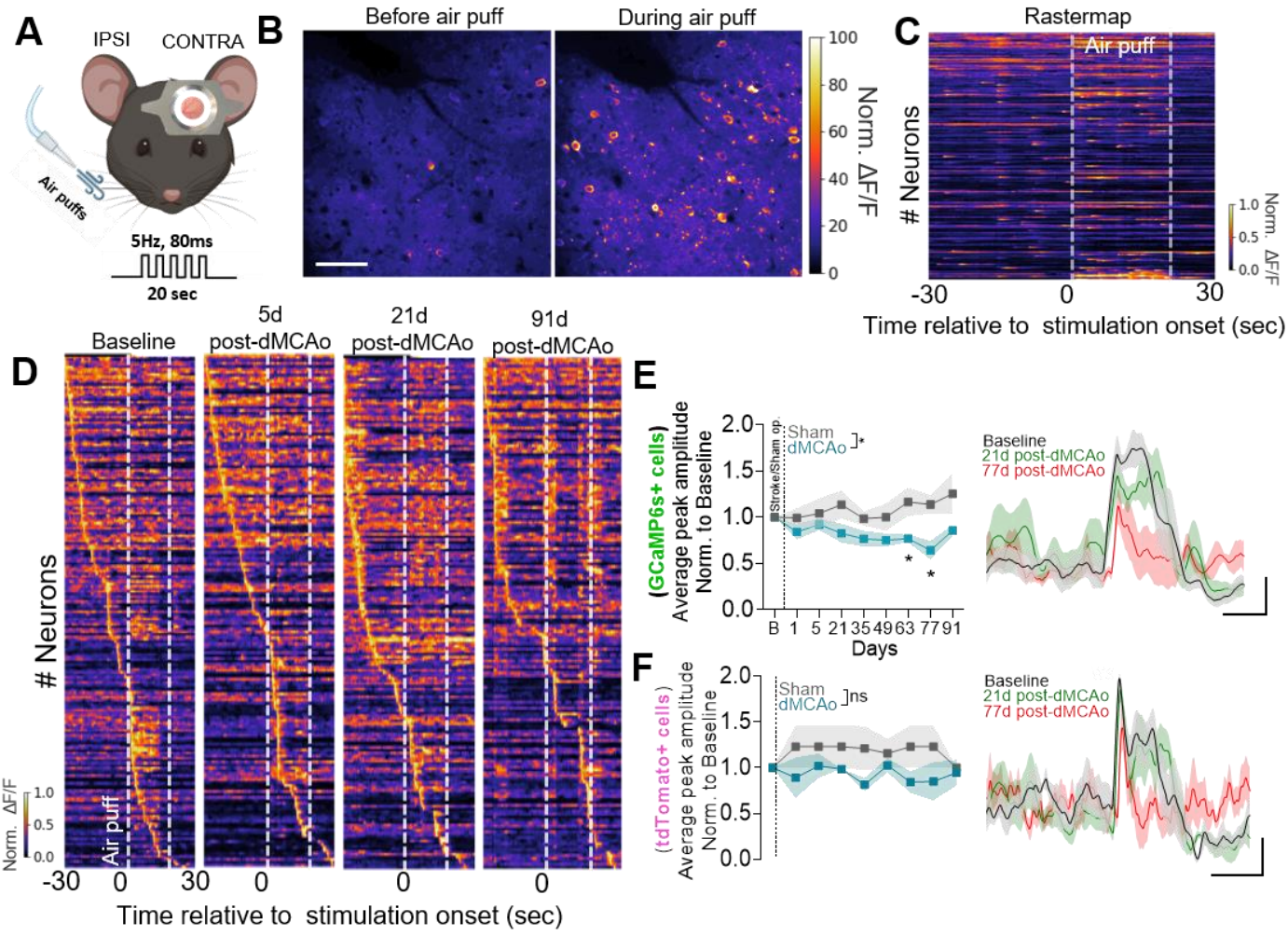
A
IPSI
CONTRA
Air puffs
5Hz, 80ms
20 sec
B
Before air puff
During air puff
Norm. ΔF/F
C
Rastermap
Air puff
Neurons
Time relative to stimulation onset (sec)
D
Baseline
5d post-dMCAo
21d post-dMCAo
91d post-dMCAo
Neurons
Air puff
Time relative to stimulation onset (sec)
E
(GCaMP6s+ cells)
Average peak amplitude Norm. to Baseline
Stroke/Sham op
Sham
dMCAo
Days
Baseline
21d post-dMCAo
77d post-dMCAo
F
(tdTomato+ cells)
Average peak amplitude Norm. to Baseline
Sham
dMCAo
ns
Baseline
21d post-dMCAo
77d post-dMCAo

Figure 7

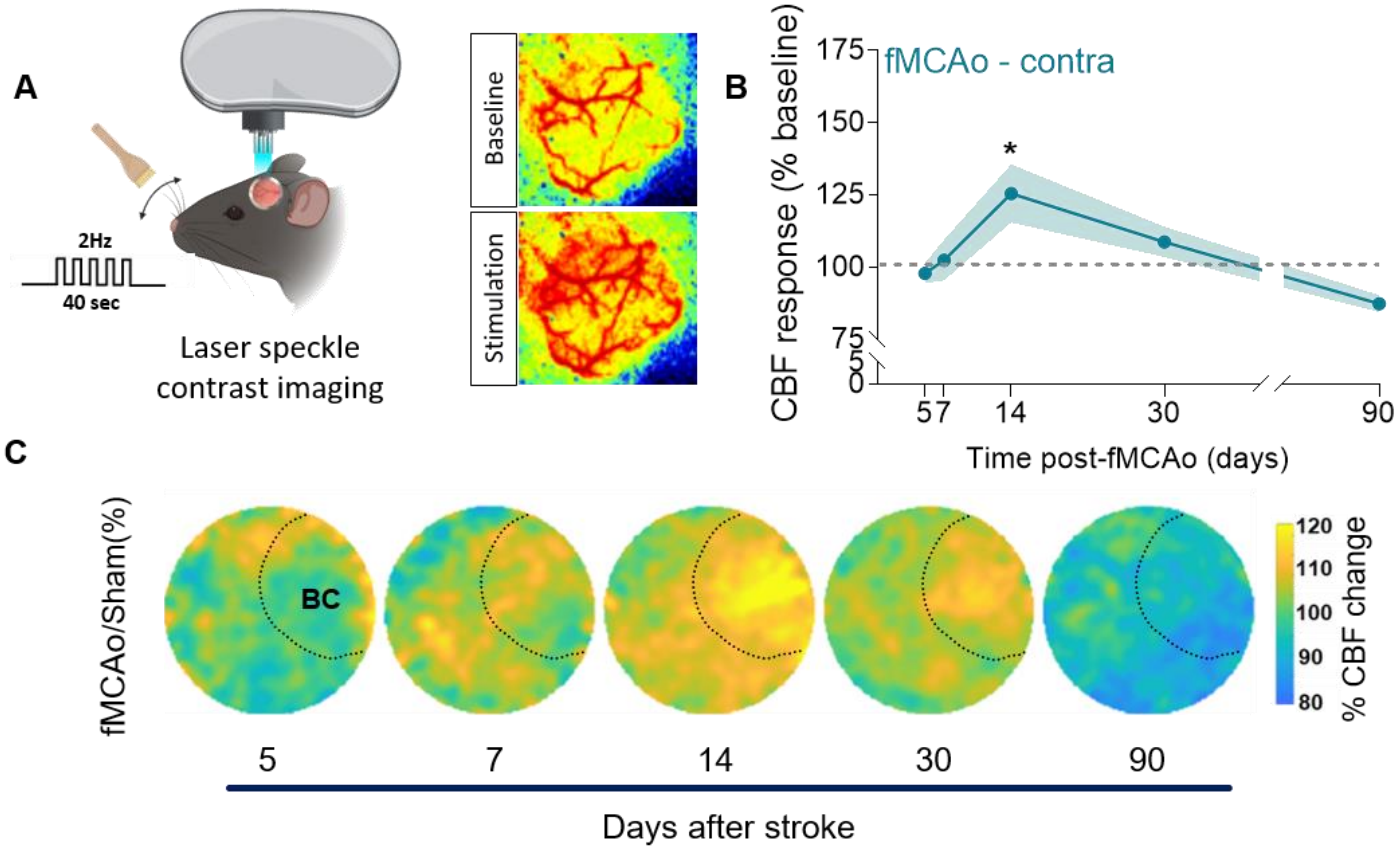
A
2Hz
40 sec
Laser speckle
contrast imaging
Baseline
Stimulation
B
fMCAo - contra
CBF response (% baseline)
175
150
125
100
75
0
*
57
14
30
90
Time post-fMCAo (days)
C
fMCAo/Sham(%)
BC
120
110
100
90
80
% CBF change
5
7
14
30
90
Days after stroke

Figure legends

Figure 1: Experimental stroke leads to contralateral cortical thinning

(A) Experimental design showing two stroke models to investigate distant brain effects. Upper: Filament middle cerebral artery occlusion (fMCAo) inducing large strokes affecting cerebral cortex and basal ganglia, followed by ex-vivo MRI analysis at 90 days post-stroke. Lower: Distal middle cerebral artery occlusion (dMCAo) inducing isolated cortical infarcts, followed by confocal imaging at 60 days post-stroke. **(B)** Hemispheric volume measurements following fMCAo showing significant reductions in both ipsilateral (~32%) and contralateral (~11%) hemispheres compared to naive controls (n=6 per group; Ordinary one-way ANOVA followed by Tukey's multiple comparisons test; means ± SEM; ****p<0.0001, *p<0.05). **(C)** Contralateral cortical thickness measurements following dMCAo demonstrating significant reduction in dMCAo animals (1010 µm) compared to sham controls (1123 µm) (n=10 per group; Unpaired t-test; means±SEM; ****p<0.0001).

Figure 2: Stroke triggers contralateral neuropil atrophy without neuronal loss

A) Schematic overview of the experimental design and region of interest selection. Representative coronal brain sections from Sham and dMCAo animals show the ipsilateral (Ipsi) and contralateral (Contra) hemispheres, with red boxes indicating the analyzed region in the contralateral barrel cortex. Enlarged images show Nissl-stained sections and corresponding binarized images used for quantification. Lower panels illustrate representative binarized images from Sham and dMCAo contralateral cortices used for neuropil fraction analysis. **B)** Quantification of neuronal density in the contralateral barrel cortex shows no significant difference between Sham and dMCAo groups (n=7 per group). Unpaired t-test; means±SEM; ns (p=0.9915). **C)** Distribution of neuronal soma sizes in the contralateral barrel cortex shows no significant differences between Sham (n=6) and dMCAo (n=7) groups across all size bins (50–300 µm²; data are presented as mean ± SEM; Šídák's multiple comparisons test; all comparisons not significant; p > 0.05). **D)** Neuropil fraction analysis reveals a significant reduction in dMCAo animals (61.23%, n=9) compared to Sham controls (68.59%, n=8). Mean difference: -7.360 ± 1.432% (95% CI: -10.41 to -4.307). Unpaired t-test (t=5.139, df=15); means ± SEM; ***p=0.0001.

Figure 3: Ischemia induces corpus callosum atrophy

A) On the left, schematic representation of the first experimental approach, in which AAV1-CAG-eGFP was injected intracortically into the hemisphere contralateral to the future infarct site. This allowed for the anterograde labeling of neurons and their transcallosal axons projecting to the stroke-affected region. On the right, Timeline summarizing the experimental protocol. **B)** Representative images showing GFP-

labeled transcallosal axons in the corpus callosum of sham-operated (top) and dMCAo (bottom) mice. Dendritic beading, indicative of structural damage, is marked by white arrows. **C)** Quantification of the GFP-positive axonal area in the corpus callosum of the ipsilateral hemisphere in sham (n=9; grey) and dMCAo (n=8; orange) mice, as well as in the contralateral hemisphere of dMCAo mice (n=8; teal). Data are presented as mean ± SEM. Statistical analysis was performed using ordinary one-way ANOVA followed by Tukey's multiple comparisons test. *p < 0.05, **p < 0.001. **D)** On the left, Schematic of a second viral labeling strategy using a retrograde AAV injected directly into the future infarct core to specifically label contralateral transcallosal projection neurons. On the right, Corresponding experimental timeline. **E)** Representative images of GFP-labeled contralateral transcallosal neurons in sham (left) and fMCAo (right) mice. Arrows indicate shrunken soma morphology, suggestive of neuronal atrophy or degeneration, in the fMCAo group. **F)** Quantification of the soma surface area of contralateral transcallosal neurons in sham (n=8; grey) and fMCAo (n=8; teal) mice. Data are expressed as mean ± SEM. Statistical comparison was performed using ordinary one-way ANOVA followed by Tukey's multiple comparisons test.

Figure 4: Excitation-inhibition imbalance in the contralateral cortex following stroke

A) Contralesional cortical columns in the barrel field 12 weeks post-stroke, immunolabeled for Vesicular Glutamate Transporter 1 (vGlut1) and Glutamic Acid Decarboxylase 65/67 (Gad65/67), with magnified Layer II/III views comparing sham (left) and stroke (right) brains. **B)** Quantification of Gad65/67 and **C)** vGlut1 puncta density in cortical columns (n = 7 per group). **(D-E)** Relative expression of GABAA receptor subunits mediating tonic (D) and phasic (E) inhibition in ipsilesional peri-infarct and contralesional homotopic regions (sham controls: dashed line). **(F-G)** vGlut1 (F) and Gad65/67 (G) puncta density on dendrites of deafferented transcallosal neurons in contralesional homotopic areas. **H)** Synaptic Gad65/67-to-vGlut1 ratio (n = 8–9 mice per group). Data represent mean ± SD; analyzed by one-way ANOVA (Bonferroni post-hoc) and Student's t-test (*p < 0.05, **p < 0.001, ***p < 0.0001).

Figure 5: Stroke causes hyperactivation of contralateral transcallosal neurons

A) On the left, Schematic overview of the experimental design and viral vector strategy used to retrogradely label contralateral transcallosal neurons. On the right, Illustration of in vivo two-photon imaging in awake, head-fixed mice. On the bottom, timeline of the experimental schedule, including imaging sessions before and after dMCAo. **B)** Representative field of view showing GCaMP6s-positive neurons (green), TdTomato-positive neurons (red), merged channels, and corresponding automated neuron detection in the same region. **C)** Representative calcium traces from two neurons co-

expressing GCaMP6s and TdTomato at baseline and 21 days post-dMCAo. Note the increased frequency of calcium transients in TdTomato-positive neurons at 21 days post-stroke. **D)** Quantification of calcium event frequency in TdTomato-positive neurons from sham-operated mice (n = 37 cells) and dMCAo-operated mice (n = 59 cells), normalized to baseline. **E)** Amplitude of calcium transients in TdTomato-positive neurons from sham (n = 37 cells) and dMCAo mice (n = 59 cells), normalized to baseline. **F)** Frequency of calcium events in GCaMP6s-positive neurons from sham-operated (n = 3 mice) and dMCAo-operated animals (n = 5 mice), normalized to baseline. **G)** Amplitude of calcium transients in GCaMP6s-positive neurons, normalized to baseline. Statistical analyses were performed using mixed-effects models and Student's *t*-test. *$p < 0.05$.

Figure 6: Stroke triggers chronic weakening in contralateral neuronal response

A) Schematic representation of the experimental approach, including the sensory stimulation setup. The air-puff stimulation protocol used to evoke neuronal responses is shown on the right. **B)** Representative field of view of neuronal activity (ΔF/F) before and during air-puff stimulation. Note the increased fluorescence signal during stimulation, indicating heightened neuronal activity. **C)** Raster plot of neuronal calcium activity corresponding to the field of view shown in (B) (n = 132 cells), illustrating the temporal dynamics of individual neuronal responses to sensory stimulation. **D)** Onset latency plot from a representative mouse showing activation times of individual neurons across the experimental timeline (Baseline: n = 177 cells; 5d post-dMCAo: n = 174 cells; 21d post-dMCAo: n = 177; 91d post-dMCAo: n = 177 cells). **E)** Quantification of the amplitude of evoked bulk neuronal responses in TdTomato-positive neurons from sham-operated (n = 3 mice) and dMCAo-operated (n = 5 mice) animals. Right: Representative traces of the evoked bulk responses for each group. **F)** Quantification of the amplitude of evoked bulk neuronal responses in GCaMP6s-positive neurons from sham-operated (n = 3 mice) and dMCAo-operated (n = 5 mice) animals. Right: Corresponding traces illustrating evoked responses in each group. Statistical analyses were performed using mixed-effects models and Student's t-test. $p < 0.05$.

Figure 7: Stroke induces chronic impairment of neurovascular coupling in the contralateral hemisphere

A) Schematic representation of the experimental setup, including the application of air-puff stimulation to the ipsilateral whisker pad and the corresponding stimulation protocol. On the right, representative images of cortical activity during baseline and whisker stimulation, illustrating the evoked response. **B)** Quantification of the average peak response amplitude across groups. Data are presented as mean ± SD. Statistical comparison was performed using Student's t-test. $p < 0.05$. **C)** Heatmaps showing the spatial distribution of average responses in stroke and sham groups.

3.2 Study II: A novel glutamate reporter line for whole-brain monitoring of glutamate dynamics

Gian Marco Calandra[1,2#], Dániel Péter Varga[1,2,4#*], Paul Feyen[5], Francesco Gubinelli[2,5], Benedikt Wefers[2,5], Peter Makra[7], Joshua James Shrouder[1,2], Lena Burbulla[2,5], Wolfgang Wurst[2,5], Andrea Cattaneo[1,2,6], Jochen Herms[2,5], Arthur Liesz[1,2], Severin Filser[1,2,3#]& Nikolaus Plesnila[1,2#]

1) Institute for Stroke and Dementia Research (ISD), University Hospital, Ludwig-Maximilians University (LMU) Munich, Germany. 2) Munich Cluster for Systems Neurology (SyNergy), Munich, Germany. 3) Deutsches Zentrum für Neurodegenerative Erkrankungen (DZNE), Light Microscope Facility (LMF), Bonn, Germany. 4) Deutsches Zentrum für Neurodegenerative Erkrankungen (DZNE), Image and Data Analysis Facility (IDAF), Bonn, Germany. 5) Deutsches Zentrum für Neurodegenerative Erkrankungen (DZNE), Munich, Germany. 6) Department of Neurosurgery, University Hospital Würzburg, Würzburg, Germany. 7) Department of Medical Physics and Informatics, Faculty of Science and Informatics, University of Szeged, Szeged, Hungary

# These authors contributed equally to this study.

Abstract

Glutamate, the brain's primary excitatory neurotransmitter, plays a critical role in neural circuit function, yet monitoring its dynamics in vivo has been limited by the constraints of viral delivery systems, which can exhibit variable expression and potential toxicity over time. To address these limitations, we developed a novel ROSA26 knock-in mouse model engineered for conditional, stable, and longitudinal expression of the iGluSnFR3 glutamate sensor (GluTrooper). Through Cre/loxP-mediated conditional expression, GluTrooper displayed robust and uniform sensor expression in cortical excitatory neurons when crossed with Emx1-Cre mice, with prominent fluorescence in the cortex, hippocampus, and olfactory bulb. Importantly, iGluSnFR3 expression remained stable across developmental timepoints, enabling reliable longitudinal investigations. Through multimodal imaging, we demonstrated the versatility of GluTrooper across spatial scales, from whole-cortex widefield imaging to two-photon microscopy in awake head-fixed mice. During cortical spreading depolarization, we captured bilateral glutamate dynamics with high temporal and spatial and identified contralateral disinhibition, a compensatory phenomenon previously not detectable with traditional invasive methodologies. The compatibility of our novel reporter line with diverse Cre-driver lines positions it as a valuable tool for cell type-specific interrogation of glutamatergic signaling under both physiological and pathophysiological conditions, offering unprecedented opportunities for chronic, non-invasive monitoring of excitatory neurotransmission in living brain circuits.

Introduction

Glutamate is the principal excitatory neurotransmitter in the mammalian central nervous system, critically shaping the excitatory-inhibitory balance alongside GABAergic signaling [1-3]. The ability to monitor extracellular glutamate in vivo has become increasingly valuable for understanding neural circuit function in both physiological and pathophysiological conditions. Recent advances in genetically encoded fluorescent sensors, particularly the intensity-based glutamate sensor iGluSnFR, have enabled direct, high-resolution visualization of glutamate dynamics [4-7]. While adeno-associated virus (AAV)-mediated delivery has been widely adopted for sensor expression in the brain, it poses several limitations, especially for long-term studies. AAV-driven expression can increase over time, potentially reaching levels that induce excitotoxicity and compromise cellular health [8, 9]. In contrast, transgenic models offer stable and uniform expression, minimizing variability and supporting longitudinal investigations [8, 10]. To overcome the constraints of viral delivery and facilitate chronic glutamate imaging, we generated GluTrooper, a knock-in mouse line expressing iGluSnFR3 from the ROSA26 locus. By crossing this line with Emx1-Cre mice [11] (JAX #005628), we achieved pan cortical expression of the sensor in excitatory neurons located in cortex, hippocampus, and olfactory bulb. GluTrooper enables reliable in vivo tracking of glutamatergic dynamics across the brain in awake, head-fixed mice under physiological and pathophysiological conditions, such as cortical spreading depolarizations.

Results

Generation of a conditional ROSA26 knock-in mouse for targeted and longitudinal expression of iGluSnFR3

To enable the investigation of glutamatergic neurotransmission, we utilized a knock-in strategy targeting the well-characterized ROSA26 locus, which enables robust expression of transgenes avoiding the interference of endogenous gene function [12, 13]. The targeting construct included 5' and 3' homology arms (ROSA 5'HA and ROSA 3'HA) flanking the functional elements to ensure precise integration by homologous recombination (Fig.1A top). The construct contained an AG slice promoter followed by an FRT-flanked sequence, a ubiquitous CAG promoter to drive high level expression, and a loxP-flanked puromycin resistance cassette (puroR) acting as a STOP signal in front of the iGluSnFR3 coding sequence. The presence of the STOP cassette prevents the expression of iGluSnFR3 until Cre-mediated recombination removes the intervening sequence, making this design critical for achieving conditional expression. Additional regulatory elements included the Woodchuck Hepatitis Virus Posttranscriptional Regulatory Element (WPRE) to enhance mRNA stability and translation efficiency, as well as human growth hormone (hGH) and SV40 polyadenylation signals to ensure proper mRNA processing and stability. The resulting mouse line, named GluTrooper (ROSA26-CAG-lsl-iGluSnFR3), carries the iGluSnFR3 transgene in all cells but expresses it only upon concomitant expression of the Cre recombinase. Genotyping confirmed successful germline transmission and maintenance of the transgene through multiple generations, establishing a stable line for experimental use. To achieve whole-cortex expression, mice were crossed with Emx1-Cre mice [11] (JAX stock #005628) (Fig1A bottom and B). Regional analysis revealed robust iGluSnFR3 intensity levels in the cortex, olfactory bulb, and hippocampus (Fig. 1C and D). Given the cerebellum's distinct developmental origin and lack of transcription factor Emx1 [14], it served as an internal control for regional iGluSnFR3 intensity quantification [15]. Sensor fluorescence intensity was prominent in the somatosensory cortex (Fig. 1E; nearly 8 folds vs Cerebellum), hippocampus (Fig. 1F; 11.20 folds vs Cerebellum) and olfactory bulb (Fig. 1G; nearly 8 folds vs Cerebellum) compared to cerebellar levels. Importantly, iGluSnFR3 expression showed no significant regional variation across developmental timepoints (Fig. 1E-G;

3 months vs 12 months; >0.05; see also suppl. Fig. 1), making the GluTrooper a unique tool for mapping glutamatergic neurotransmission in both acute and longitudinal investigations.

Whole-cortex glutamate dynamics in awake head-fixed mice

To capture cortex-wide glutamate dynamics in vivo, we employed widefield mesoscale imaging (Fig. 2A top). To disentangle glutamate dynamics from overlapping hemodynamic responses, we integrated a multispectral illumination approach using a three-wavelength LED system (Thorlabs; Fig. 2A top), enabling simultaneous detection of iGluSnFR3 dynamics and relative changes in oxyhemoglobin (ΔHbO) and deoxyhemoglobin (ΔHbR) levels (Fig. 2A bottom). Sensory-evoked glutamate release was elicited using a 10-second tactile stimulus applied to the left whisker pad via a custom Arduino-controlled system (Fig. 2A bottom). Glutamate responses were quantified in the right primary somatosensory cortex (S1), contralateral to the site of stimulation, with the corresponding region in the left hemisphere serving as an internal control. Under baseline conditions, spontaneous rate of glutamate events (Fig. 2B top; $p = 0.88$) and amplitude (Fig. 2B bottom; $p = 0.30$) were comparable between S1 cortices. However, whisker stimulation produced a significant increase in both the rate of glutamate events (Fig. 2C top; $p = 0.001$) and their amplitude (Fig. 2C bottom; $p = 0.04$) in the right S1, confirming stimulus specificity of the observed iGluSnFR3 dynamics. To further dissect the relationship between neural and vascular activity, we examined the temporal evolution of iGluSnFR3 alongside ΔHbO and ΔHbR across baseline and stimulated conditions (Fig. 2D-E). Whisker stimulation evoked a robust increase in iGluSnFR3 signal (>11%; $p = 0.007$), alongside with a significant rise in ΔHbO (>12%; $p = 0.006$) and a reciprocal drop in ΔHbR (<3%; $p = 0.006$; Fig. 2D-E). Correlation analyses during spontaneous activity revealed a strong positive association between glutamate fluctuations and ΔHbO, and an inverse relationship with ΔHbR (Fig. 2F left); positive and negative correlations that became stronger upon whisker stimulation (Fig. 2F right). Notably, temporal alignment of signal peaks demonstrated that glutamate elevations preceded vascular changes, with iGluSnFR3 reaching its maximum ~0.56 s after stimulation onset, followed by ΔHbO and ΔHbR peaks at 2.83 s and 2.94 s, respectively (Fig. 2G), indicating that the observed glutamate dynamics, are temporally and mechanistically distinct from hemodynamic

signals. These results demonstrate the applicability of the GluTrooper for monitoring whole-brain glutamate dynamics in awake, head-fixed mice, offering a direct measure of excitatory neurotransmission and its correlation with vascular dynamics.

In vivo dual imaging of interhemispheric neurovascular coupling during cortical spreading depolarization

After assessing glutamate dynamics in spontaneous and evoked conditions, we utilized our novel glutamate reporter line for the observation of cortical spreading depolarizations [16] (CSDs), an aberrant wave of cortical excitation that occurs during migraine aura and following stroke [17-19] and brain injury [20-23]. Under light anesthesia, mice were subjected to an acute cranial window over the occipital cortex, followed by careful removal of the dura. A 1M KCl- solution was then topically applied to the exposed cortical surface to induce the initiation of CSD in the left hemisphere and its spatiotemporal progression was captured across multiple timepoints (Fig. 3A). Spatiotemporal glutamate dynamics during CSD were quantified using three homotopic regions of interest (ROIs) distributed along the caudal–rostral axis in both hemispheres (Fig. 3B). Upon KCl- application, the CSD propagated across the left hemisphere triggering a >1000% ΔF/F increase in iGluSnFR3 in all ROIs (Fig. 3C-D; Baseline vs CSD). Notably, elevated glutamate levels were also detected in contralateral ROIs as the wave progressed, with the strongest increase emerging in the most frontal ROI (>50% of iGluSnFR3 % ΔF/F; Fig. 3E-F) suggesting a bilateral response. Spatiotemporal analysis of the CSD revealed that the wave of depolarization crossed the left hemisphere with a velocity of 3.63 mm/min (Fig. 3G), and a larger area under the curve compared to the glutamate dynamics observed in the right hemisphere (Fig. 3H; $p = 0.0009$). To assess concurrent cerebral hemodynamic changes, we simultaneously measured ΔHbO and ΔHbR in the same bilateral ROIs across three distinct phases: Before CSD, CSD onset, and post-CSD (Fig. 3I). In the ipsilateral hemisphere, ΔHbO significantly increased post-CSD (Fig. 3J; $p = 0.001$), consistent with the transient hyperemic response and perfusion-driven oxygen delivery following CSDs described in previous studies [24] , while ΔHbR did not show significant changes across the different phases (Fig. 3K). In contrast, the contralateral hemisphere exhibited no significant changes in ΔHbO or ΔHbR, suggesting that absolute

hemodynamic alterations were largely confined to the affected hemisphere (Fig. 3L-M). Together, these findings underscore the utility of our novel reporter line for real-time, dual-modality imaging of excitatory neurotransmission and vascular dynamics during CSD. Most importantly, this approach provides a more direct, non-invasive assessment of neurovascular coupling under pathophysiological conditions, offering a viable alternative to traditional invasive methodologies.

GluTrooper enables non-invasive observation of contralateral glutamatergic disinhibition

Following our observation of widespread glutamate dynamics during spreading depolarization, we aimed to determine whether the GluTrooper could enable monitoring of contralateral disinhibition, a phenomenon that occurs following stroke and brain injury due to an unbalance of the interhemispheric inhibitory loop [25, 26]. To investigate this phenomenon, we selected two regions of interest in the center of each hemisphere (Fig. A) and continuously observed iGluSnFR3 fluorescence before and after CSD induction in both hemispheres. Analysis of the left hemisphere revealed distinct changes in glutamate dynamics following CSD (Fig. 4B). Quantitative and qualitative analysis showed a significant reduction in the amplitude of glutamate events (Fig. 4C left; $p = 0.03$) as well as their rate (Fig. 4C right; $p = 0.01$). These results are in line with the extensive literature focused on CSD, representing the strong long-lasting cellular depression that follows this phenomenon [16, 27-29]. In contrast, the contralateral hemisphere exhibited a markedly different response profile (Fig. 4D). Post-CSD, event amplitudes remained stable (Fig. 4E right; $p = 0.43$), however, we observed a significant increase in the rate of glutamate events following CSD (Fig. 4E left; $p = 0.01$), indicative of contralateral disinhibition [30]. These findings demonstrate the great sensitivity of the GluTrooper in capturing interhemispheric compensations that traditionally required invasive electrophysiological techniques such as EEG.

In vivo two-photon observation of glutamate dynamics

To observe changes in glutamate with high spatial resolution, we performed two-photon microscopy in awake, head-fixed mice. Mice received a cranial window over the right barrel cortex (Fig. 5A) and functional in vivo two-photon microscopy was performed two weeks later (Fig. 5A). During baseline and following air-puff stimulation to the left whisker pad, we observed distinct fluorescent patches within the field of view, corresponding to regions of glutamate release (Fig. 5B). Example traces from individual patches showed positive changes in fluorescence intensity following sensory stimulation (Fig. 5C). Spatiotemporal analysis, across detected patches, revealed a robust increase in iGluSnFR3 ΔF/F upon stimulation (Fig. 5D-E). Frequency distribution analysis indicated that most iGluSnFR3 %ΔF/F values were distributed around 6% (Fig. 5). Statistical comparison of pooled data from all animals and ROIs confirmed a significant increase in iGluSnFR3 %ΔF/F during stimulation compared to baseline periods (90 detected patches; Baseline vs Peak $p<0.0001$; n ROIs = 90, Fig. 5G). These findings highlight the versatility of our novel reporter line for multimodal investigation of glutamate dynamics across different spatial scales, facilitating longitudinal studies of glutamate signaling in vivo.

Discussion

The present study introduces the GluTrooper, a novel ROSA26 knock-in model enabling conditional, robust, and longitudinal expression of the iGluSnFR3 glutamate sensor under the ubiquitous CAG promoter. By crossing with Emx1-Cre mice, we achieved strong expression of iGluSnFR3 in the cerebral cortex, the hippocampus, and the olfactory bulb; no expression was observed in the cerebellum, confirming the specificity and efficacy of our genetic approach [15]. Importantly, we found no significant developmental variation in iGluSnFR3 intensity, indicating that the GluTrooper supports consistent glutamate monitoring across diverse brain areas and throughout adulthood. The consistent expression across ages is a key advantage, enabling reliable longitudinal monitoring of glutamate dynamics. Functionally, we demonstrated the utility of GluTrooper in capturing whole-cortex glutamate dynamics in awake, head-fixed mice. Sensory-evoked stimulation elicited significant modulation in both the rate and amplitude of glutamate events in the contralateral primary somatosensory cortex. By employing multispectral illumination, we simultaneously observed ΔHbO and ΔHbR levels, observing that glutamate elevations precede vascular responses with a temporal dissociation of ~ 2.3 seconds, confirming the physiological relevance of the observed glutamate dynamics [31].

The versatility of the GluTrooper was further demonstrated under pathophysiological conditions, that is CSD, where we observed bilateral fluctuations in iGluSnFR3 fluorescence, highlighting the model's ability to measure widespread glutamatergic neurotransmission. Thanks to the pan-cortical expression of the sensor, we were able to detect bilateral spontaneous glutamate fluctuations both before and after CSD, with a notable increase in contralateral glutamate activity. Remarkably, these compensatory interhemispheric events, which previously required invasive techniques to be observed, can now be monitored non-invasively.

Finally, we confirmed the compatibility of the line with two-photon microscopy, achieving high spatial and temporal resolution of glutamate release in response to sensory stimulation. Distinct iGluSnFR3 fluctuations were observed in localized patches, and statistical analysis confirmed robust increases in iGluSnFR3 % ΔF/F upon sensory stimulation. The GluTrooper enables the visualization of glutamate dynamics across multiple imaging modalities, facilitating the investigation of glutamatergic signaling from large-scale brain networks down to subcellular

microdomains. Taking advantage of the Cre/lox recombination system, the GluTrooper can be crossed with a wide array of Cre-driver lines, permitting cell type-specific interrogation of glutamate dynamics under both physiological and pathophysiological conditions in acute and, most importantly, longitudinal investigations.

Material and methods

Immunohistochemistry

Mice were deeply anesthetized and transcardially perfused with ice-cold 4% paraformaldehyde (PFA) in 0.1 M phosphate buffer. Brains were post-fixed in the same fixative for 24 hours at 4°C, then 100 µm sagittal slices where prepared using a Leica vibratome (Leica Biosystems, Germany). Sections were incubated with primary antibody (goat anti-GFP; Thermo Fisher Scientific, #600-101-215M) diluted in blocking solution overnight at 4°C to observe iGluSnFR3-expressing cells. After three PBS-T (0.05% Tween 20) washes, tissue was incubated with species-matched Alexa Fluor 488-conjugated secondary antibody (donkey anti-goat IgG (H+L); Thermo Fisher Scientific, #A-11055) diluted 1:500 in PBS-T and DAPI (Invitrogen, #D1306; 1:1000). Then, slices were washed 3 times for 20 minutes each prior to mounting.

Confocal microscopy

Confocal imaging was performed using a Leica Stellaris 5 system (Leica Microsystems, Wetzlar, Germany) equipped with 40× (NA 1.30) and 63× (NA 1.40) oil-immersion objectives. Z-stacks were acquired at 2,048 × 2,048-pixel resolution with 0.65 µm z-intervals. Four neuroanatomically distinct regions (somatosensory cortex, hippocampus, olfactory bulb, and cerebellum) were systematically imaged in both 3- and 12-month-old cohorts to evaluate age-dependent expression profiles. Post-acquisition processing utilized Leica LAS X software (v3.7.4, Leica Microsystems) to generate maximum intensity projections from raw z-stacks. For cross-regional comparisons, cerebellar iGluSnFR3 signals served as an internal control due to its lack of transcriptional factor Emx1. Comparison of fluorescence intensity between the different regions and age was done using Scikit-image (Python).

Chronic widefield window implantation

Multimodal widefield imaging was performed to simultaneously monitor extracellular glutamate dynamics and intrinsic optical signals (IOS) reflecting cortical hemodynamics, using a custom-built mesoscale imaging system. Cranial window preparation was conducted three days prior to imaging sessions. Animals were anesthetized with isoflurane (5% for induction, 2% for maintenance) in a gas mixture of 70% nitrous oxide and 30% oxygen, and positioned in a prone orientation in a stereotaxic frame (Stoelting). After removal of scalp and connective tissue, the skull was coated with a thin layer of transparent dental cement (Parkell C&B Superbond). A curved crystal glass coverslip (LabMaker) was then affixed over the intact skull using the same cement, and a custom head-fixation frame was attached around the window. Animals recovered for a minimum of 48 hours before imaging.

Awake widefield mesoscale imaging and sensory stimulation

Mice were briefly anesthetized with 4% isoflurane to allow head fixation onto a Gramophone-style holder (Femtonics) using the custom head frame. Sensory stimulation was delivered to the left whisker pad using a custom-built, Arduino-controlled whisker stimulator oscillating vertically at 2 Hz. Each session included a 4-minute habituation period followed by a 4-minute imaging protocol consisting of a 50-second baseline and four stimulation blocks (10 s stimulation, 20 s rest), concluding with a final rest period. Infrared video was recorded concurrently using a Basler camera. To prevent visual interference from the imaging system, a 3D-printed eye shield was placed over the animal’s eyes. Following video correction and ΔF/F extraction from the selected regions of interest, signals were analyzed using SciPy (Python). The left and right somatosensory cortices were identified using the Allen Brain Atlas (reference) as reference. After baseline correction, glutamate events were detected by calculating the mean trace and applying a threshold of 1.5 standard deviations to ensure that only true fluctuations were considered as events. Event detection was performed using SciPy, and statistical differences in detected peaks during baseline and stimulation in both somatosensory cortices were compared using GraphPad Prism. Bulk changes in ΔiGluSnFR3, ΔHbO, and ΔHbR were assessed by comparing the 10 seconds before and after stimulation onset. The time to peak of these bulk changes was measured from the initiation of stimulation to the peak of the signals.

Cortical Spreading Depolarization

To observe CSD, mice were administered medetomidine (0.05 mg/kg, i.p.) five minutes prior to induction with 5% isoflurane delivered in a gas mixture of 70% nitrous oxide and 30% oxygen. After 1 minute, animals were placed in a stereotaxic frame, and isoflurane was gradually reduced to 1.5% for 140 seconds, followed by 0.75% for an additional 2 minutes to achieve a stable anesthetic state suitable for imaging. A small craniotomy was performed approximately one hour prior to imaging, positioned caudo-laterally to the primary imaging window, and filled with sterile phosphate-buffered saline (PBS). Following a 2-minute baseline period, CSD was induced by replacing the PBS with 1M KCl for 10 seconds, after which PBS was promptly reintroduced. Imaging continued for an additional 10 minutes, resulting in a total recording time of 12 minutes. Successful induction of CSD was verified through intrinsic optical signal (IOS) monitoring. Immediately after imaging, animals were sacrificed. To quantify changes in glutamate dynamics, the mean ΔiGluSnFR3, ΔHbO, and ΔHbR signal from all defined regions of interest was calculated and compared between the baseline and CSD periods using GraphPad Prism.

Pre-processing of widefield imaging data analysis

All image processing and analyses were performed using MATLAB (Mathworks, R2016b), with additional custom scripts written in Python (version 3.11.3) for extended analyses and visualization tasks. Briefly, acquired images underwent motion correction and alignment, background fluorescence subtraction, and normalization of fluorescence signals to the mean intensity across each recording for individual pixels (ΔF/F).

Chronic cranial window implantation

Before surgery, all instruments were sterilized using a glass-bead sterilizer (Fine Science Tools). Mice were anesthetized via intraperitoneal injection of a mixture containing medetomidine (0.5 mg/kg), midazolam (5 mg/kg), and fentanyl (0.05 mg/kg). Once anesthetized, animals were placed on a heating pad maintained at 37 °C, and their heads were secured in a stereotactic frame. To protect the eyes from drying, ophthalmic ointment was applied. The scalp was disinfected with 70% ethanol and

incised to expose the skull. The periosteum was gently removed with a scalpel. A 4 mm diameter craniotomy was outlined above the somatosensory cortex using a biopsy punch. To stabilize the surrounding skull area, a thin layer of dental adhesive (iBond Self Etch, Heraeus Kulzer) was applied and cured using an LED polymerization lamp (Demi Plus, Kerr). A dental drill (Schick Technikmaster C1, Pluradent) was then used to thin the bone along the marked region. After moistening the area with sterile phosphate-buffered saline, the bone flap was carefully lifted with forceps.

A circular glass coverslip (4 mm diameter) was placed over the craniotomy and secured to the skull using histoacryl adhesive (Aesculap). The remaining exposed skull was coated with dental acrylic (Tetric Evoflow A1 Fill, Ivoclar Vivadent), and a custom-made head-post was affixed adjacent to the window to allow for stable head fixation during later imaging sessions. Upon completion of the procedure, mice were given a subcutaneous injection of the analgesic carprofen (7.5 mg/kg body weight). Anesthesia was then reversed with intraperitoneal administration of atipamezole (2.5 mg/kg), naloxone (1.2 mg/kg), and flumazenil (0.5 mg/kg). Animals were placed in a warming chamber set at 35 °C and monitored until full recovery. In vivo imaging experiments began two to three weeks after surgery.

In vivo Two-Photon microscopy

Two-photon glutamate imaging was performed two weeks following cranial window implantation to allow for complete tissue recovery. Experiments were conducted using an Atlas two-photon microscope (Femtonics) equipped with a Chameleon Ultra tunable laser (Coherent) and a 16× water immersion objective (Nikon, NA 0.8). The iGluSnFR3 sensor was excited at 940 nm with fluorescence emission collected between 500-550 nm. Laser power was carefully maintained at approximately 40 mW below the objective to prevent tissue damage. Awake mice were positioned on a circular head-fixation platform (Gramophone, Femtonics Ltd) and allowed to habituate for 10 minutes prior to recording. Time-lapse imaging was acquired at 10 Hz with 512 × 512-pixel resolution at cortical depths of 150-200 µm below the surface. Each recording session began with a 1-minute baseline period, followed by controlled whisker stimulation delivered via Picospritzer (Parker-Hannifin Corporation) at 5 Hz frequency with 80 ms pulse duration for 10 seconds. All image processing and quantitative analyses were conducted post imaging acquisition.

Two-photon glutamate imaging analysis

Motion correction was first performed using the NoRMCorre algorithm [32] to reduce movement-related artifacts in the imaging data. After stabilization, time-lapse sequences were imported into Fiji, where regions of interest corresponding to glutamate-release areas were manually identified and fluorescence traces were extracted from each patch. For each labeled region, changes in ΔF/F glutamate levels were quantified by comparing the five seconds preceding stimulation with the peak detected during whisker stimulation. All statistical analyses were conducted using GraphPad Prism to assess differences in glutamate dynamics between experimental conditions.

References

1. DeFelipe J, Marco P, Busturia I, Merchán-Pérez A: Estimation of the number of synapses in the cerebral cortex: methodological considerations. Cereb Cortex 1999, 9(7):722-732.
2. Calì C, Wawrzyniak M, Becker C, Maco B, Cantoni M, Jorstad A, Nigro B, Grillo F, De Paola V, Fua P et al: The effects of aging on neuropil structure in mouse somatosensory cortex-A 3D electron microscopy analysis of layer 1. PLoS One 2018, 13(7):e0198131.
3. Wen Y, Dong Z, Liu J, Axerio-Cilies P, Du Y, Li J, Chen L, Zhang L, Liu L, Lu J et al: Glutamate and GABA(A) receptor crosstalk mediates homeostatic regulation of neuronal excitation in the mammalian brain. Signal Transduct Target Ther 2022, 7(1):340.
4. Aggarwal A, Liu R, Chen Y, Ralowicz AJ, Bergerson SJ, Tomaska F, Mohar B, Hanson TL, Hasseman JP, Reep D et al: Glutamate indicators with improved activation kinetics and localization for imaging synaptic transmission. Nat Methods 2023, 20(6):925-934.
5. Marvin JS, Scholl B, Wilson DE, Podgorski K, Kazemipour A, Müller JA, Schoch S, Quiroz FJU, Rebola N, Bao H et al: Stability, affinity, and chromatic variants of the glutamate sensor iGluSnFR. Nat Methods 2018, 15(11):936-939.
6. Soares C, Trotter D, Longtin A, Béïque JC, Naud R: Parsing Out the Variability of Transmission at Central Synapses Using Optical Quantal Analysis. Front Synaptic Neurosci 2019, 11:22.
7. Hao Y, Toulmé E, König B, Rosenmund C, Plested AJR: Targeted sensors for glutamatergic neurotransmission. Elife 2023, 12.
8. Tian L, Hires SA, Mao T, Huber D, Chiappe ME, Chalasani SH, Petreanu L, Akerboom J, McKinney SA, Schreiter ER et al: Imaging neural activity in worms, flies and mice with improved GCaMP calcium indicators. Nat Methods 2009, 6(12):875-881.
9. Zariwala HA, Borghuis BG, Hoogland TM, Madisen L, Tian L, De Zeeuw CI, Zeng H, Looger LL, Svoboda K, Chen TW: A Cre-dependent GCaMP3 reporter mouse for neuronal imaging in vivo. J Neurosci 2012, 32(9):3131-3141.
10. Dana H, Chen TW, Hu A, Shields BC, Guo C, Looger LL, Kim DS, Svoboda K: Thy1-GCaMP6 transgenic mice for neuronal population imaging in vivo. PLoS One 2014, 9(9):e108697.
11. Gorski JA, Talley T, Qiu M, Puelles L, Rubenstein JL, Jones KR: Cortical excitatory neurons and glia, but not GABAergic neurons, are produced in the Emx1-expressing lineage. J Neurosci 2002, 22(15):6309-6314.
12. Soriano P: Generalized lacZ expression with the ROSA26 Cre reporter strain. Nat Genet 1999, 21(1):70-71.
13. Srinivas S, Watanabe T, Lin CS, William CM, Tanabe Y, Jessell TM, Costantini F: Cre reporter strains produced by targeted insertion of EYFP and ECFP into the ROSA26 locus. BMC Dev Biol 2001, 1:4.
14. Gulisano M, Broccoli V, Pardini C, Boncinelli E: Emx1 and Emx2 show different patterns of expression during proliferation and differentiation of the developing cerebral cortex in the mouse. Eur J Neurosci 1996, 8(5):1037-1050.
15. Guo H, Hong S, Jin XL, Chen RS, Avasthi PP, Tu YT, Ivanco TL, Li Y: Specificity and efficiency of Cre-mediated recombination in Emx1-Cre knock-in mice. Biochem Biophys Res Commun 2000, 273(2):661-665.

16. Leao AA: Further observations on the spreading depression of activity in the cerebral cortex. J Neurophysiol 1947, 10(6):409-414.
17. Branston NM, Strong AJ, Symon L: Extracellular potassium activity, evoked potential and tissue blood flow. Relationships during progressive ischaemia in baboon cerebral cortex. J Neurol Sci 1977, 32(3):305-321.
18. Strong AJ, Venables GS, Gibson G: The cortical ischaemic penumbra associated with occlusion of the middle cerebral artery in the cat: 1. Topography of changes in blood flow, potassium ion activity, and EEG. J Cereb Blood Flow Metab 1983, 3(1):86-96.
19. Nedergaard M, Astrup J: Infarct rim: effect of hyperglycemia on direct current potential and [14C]2-deoxyglucose phosphorylation. J Cereb Blood Flow Metab 1986, 6(5):607-615.
20. Oka H, Kako M, Matsushima M, Ando K: Traumatic spreading depression syndrome. Review of a particular type of head injury in 37 patients. Brain 1977, 100(2):287-298.
21. Rogatsky G, Mayevsky A, Zarchin N, Doron A: Continuous multiparametric monitoring of brain activities following fluid-percussion injury in rats: preliminary results. J Basic Clin Physiol Pharmacol 1996, 7(1):23-43.
22. Obrenovitch TP, Urenjak J: Is high extracellular glutamate the key to excitotoxicity in traumatic brain injury? J Neurotrauma 1997, 14(10):677-698.
23. Vespa PM, McArthur D, O'Phelan K, Glenn T, Etchepare M, Kelly D, Bergsneider M, Martin NA, Hovda DA: Persistently low extracellular glucose correlates with poor outcome 6 months after human traumatic brain injury despite a lack of increased lactate: a microdialysis study. J Cereb Blood Flow Metab 2003, 23(7):865-877.
24. Østergaard L, Dreier JP, Hadjikhani N, Jespersen SN, Dirnagl U, Dalkara T: Neurovascular coupling during cortical spreading depolarization and -depression. Stroke 2015, 46(5):1392-1401.
25. Mohajerani MH, Aminoltejari K, Murphy TH: Targeted mini-strokes produce changes in interhemispheric sensory signal processing that are indicative of disinhibition within minutes. Proc Natl Acad Sci U S A 2011, 108(22):E183-191.
26. Wang Y, Chen Z, Ma G, Wang L, Liu Y, Qin M, Fei X, Wu Y, Xu M, Zhang S: A frontal transcallosal inhibition loop mediates interhemispheric balance in visuospatial processing. Nat Commun 2023, 14(1):5213.
27. Sugaya E, Takato M, Noda Y: Neuronal and glial activity during spreading depression in cerebral cortex of cat. J Neurophysiol 1975, 38(4):822-841.
28. Somjen GG: Mechanisms of spreading depression and hypoxic spreading depression-like depolarization. Physiol Rev 2001, 81(3):1065-1096.
29. Sawant-Pokam PM, Suryavanshi P, Mendez JM, Dudek FE, Brennan KC: Mechanisms of Neuronal Silencing After Cortical Spreading Depression. Cereb Cortex 2017, 27(2):1311-1325.
30. Henninger N, Heimann A, Kempski O: Electrophysiology and neuronal integrity following systemic arterial hypotension in a rat model of unilateral carotid artery occlusion. Brain Res 2007, 1163:119-129.
31. Chaigneau E, Oheim M, Audinat E, Charpak S: Two-photon imaging of capillary blood flow in olfactory bulb glomeruli. Proc Natl Acad Sci U S A 2003, 100(22):13081-13086.

32. Pnevmatikakis EA, Giovannucci A: NoRMCorre: An online algorithm for piecewise rigid motion correction of calcium imaging data. J Neurosci Methods 2017, 291:83-94.

Author Contributions

BW and WW generated the mouse line. GMC, DPV, PF, SF, FG and AC performed the experiments. GMC, DPV and PM analyzed the data and performed statistical analysis. GMC, DPV and NP drafted the manuscript.

Competing Interests

The authors declare no competing interests.

Data availability

The data generated during the study are available from the corresponding author upon request.

Figures

Figure 1

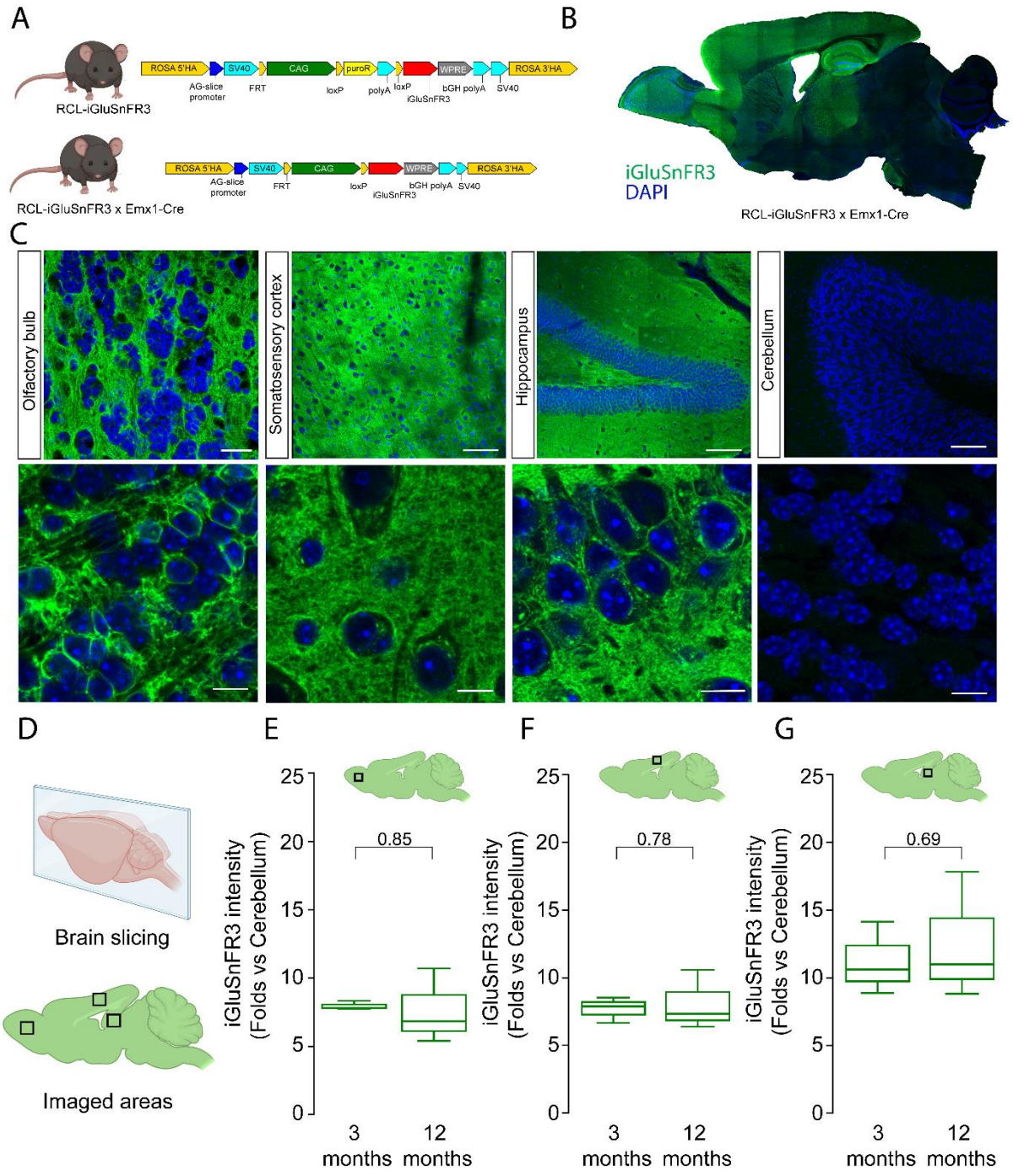

Figure 2

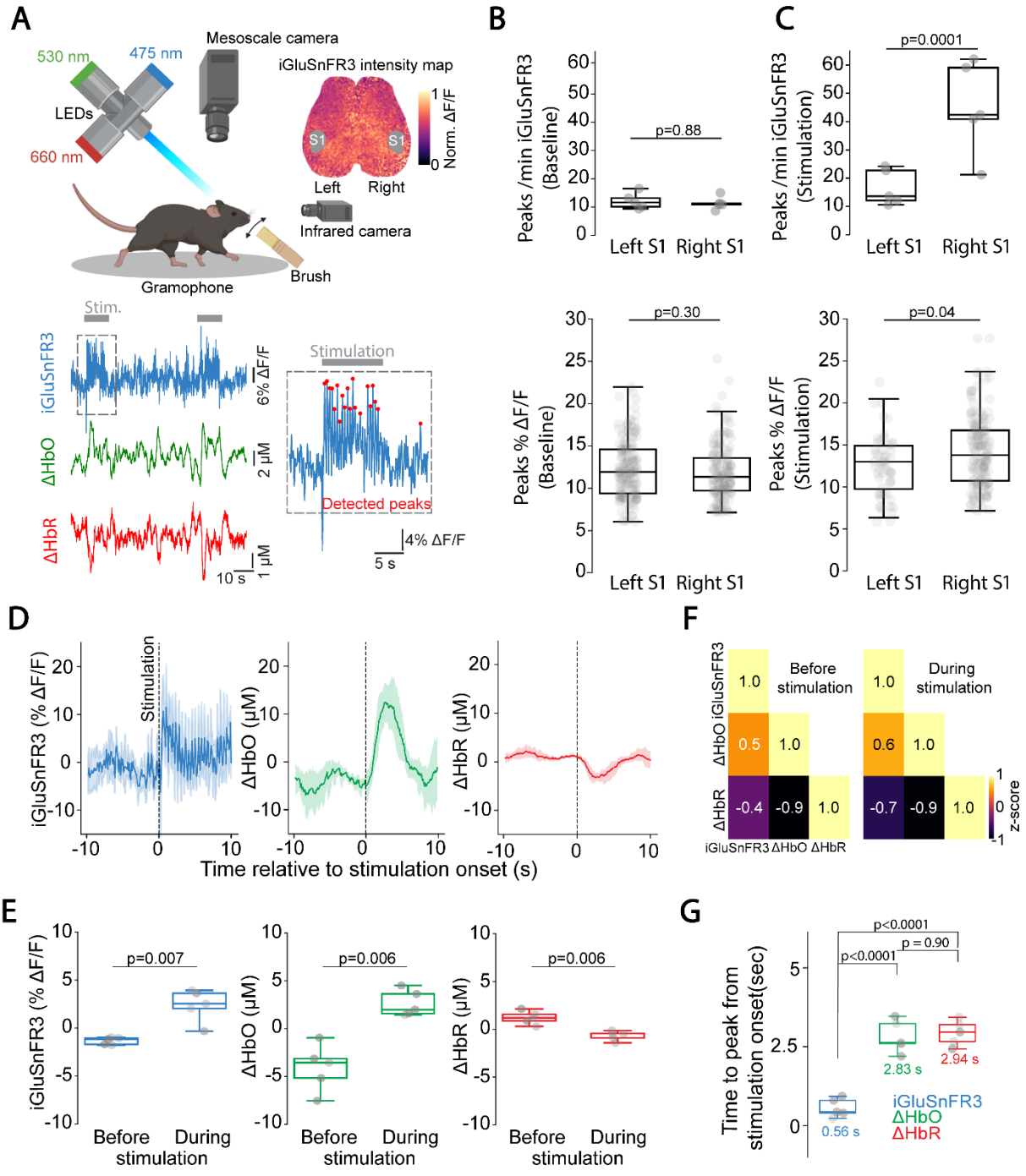
A
530 nm
475 nm
LEDs
660 nm
Mesoscale camera
iGluSnFR3 intensity map
S1
S1
Left
Right
1
0
Norm. ΔF/F
Infrared camera
Brush
Gramophone
Stim.
iGluSnFR3
ΔHbO
ΔHbR
6% ΔF/F
2 μM
1 μM
10 s
Stimulation
Detected peaks
4% ΔF/F
5 s
B
Peaks /min iGluSnFR3 (Baseline)
p=0.88
Left S1
Right S1
C
Peaks /min iGluSnFR3 (Stimulation)
p=0.0001
Left S1
Right S1
Peaks % ΔF/F (Baseline)
p=0.30
Left S1
Right S1
Peaks % ΔF/F (Stimulation)
p=0.04
Left S1
Right S1
D
iGluSnFR3 (% ΔF/F)
Stimulation
ΔHbO (μM)
ΔHbR (μM)
Time relative to stimulation onset (s)
F
Before stimulation
During stimulation
ΔHbO iGluSnFR3
ΔHbR
1.0
0.5
1.0
-0.4
-0.9
1.0
0.6
-0.7
z-score
iGluSnFR3 ΔHbO ΔHbR
E
iGluSnFR3 (% ΔF/F)
p=0.007
ΔHbO (μM)
p=0.006
ΔHbR (μM)
p=0.006
Before stimulation
During stimulation
G
Time to peak from stimulation onset(sec)
p<0.0001
p = 0.90
p<0.0001
2.83 s
2.94 s
0.56 s
iGluSnFR3
ΔHbO
ΔHbR

Figure 3

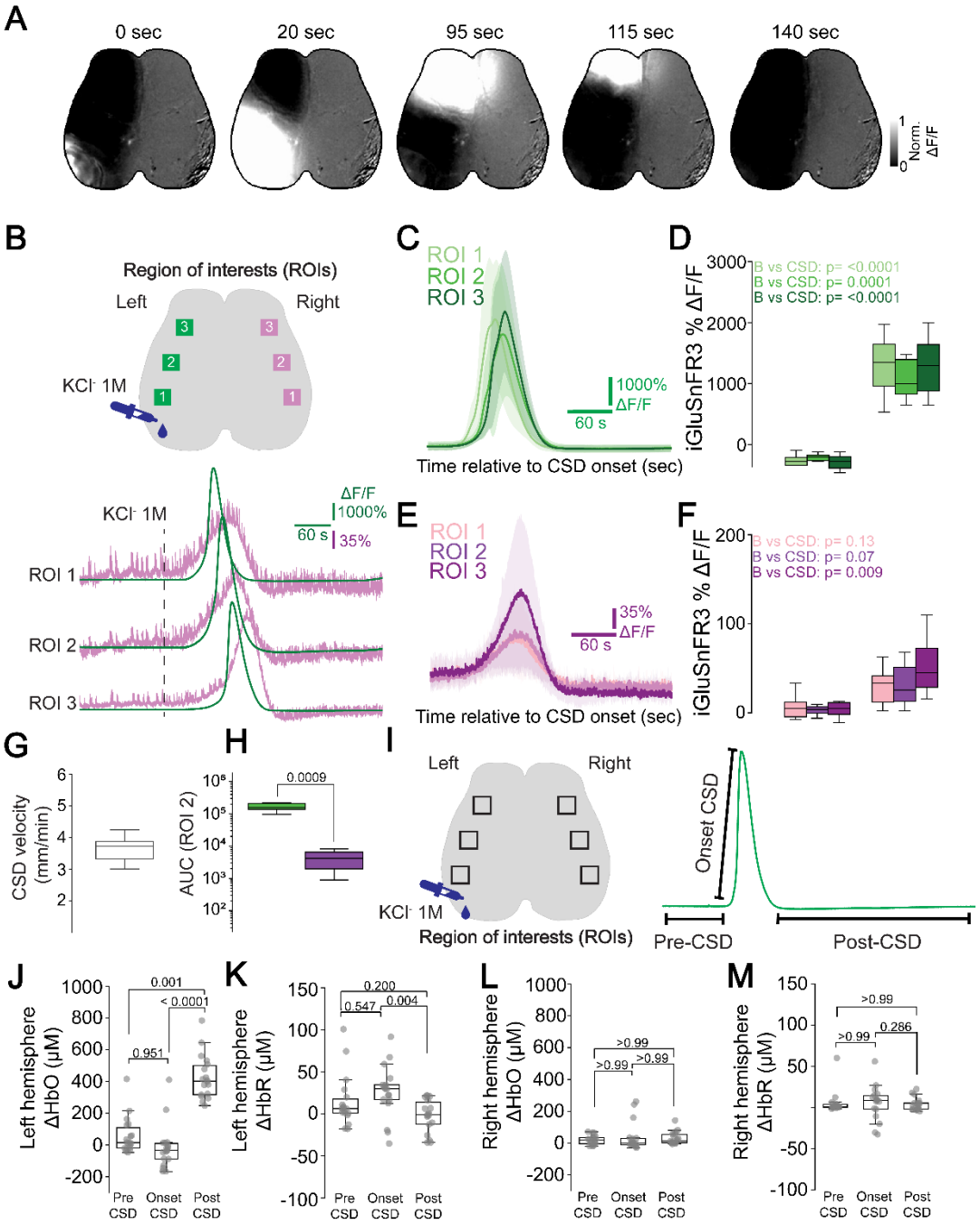
A
0 sec
20 sec
95 sec
115 sec
140 sec
1
Norm. ΔF/F
0
B
Region of interests (ROIs)
Left
Right
KCl 1M
C
ROI 1
ROI 2
ROI 3
1000% ΔF/F
60 s
Time relative to CSD onset (sec)
D
iGluSnFR3 % ΔF/F
B vs CSD: p= <0.0001
B vs CSD: p= 0.0001
B vs CSD: p= <0.0001
KCl 1M
ΔF/F
1000%
60 s
35%
ROI 1
ROI 2
ROI 3
E
ROI 1
ROI 2
ROI 3
35% ΔF/F
60 s
Time relative to CSD onset (sec)
F
iGluSnFR3 % ΔF/F
B vs CSD: p= 0.13
B vs CSD: p= 0.07
B vs CSD: p= 0.009
G
CSD velocity (mm/min)
H
AUC (ROI 2)
0.0009
I
Left
Right
KCl 1M
Region of interests (ROIs)
Onset CSD
Pre-CSD
Post-CSD
J
Left hemisphere ΔHbO (μM)
0.001
< 0.0001
0.951
Pre CSD
Onset CSD
Post CSD
K
Left hemisphere ΔHbR (μM)
0.200
0.547
0.004
L
Right hemisphere ΔHbO (μM)
>0.99
>0.99
>0.99
M
Right hemisphere ΔHbR (μM)
>0.99
>0.99
0.286

Figure 4

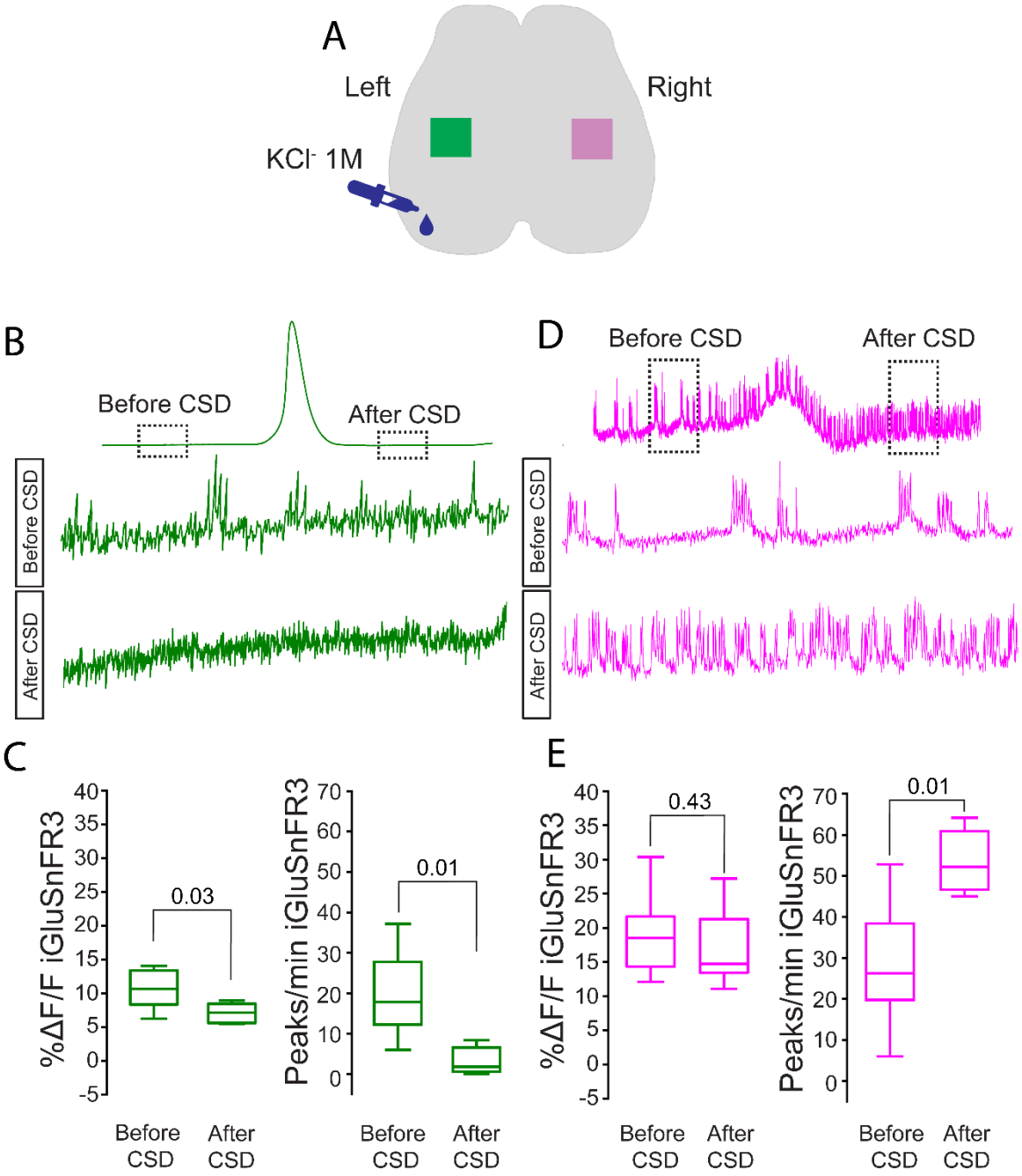
A
Left
Right
KCl 1M
B
Before CSD
After CSD
Before CSD
After CSD
D
Before CSD
After CSD
Before CSD
After CSD
C
%ΔF/F iGluSnFR3
0.03
Before CSD
After CSD
Peaks/min iGluSnFR3
0.01
Before CSD
After CSD
E
%ΔF/F iGluSnFR3
0.43
Before CSD
After CSD
Peaks/min iGluSnFR3
0.01
Before CSD
After CSD

Figure 5

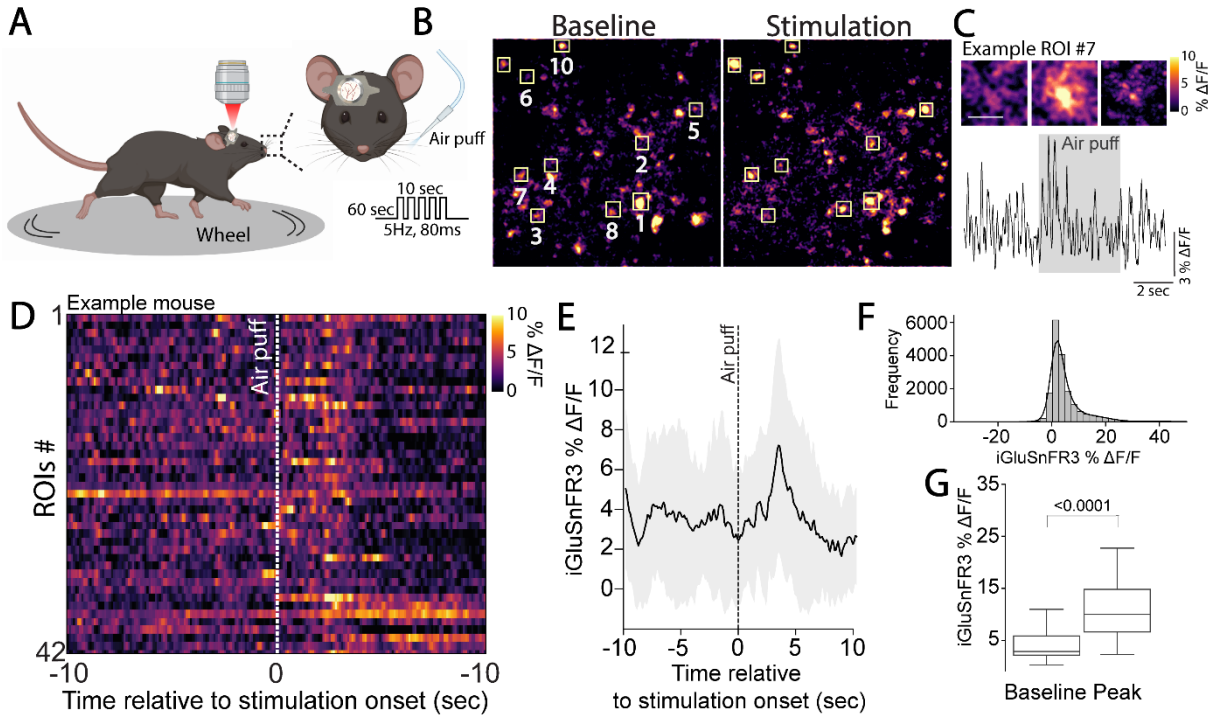
A
Wheel
Air puff
10 sec
60 sec
5Hz, 80ms
B
Baseline
Stimulation
C
Example ROI #7
% ΔF/F
Air puff
3 % ΔF/F
2 sec
D
Example mouse
ROIs #
Air puff
% ΔF/F
Time relative to stimulation onset (sec)
E
iGluSnFR3 % ΔF/F
Air puff
Time relative
to stimulation onset (sec)
F
Frequency
iGluSnFR3 % ΔF/F
G
iGluSnFR3 % ΔF/F
<0.0001
Baseline Peak

Figure legends

Figure 1

A) Schematic illustrating the genetic design of the GluTrooper mouse line (top) and the resulting construct following crossbreeding with Emx1-Cre mice (bottom). **B)** Representative sagittal brain section showing widespread, pan-cortical expression of iGluSnFR3. **C)** Representative images from four distinct brain regions: olfactory bulb, somatosensory cortex, hippocampus, and cerebellum (Top Scale bars = Olfactory bulb: 20 µm; Somatosensory cortex: 80 µm; Hippocampus: 80 µm; Cerebellum: 80 µm. Bottom Scale bars: all scale bars = 10 µm). Note the lack of iGluSnFR3 expression in the Cerebellum due to lack of transcription factor Emx1. **D)** Schematic overview of the brain slicing strategy (top) and the four analyzed brain regions (bottom). **E-G)** Quantification of iGluSnFR3 fluorescence intensity in the somatosensory cortex, hippocampus, and olfactory bulb, using the cerebellum as an internal control. Data are presented as fold-change in signal intensity relative to cerebellar levels (n = 3 mice per group). All data are displayed as median and the interquartile range (25th to 75th percentiles), whiskers reach to the minimum and maximum values of the distribution. Schematic illustrations are created with BioRender.com. No significant differences were observed between age groups (Somatosensory cortex: $p = 0.78$; Hippocampus: $p = 0.69$; Olfactory bulb: $p = 0.85$; Student's t-test).

Figure 2

A) Schematic of the widefield imaging setup and experimental paradigm (left panel), with a representative widefield fluorescence image highlighting the bilateral somatosensory cortex (S1) regions of interest (right panel). **B)** Quantification of spontaneous iGluSnFR3 transient frequency (peaks/min, top panel; $p = 0.88$) and amplitude (bottom panel, $p = 0.30$) in left vs. right S1 cortices. **C)** Stimulation-evoked responses: iGluSnFR3 transient frequency (peaks/min, top panel, $p = 0.0001$) and amplitude (bottom panel, $p = 0.04$) in bilateral S1 during sensory stimulation. **D)** Simultaneous recording of glutamate release (iGluSnFR3 %ΔF/F), hemodynamic responses (ΔHbO = oxygenated hemoglobin; ΔHbR = deoxygenated hemoglobin), and stimulus timeline following stimulation onset. **E)** iGluSnFR3 signaling intensity and hemodynamic parameters during prestimulus baseline vs. active stimulation periods (iGluSnFR3 %ΔF/F: $p = 0.007$; ΔHbO: $p = 0.006$; ΔHbR: $p = 0.006$). **F)** Correlation matrix of iGluSnFR3, ΔHbO, and ΔHbR during baseline and stimulation, showing increased coupling between glutamate and hemodynamic signals during stimulation (see color scale for z-score values). **G)** Time to peak of iGluSnFR3 %ΔF/F, ΔHbO and ΔHbR from stimulation onset (iGluSnFR3 vs ΔHbO: $p = <0.0001$; iGluSnFR3 vs ΔHbR: $p = <0.0001$). B-C-E-G: Data are displayed as median and the interquartile range (25th to 75th percentiles), whiskers reach to the minimum and maximum values of the distribution. D: Data are presented as mean ± 95% confidence interval. Statistical analysis by Student's t-test, z-score calculation and One-Way ANOVA followed by Dunn's post-hoc test.

Figure 3

A) Representative image series of the progression of the CSD in the left hemisphere. **B)** Schematic of bilateral regions of interest (ROIs) and KCl application site (top); representative iGluSnFR3 traces from the selected ROI (bottom). **C)** Glutamate dynamics (%ΔF/F iGluSnFR3) in the left ROI aligned to CSD onset. **D)** Comparison of mean iGluSnFR3 %ΔF/F in the left ROI during baseline (B) and CSD (ROI1 and 3: $p < 0.0001$; ROI2: $p = 0.0001$). **E)** Glutamate dynamics in the right ROI aligned to CSD onset. **F)** Comparison of mean iGluSnFR3 %ΔF/F in the right ROI during baseline and CSD (ROI1: $p = 0.13$; ROI2: $p = 0.007$; ROI3: $p = 0.009$). **G)** Quantification of CSD propagation velocity. H) Area under the curve (AUC) of glutamate transients in bilateral ROI2 (left vs right: $p = 0.0009$). **I)** Schematic of bilateral ROIs (left) and definition of three CSD phases (right). **J-K)** Quantification of ΔHbO (J) and ΔHbR (K) across CSD phases in the left hemisphere (For ΔHbO, Pre-CSD vs Post-CSD: $p = 0.001$; Onset-CSD vs Post-CSD: $p < 0.0001$; For ΔHbR, Onset-CSD vs Post-CSD: $p = 0.004$). **L-M)** Quantification of ΔHbO (L) and ΔHbR (M) across CSD phases in the right hemisphere (For ΔHbO, all comparisons: $p > 0.05$; For ΔHbR, all comparisons: $p > 0.05$). C-E: C-G: Data are presented as mean ± 95% confidence interval. D-F-G-H-J-K-L-M: data are displayed as median and interquartile range (25th–75th percentiles), whiskers reach to the minimum and maximum values of the distribution (n = 6 mice). Statistical analysis: D, F, H—Student's t-test; J, K, L, M: one-way ANOVA with Dunn's post hoc test.

Figure 4

A) Schematic representing the selected bilateral region of interest. **B)** Representative CSD from the left ROI (on the top) with zooming on before and after CSD (on the bottom). **C)** Amplitude of detected glutamate events before and after CSD (on the left, $p = 0.03$) and number of detected peaks/min (on the right, $p = 0.62$). **D)** Representative CSD from the right ROI (on the top) with zooming on before and after CSD (on the bottom). **E)** Amplitude of detected glutamate events before and after CSD on the right ROI (on the left, $p = 0.40$) and number of detected peaks/min (on the right, $p = 0.03$). All data are displayed as median and interquartile range (25th–75th percentiles), whiskers reach to the minimum and maximum values of the distribution; n = 6 mice. Statistical analysis: C, E) Student's t-test

Figure 5

A) Experimental setup schematic and stimulation paradigm. **B)** Representative fluorescence field of view during baseline (left) and active stimulation (right). **C)** Example ROI (top) with corresponding iGluSnFR3 %ΔF/F dynamics during stimulation (bottom). **D)** Rastermap of all detected ROIs color-coded by iGluSnFR3 %ΔF/F intensity in an exemplary mouse. **E–F)** Distribution of iGluSnFR3 response magnitudes during stimulation (E) and across the entire experiment. **F)**. Comparison of iGluSnFR3 %ΔF/F between baseline and peak response periods ($p < 0.0001$; Student's t-test). E: Data are presented as mean ± SD; G: Data are displayed as median and the

interquartile range (25th to 75th percentiles), whiskers reach to the minimum and maximum values of the distribution

Supplementary figures

Suppl. Figure 1

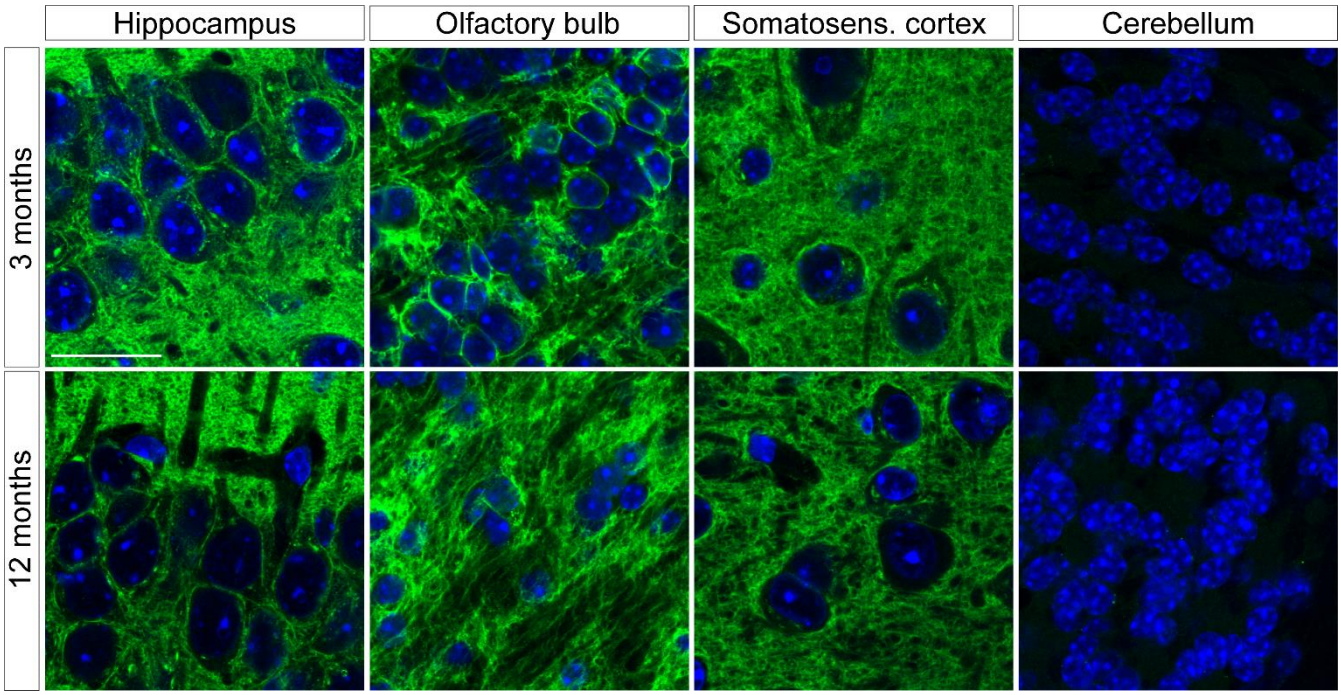

Supplementary figure legend

Supplementary figure 1

Representative images of 4 different brain regions (Hippocampus, olfactory bulb, Somatosensory cortex and Cerebellum) at two different developmental stages: 3 and 12 months.

4. Discussion

4.1 Study I: Stroke leads to chronic contralateral neuronal suppression

4.1.2 Main findings of the study

Our findings provide novel insights into the mechanisms by which ischemic stroke exerts its effects on distant, functionally connected brain regions, leading to the phenomenon known as diaschisis. While traditional views have emphasized diaschisis as a passive consequence of disrupted input to structurally intact areas, our data suggest a far more active and dynamic reorganization of neural circuits in the contralateral hemisphere over a period of three months. Specifically, we identify contralateral transcallosal neurons, those that project to the infarcted hemisphere, as a key cellular substrate of diaschisis. Ninety days post-ischemic injury, these neurons do not undergo retrograde degeneration, as one might expect from classical deafferentation models, but instead exhibit morphological preservation and even show chronic functional hyperactivity.

The sustained number of transcallosal neurons suggests that they remain viable and capable of contributing to network function. Notably, this hyperactivation emerges by 21 days post-ischemia and coincides with a pronounced shift in the excitatory-inhibitory balance of the contralesional cortex, evident at ninety days post-stroke. Immunohistochemical analyses revealed that, three months post stroke, disconnected transcallosal neurons displayed a decreased number of inhibitory synapses and an increase in excitatory synapses, culminating in a nearly two-fold increase in the excitation/inhibition ratio. This synaptic remodeling aligns with previous observations in models of cortical plasticity and injury, where deafferented neurons undergo homeostatic synaptic scaling to compensate for lost input [220].

However, rather than restoring balance, our data suggest that this compensation becomes maladaptive. Functionally, this is evidenced by the marked increase in spontaneous calcium transients observed specifically in transcallosal neurons from three weeks post-stroke operation, while neighboring local neurons remained functionally stable for the entire longitudinal investigation. The selective nature of this hyperexcitability strongly implicates the loss of callosal input as a driving factor, rather

than a generalized cortical response to stroke. The hyperactive state of transcallosal neurons appears to exert downstream effects on their local network, promoting a widespread shift toward inhibition.

Over the course of three months post-stroke, we observed a progressive increase in GAD65-67+ inhibitory synapses throughout layers II–V of the contralateral barrel cortex, accompanied by a substantial decrease in vGlut1+ synapses. These network-level changes suggest that hyperactive transcallosal neurons may drive inhibitory remodeling via activity-dependent mechanisms, possibly involving interneuron recruitment or long-term changes in synaptic transmission. This hypothesis is further supported by the molecular analysis which showed increased expression of $GABA_A$ receptor subunits mediating tonic inhibition, which has been linked to long-term suppression of cortical excitability in other injury models [221]. Functionally, this remodeling translates to a progressive decline in the responsiveness of the contralateral cortex to sensory stimulation.

Longitudinal calcium imaging revealed a gradual attenuation of whisker-evoked responses in local neurons of the contralateral barrel field, beginning twenty-one days post-stroke and reaching a significant 36% reduction by seventy-seven days. In contrast, transcallosal neurons did not exhibit this stimulus-induced suppression, maintaining consistent sensory-evoked responses throughout the entire experimental timeline. This dissociation highlights the paradoxical nature of diaschisis: while certain neurons become hyperexcitable in response to lost input, their downstream influence suppresses normal stimulus-driven activity in the surrounding network. Notably, this functional inhibition mirrors findings in stroke patients, where diaschisis is characterized by hypometabolism and hypoperfusion in structurally intact areas [23].

Indeed, our data suggest that impaired neurovascular coupling may be one of the terminal outcomes of this maladaptive circuit remodeling. Using laser speckle contrast imaging, we found that the CBF response to whisker stimulation was initially intact but declined significantly three months post-stroke, mirroring the functional and structural alterations described above.

This finding suggests that inhibitory remodeling not only impairs neural responsiveness but also disrupts the neurovascular mechanisms required for functional perfusion.

Chronic hypoperfusion of the contralateral cortex may further exacerbate neural dysfunction, contributing to the sustained nature of diaschisis and its resistance to spontaneous recovery. Collectively, our data support a model in which diaschisis is not merely a passive reflection of lost input but an active, self-perpetuating state of network imbalance triggered by the maladaptive remodeling of transcallosal neurons to deafferentation.

These findings build on previous studies demonstrating that transcallosal projections play a critical role in interhemispheric inhibition [222-224]. Our identification of transcallosal hyperexcitability as a key driver of diaschisis opens the door to new therapeutic strategies aimed at restoring excitatory-inhibitory balance in the intact hemisphere. Potential approaches might include modulation of tonic GABAergic signaling, targeted neuromodulation of transcallosal circuits, or activity-dependent plasticity-based rehabilitation protocols. In conclusion, our study provides a comprehensive mechanistic framework for understanding diaschisis at the cellular, synaptic, and functional levels. By focusing on the role of transcallosal neurons, we reveal a novel pathway by which distant effects of stroke can lead to chronic cortical dysfunction, and suggest that targeting these maladaptive changes may offer new avenues for improving long-term outcomes in stroke patients.

4.1.3 Limitations of the study

While our study provides important insights into the mechanisms of diaschisis and transcallosal remodeling after stroke, several limitations must be considered when interpreting these findings. First, although our approach enabled cell-type-specific identification of transcallosal neurons using a retrograde viral labelling strategy, we cannot entirely exclude the possibility of missed transcallosal cells.

In fact, although we carefully restricted viral injections to the future infarct core and confirmed accurate targeting through histological analysis, AAVs cannot label 100% of the targeted cell population. As a result, some transcallosal neurons may have remained unlabeled and we may have miscategorized neurons when imaging their activity in the contralateral hemisphere. Future studies using intersectional genetic labeling strategies may help refine the specificity of this population and allow for dissection of projection subtypes. Although the anatomical and temporal progression

strongly suggests that hyperactive transcallosal neurons contribute to downstream inhibition of the contralateral cortex, we did not perform network manipulations, such as optogenetics or chemogenetics inhibition/activation of these neuronal population, thus being able to directly test this hypothesis. Without such interventions, it remains possible that different cell populations could influence the excitatory-inhibitory unbalance we observed in the contralesional hemisphere. Incorporating circuit-level manipulations in future work would strengthen the mechanistic conclusions of this study.

Furthermore, our interpretation of functional inhibition is based largely on calcium imaging readouts and immunohistochemical quantification of inhibitory synapses and GABA receptor subunits. While these are well-established proxies for neuronal activity and inhibitory remodeling, they are inherently indirect.

Calcium indicators such as GCaMP6s have limitations in detecting subthreshold synaptic activity or tonic inhibition, which is particularly relevant in the context of altered $GABA_A$ receptor expression [225]. Furthermore, although we observed increased expression of $GABA_A$ receptor subunits associated with tonic inhibition, we did not directly measure GABA levels, tonic currents, or miniature inhibitory postsynaptic currents [225].

Electrophysiological validation of these changes would provide a more direct measure of functional inhibition and could distinguish between synaptic and extra-synaptic forms of GABAergic transmission. Similarly, our observation of impaired neurovascular coupling was inferred from bulk CBF responses using laser speckle imaging. The combination of two-photon imaging of vascular dynamics or oxygen-sensitive probes could clarify whether capillary-level responses or oxygen extraction are also disrupted in parallel with the observed neuronal suppression.

A further limitation lies in the spatial resolution and coverage of our imaging techniques. While we performed longitudinal two-photon calcium imaging in an identified population of neurons and combined this with widefield measurements of CBF, both approaches are constrained in different ways:

Two-photon microscopy allows for single-cell resolution but is limited to small fields of view and cortical layers. As a result, we may have overlooked deeper-layer

contributions or more diffuse changes across widespread cortical regions. On the other hand, widefield imaging of CBF provides better spatial coverage but lacks cell-type specificity. An integrated mesoscale approach, using widefield calcium imaging in transgenic mice such as Thy1-GCaMP6s [107], could provide a better understanding of the spatiotemporal dynamics in the contralesional hemisphere. Moreover, while our study focused on transcallosal glutamatergic neurons and their influence on local excitatory and inhibitory populations, we did not directly assess the role of other projection systems or interneuron subtypes in mediating diaschisis. For example, thalamocortical projections also undergo compensatory or maladaptive changes post-stroke, potentially influencing cortical responsiveness and recovery [226].

Similarly, interneuron subtypes such as parvalbumin-, somatostatin-, or vasoactive intestinal peptide (VIP)-expressing cells were not examined in this study but are likely to play distinct roles in shaping cortical excitability and inhibitory balance [227-229]. Expanding the cellular scope in future investigations will provide further insight into the circuit-level alterations contributing to diaschisis. Additionally, the behavioral relevance of our findings remains an important avenue for future research. While we observed robust structural and functional changes in the contralesional hemisphere, their direct link to behavioral impairments or recovery trajectories has yet to be established.

4.2 Study II: A novel glutamate reporter line for whole-brain monitoring of glutamate dynamics

4.2.1 Main findings of the study

In this study, we generated GluTrooper, a novel ROSA26 knock-in mouse model designed for Cre-dependent expression of the genetically encoded glutamate sensor iGluSnFR3 [184, 210, 230, 231]. This line provides stable, long-term, and spatially controlled labeling of glutamatergic neurons throughout the cortex and subcortical regions, enabling the longitudinal study of excitatory neurotransmission under both physiological and pathophysiological conditions. Traditional methods of glutamate imaging have largely relied on viral vector-based delivery of sensors such as iGluSnFR [184, 210], which, although effective, often result in inconsistent expression levels,

limited spatial spread, and cytotoxic effects due to high overexpression in a subset of neurons [107, 232].

By leveraging the ROSA26 locus and the strong, ubiquitous CAG promoter, the GluTrooper overcomes these limitations, offering a robust, reproducible, and non-toxic alternative for brain-wide glutamate imaging. Crossing our novel reporter line with Emx1-Cre mice, we observed efficient recombination and expression across the cortex, as well as in the hippocampus and olfactory bulb [233, 234]. The stability of sensor expression over time further enhances the utility of this model for chronic imaging paradigms, including longitudinal monitoring of synaptic function, learning, and plasticity. To validate the functionality of our novel glutamate reporter line, we employed widefield glutamate imaging in awake, head-fixed mice.

We confirmed that iGluSnFR3 expression was sufficiently bright and stable to permit high signal-to-noise recordings of both spontaneous and evoked glutamatergic dynamics. In the barrel cortex, sensory stimulation reliably evoked glutamate transients with high temporal precision and regional specificity. These recordings also revealed a tight coupling between cortical activation and glutamate release, reinforcing the validity of this sensor for monitoring neuronal output rather than general network excitability.

During our experimental approaches, we observed that glutamate transients temporally preceded hemodynamic responses, including changes in oxy- and deoxy-hemoglobin (ΔHbO and ΔHbR), highlighting the value of using direct optical sensors of neurotransmitter release, like iGluSnFR3, in disentangling the timing and directionality of neurovascular coupling. It also opens up new doors for investigating the role of excitatory signaling in regulating vascular responses under physiological and pathophysiological conditions.

Beyond physiological validation, we tested our novel reporter line in the context of cortical spreading depolarization, a hallmark of several neurological conditions including stroke, traumatic brain injury, and migraine [235]. Using three different LEDs, we were able to simultaneously track glutamate dynamics and hemodynamic responses across the cortex of both hemispheres. We identified three distinct phases,

baseline, CSD onset, and post-CSD, and extracted glutamate and vascular dynamics from holotypic regions of interest in both hemispheres.

As expected, CSD evoked a pronounced increase in glutamate concentration in the ipsilateral cortex, coupled with a complex hemodynamic response characterized by an initial hypoperfusion followed by delayed hyperemia. Moreover, following the observation of spontaneous glutamate dynamics before and post- CSD, we quantified a significant increase in the frequency of spontaneous contralateral glutamate events during the post-CSD phase.

This data shows the sensitivity of our novel glutamate reporter line in observing contralateral disinhibition, a phenomenon that can be triggered by unilateral lesion or brain injury [224, 236]. The ability to observe this phenomenon non-invasively, through direct imaging of glutamate release, provides a unique window into interhemispheric network dynamics during cortical perturbations. It also raises important questions about the role of contralateral plasticity in recovery or maladaptation following focal insults.

Taken together, our findings establish our novel glutamate reporter line as a reliable, flexible, and scalable tool for investigating glutamatergic signaling *in vivo*. This model enables chronic, high-fidelity imaging of glutamate transients across a wide range of spatial and temporal scales, overcoming many of the technical limitations inherent to viral delivery methods.

By allowing for longitudinal monitoring of cortical function, sensory processing, and interhemispheric communication, GluTrooper opens new opportunities for studying circuit-level excitatory dynamics under both physiological and pathophysiological conditions. Moreover, its compatibility with various Cre-driver lines makes it as a valuable tool for future studies focused on specific cell types or brain regions, further expanding our knowledge in neuroscience research.

4.2.2 Measuring extracellular glutamate

A major strength of our study lies in the development and characterization of a transgenic mouse line with Cre-dependent expression of the glutamate sensor iGluSnFR3, offering key advantages over traditional adeno-associated virus (AAV)-based delivery systems. While AAVs are widely used for *in vivo* expression of genetically encoded sensors due to their flexibility, ease of use, and cell-type specificity when combined with Cre driver lines or specific promoters, they present several notable limitations that can compromise long-term imaging studies [107, 232].

A major limitation of AAV-based approaches is the variability in transduction efficiency, which can differ markedly across brain regions, cell types, and even within a single injection site. The number of viral genome copies taken up per cell is also difficult to control, often resulting in spatial gradients of expression, higher near the injection site and diminishing with distance. Additionally, not all cell types are equally susceptible to AAV transduction, leading to potential biases in cell-type representation. These factors can produce uneven sensor expression across animals or between hemispheres, complicating both group-level comparisons and longitudinal studies. Moreover, AAV-mediated expression is typically restricted to a focal region surrounding the injection site, limiting its utility for widefield or mesoscopic imaging of distributed networks. In contrast, Cre-dependent transgenic strategies enable broader and more uniform expression in genetically defined cell populations, offering more comprehensive coverage for circuit-level investigations.

In the case of our novel glutamate reporter line crossed with Emx1-Cre, this results in pan-cortical expression in glutamatergic neurons, enabling whole-cortex observation of glutamate dynamics without the need for multiple injections or extensive surgical manipulations.

This is particularly advantageous for bilateral comparisons or chronic imaging over extended time periods, where AAV-based approaches may be limited by variability in expression levels and potential overexpression artifacts.

Moreover, AAV injection procedures carry their own risks, including local inflammation, tissue damage, or variability in depth targeting, which may confound experimental interpretations. By avoiding intracranial injections altogether, the v provides a cleaner

and more reproducible platform for studying both physiological and pathological glutamate dynamics. Finally, while AAVs provide some degree of flexibility in tuning expression levels via promoter selection or vector design, this often comes at the cost of complex vector construction or inconsistent results: High expression levels can lead to sensor overloading, substrate buffering effects, or saturation, while low expression levels may compromise signal detection.

Transgenic strategies, particularly those involving single-copy insertion at well-characterized loci like ROSA26, offer tighter control over expression, reducing the risk of toxicity or signaling disruption [237]. Importantly, by leveraging a standardized genetic background and a consistent recombination strategy, the GluTrooper supports longitudinal, reproducible studies and can be easily combined with other transgenic tools (e.g., reporters, activity modulators, or disease models), offering a high degree of experimental flexibility.

While AAVs remain valuable for acute or region-specific manipulations, transgenic approaches are superior for long-term, whole-brain functional imaging with minimal variability and maximum reproducibility, features that are essential for advancing the field toward robust, and physiologically accurate models to study neuronal transmission.

4.2.3 Limitations of the study

While our novel reporter line provides a robust and versatile platform for the observation of glutamate dynamics, several limitations should be considered:

First, although the Cre-dependent design allows for targeted expression of iGluSnFR3, the time required to breed animals is longer than what is required to obtain viral expression following intracortical injection. Second, the uniform and widespread expression driven by the CAG promoter may dilute spatial contrast in densely interconnected networks, complicating interpretation in areas where fine spatial resolution of glutamate dynamics is critical.

Another consideration is the biological impact of long-term iGluSnFR expression, particularly under conditions of chronic imaging or repeated stimulation. Although we did not observe cytotoxicity or altered neuronal responses in widefield or two-photon

imaging, subtle alterations in synaptic physiology or glutamate uptake cannot be fully excluded. Previous studies have suggested that glutamate sensors can alter glutamate clearance or buffering, especially at high expression levels [238]. The knock-in design of the GluTrooper mitigates this risk by driving moderate, consistent expression levels, yet future studies should directly assess synaptic function and plasticity in labeled versus unlabeled neurons to rule out undesired aberrant processes.

Furthermore, while iGluSnFR3 provides improved kinetics and signal-to-noise ratios compared to earlier generations, it still reports bulk glutamate release and does not distinguishe between vesicular and non-vesicular synaptic release [238]. Thus, while GluTrooper is well-suited for monitoring population-level or mesoscale glutamatergic activity, it is less optimal for dissecting fine-scale synaptic mechanisms or circuit motifs without complementary techniques.

Furthermore, while we demonstrated the utility of the GluTrooper in both physiological and pathophysiological conditions, our study did not explore cell-type-specific contributions to the observed dynamics. For instance, while glutamate transients are assumed to originate from pyramidal neurons in Emx1-Cre mice, astrocytic glutamate release and uptake, as well as modulatory input from thalamic or subcortical projections, may also contribute to the observed signals. Without cell-type specific markers, it remains challenging to distinguish the origin of specific glutamate events. Therefore, while the GluTrooper is a powerful tool for the observation of glutamate dynamics, it should ideally be used in conjunction with complementary techniques, such as optogenetics or chemogenetics in order to fully understand the complexity of excitatory signaling in the brain.

4.3. Future directions

This thesis focuses on the observation of interhemispheric inhibition in stroke and CSD pathophysiology via calcium and glutamate imaging.

Study I. provides a better understanding of the molecular mechanisms underlying diaschisis. However, considering the limitations we mentioned before, the combination of retrograde AAVs with Cre-dependent reporters would enable the identification of transcallosal neurons while distinguishing subpopulations and their diverse functional

role. Moreover, future studies with optogenetics and chemogenetics modulation will be needed in order to better understand the involvement of the transcallosal population in promoting chronic contralateral neuronal suppression. Furthermore, electrophysiological measurements will provide a deeper knowledge on the inhibitory remodeling observed in our calcium imaging and immunohistochemical data. Finally, expanding the cellular focus to include thalamocortical projections and different interneuron subtypes, would reveal how parallel circuits coordinate post-stroke excitability shift in the contralateral hemisphere.

Study II. centers on the development and characterization of the GluTrooper, a novel transgenic glutamate reporter line that enables longitudinal, pan-cortical expression and allows the observation of whole-brain glutamate dynamics. This model overcomes key limitations of viral delivery, offering consistent and reproducible imaging suitable for longitudinal studies. Future research will benefit from crossing the floxed GluTrooper line with cell-type-specific Cre drivers, such as those targeting astrocytes, to resolve glutamatergic signaling within distinct neural populations under both physiological and pathological conditions. Additionally, combining live glutamate imaging with structural markers will help clarify the cellular origins of observed transients. As the field continues to advance, the future introduction of iGluSnFR4 [239], which enables single-vesicle sensitivity, presents an exciting opportunity for the investigation of synaptic glutamate dynamics. Incorporating such next-generation sensors in future studies could further expand our understanding of glutamate signaling at unprecedented resolution.

5. References

1. Feigin VL, Brainin M, Norrving B, Martins SO, Pandian J, Lindsay P, M FG, Rautalin I: World Stroke Organization: Global Stroke Fact Sheet 2025. *Int J Stroke* 2025, 20(2):132-144.
2. Martins SCO, Matuja SS: Acute stroke care in low and middle-income countries. *Curr Opin Neurol* 2025, 38(1):47-53.
3. Aguirre AO, Rogers JL, Reardon T, Shlobin NA, Ballatori AM, Brown NJ, Gendreau J, Shahrestani S: Stroke management and outcomes in low-income and lower-middle-income countries: a meta-analysis of 8535 patients. *J Neurosurg* 2023, 139(4):1042-1051.
4. Kelly DM, Engelbertz C, Rothwell PM, Anderson CD, Reinecke H, Koeppe J: Age- and Sex-Specific Analysis of Stroke Hospitalization Rates, Risk Factors, and Outcomes From German Nationwide Data. *Stroke* 2024, 55(9):2284-2294.
5. Pu L, Wang L, Zhang R, Zhao T, Jiang Y, Han L: Projected Global Trends in Ischemic Stroke Incidence, Deaths and Disability-Adjusted Life Years From 2020 to 2030. *Stroke* 2023, 54(5):1330-1339.
6. Belau MH, Becher H, Riefflin M, Bartig D, Schwettmann L, Schwarzbach CJ, Grau A: The impact of regional deprivation on stroke incidence, treatment, and mortality in Germany. *Neurol Res Pract* 2023, 5(1):6.
7. Stahmeyer JT, Stubenrauch S, Geyer S, Weissenborn K, Eberhard S: The Frequency and Timing of Recurrent Stroke: An Analysis of Routine Health Insurance Data. *Dtsch Arztebl Int* 2019, 116(42):711-717.
8. Kolominsky-Rabas PL, Heuschmann PU, Marschall D, Emmert M, Baltzer N, Neundörfer B, Schöffski O, Krobot KJ: Lifetime cost of ischemic stroke in Germany: results and national projections from a population-based stroke registry: the Erlangen Stroke Project. *Stroke* 2006, 37(5):1179-1183.
9. Takahashi S: Metabolic Contribution and Cerebral Blood Flow Regulation by Astrocytes in the Neurovascular Unit. *Cells* 2022, 11(5).
10. Poli S, Mbroh J, Baron JC, Singhal AB, Strbian D, Molina C, Lemmens R, Turc G, Mikulik R, Michel P *et al*: Penumbral Rescue by normobaric O = O administration in patients with ischemic stroke and target mismatch proFile (PROOF): Study protocol of a phase IIb trial. *Int J Stroke* 2024, 19(1):120-126.
11. Skou JC: The influence of some cations on an adenosine triphosphatase from peripheral nerves. *Biochim Biophys Acta* 1957, 23(2):394-401.
12. Santos MS, Moreno AJ, Carvalho AP: Relationships between ATP depletion, membrane potential, and the release of neurotransmitters in rat nerve terminals. An in vitro study under conditions that mimic anoxia, hypoglycemia, and ischemia. *Stroke* 1996, 27(5):941-950.
13. Choi DW: Excitotoxic cell death. *J Neurobiol* 1992, 23(9):1261-1276.
14. Astrup J, Siesjö BK, Symon L: Thresholds in cerebral ischemia - the ischemic penumbra. *Stroke* 1981, 12(6):723-725.
15. Fabricius M, Fuhr S, Bhatia R, Boutelle M, Hashemi P, Strong AJ, Lauritzen M: Cortical spreading depression and peri-infarct depolarization in acutely injured human cerebral cortex. *Brain* 2006, 129(Pt 3):778-790.
16. Linnik MD, Zobrist RH, Hatfield MD: Evidence supporting a role for programmed cell death in focal cerebral ischemia in rats. *Stroke* 1993, 24(12):2002-2008; discussion 2008-2009.

17. Collyer E, Blanco-Suarez E: Astrocytes in stroke-induced neurodegeneration: a timeline. *Front Mol Med* 2023, 3:1240862.
18. Huang L, Wu ZB, Zhuge Q, Zheng W, Shao B, Wang B, Sun F, Jin K: Glial scar formation occurs in the human brain after ischemic stroke. *Int J Med Sci* 2014, 11(4):344-348.
19. Wanner IB, Anderson MA, Song B, Levine J, Fernandez A, Gray-Thompson Z, Ao Y, Sofroniew MV: Glial scar borders are formed by newly proliferated, elongated astrocytes that interact to corral inflammatory and fibrotic cells via STAT3-dependent mechanisms after spinal cord injury. *J Neurosci* 2013, 33(31):12870-12886.
20. Brodtmann A, Werden E, Khlif MS, Bird LJ, Egorova N, Veldsman M, Pardoe H, Jackson G, Bradshaw J, Darby D *et al*: Neurodegeneration Over 3 Years Following Ischaemic Stroke: Findings From the Cognition and Neocortical Volume After Stroke Study. *Front Neurol* 2021, 12:754204.
21. Kuhn MJ, Mikulis DJ, Ayoub DM, Kosofsky BE, Davis KR, Taveras JM: Wallerian degeneration after cerebral infarction: evaluation with sequential MR imaging. *Radiology* 1989, 172(1):179-182.
22. Waller A: Experiments on the Section of the Glosso-Pharyngeal and Hypoglossal Nerves of the Frog, and Observations of the Alterations Produced Thereby in the Structure of Their Primitive Fibres. *Edinb Med Surg J* 1851, 76(189):369-376.
23. Carrera E, Tononi G: Diaschisis: past, present, future. *Brain* 2014, 137(Pt 9):2408-2422.
24. Monakow Cv: Die lokalisation im grosshirn und der abbau der funktion durch kortikale herde. Wiesbaden,: J. F. Bergmann; 1914.
25. Baron JC, Bousser MG, Comar D, Castaigne P: "Crossed cerebellar diaschisis" in human supratentorial brain infarction. *Trans Am Neurol Assoc* 1981, 105:459-461.
26. Lenzi GL, Frackowiak RS, Jones T: Cerebral oxygen metabolism and blood flow in human cerebral ischemic infarction. *J Cereb Blood Flow Metab* 1982, 2(3):321-335.
27. Martin WR, Raichle ME: Cerebellar blood flow and metabolism in cerebral hemisphere infarction. *Ann Neurol* 1983, 14(2):168-176.
28. Förster A, Kerl HU, Goerlitz J, Wenz H, Groden C: Crossed cerebellar diaschisis in acute isolated thalamic infarction detected by dynamic susceptibility contrast perfusion MRI. *PLoS One* 2014, 9(2):e88044.
29. Xia C, Zhou J, Lu C, Wang Y, Tang T, Cai Y, Ju S: Characterizing Diaschisis-Related Thalamic Perfusion and Diffusion After Middle Cerebral Artery Infarction. *Stroke* 2021, 52(7):2319-2327.
30. Reidler P, Thierfelder KM, Fabritius MP, Sommer WH, Meinel FG, Dorn F, Wollenweber FA, Duering M, Kunz WG: Thalamic Diaschisis in Acute Ischemic Stroke: Occurrence, Perfusion Characteristics, and Impact on Outcome. *Stroke* 2018, 49(4):931-937.
31. Seitz RJ, Azari NP, Knorr U, Binkofski F, Herzog H, Freund HJ: The role of diaschisis in stroke recovery. *Stroke* 1999, 30(9):1844-1850.
32. Wawrzyniak M, Schneider HR, Klingbeil J, Stockert A, Hartwigsen G, Weiller C, Saur D: Resolution of diaschisis contributes to early recovery from post-stroke aphasia. *Neuroimage* 2022, 251:119001.

33. Thomalla G, Glauche V, Koch MA, Beaulieu C, Weiller C, Röther J: Diffusion tensor imaging detects early Wallerian degeneration of the pyramidal tract after ischemic stroke. *Neuroimage* 2004, 22(4):1767-1774.
34. Egorova N, Dhollander T, Khlif MS, Khan W, Werden E, Brodtmann A: Pervasive White Matter Fiber Degeneration in Ischemic Stroke. *Stroke* 2020, 51(5):1507-1513.
35. Kinnunen KM, Greenwood R, Powell JH, Leech R, Hawkins PC, Bonnelle V, Patel MC, Counsell SJ, Sharp DJ: White matter damage and cognitive impairment after traumatic brain injury. *Brain* 2011, 134(Pt 2):449-463.
36. Villegas R, Martinez NW, Lillo J, Pihan P, Hernandez D, Twiss JL, Court FA: Calcium release from intra-axonal endoplasmic reticulum leads to axon degeneration through mitochondrial dysfunction. *J Neurosci* 2014, 34(21):7179-7189.
37. Puig J, Blasco G, Schlaug G, Stinear CM, Daunis IEP, Biarnes C, Figueras J, Serena J, Hernández-Pérez M, Alberich-Bayarri A *et al*: Diffusion tensor imaging as a prognostic biomarker for motor recovery and rehabilitation after stroke. *Neuroradiology* 2017, 59(4):343-351.
38. Schaechter JD, Fricker ZP, Perdue KL, Helmer KG, Vangel MG, Greve DN, Makris N: Microstructural status of ipsilesional and contralesional corticospinal tract correlates with motor skill in chronic stroke patients. *Hum Brain Mapp* 2009, 30(11):3461-3474.
39. Siegel JS, Ramsey LE, Snyder AZ, Metcalf NV, Chacko RV, Weinberger K, Baldassarre A, Hacker CD, Shulman GL, Corbetta M: Disruptions of network connectivity predict impairment in multiple behavioral domains after stroke. *Proc Natl Acad Sci U S A* 2016, 113(30):E4367-4376.
40. Yourganov G, Stark BC, Fridriksson J, Bonilha L, Rorden C: Effect of Stroke on Contralateral Functional Connectivity. *Brain Connect* 2021, 11(7):543-552.
41. Cheng B, Dietzmann P, Schulz R, Boenstrup M, Krawinkel L, Fiehler J, Gerloff C, Thomalla G: Cortical atrophy and transcallosal diaschisis following isolated subcortical stroke. *J Cereb Blood Flow Metab* 2020, 40(3):611-621.
42. Cheng HJ, Ng KK, Qian X, Ji F, Lu ZK, Teo WP, Hong X, Nasrallah FA, Ang KK, Chuang KH *et al*: Task-related brain functional network reconfigurations relate to motor recovery in chronic subcortical stroke. *Sci Rep* 2021, 11(1):8442.
43. Li Y, Yu Z, Wu P, Chen J: Ability of an altered functional coupling between resting-state networks to predict behavioral outcomes in subcortical ischemic stroke: A longitudinal study. *Front Aging Neurosci* 2022, 14:933567.
44. Webster BR, Celnik PA, Cohen LG: Noninvasive brain stimulation in stroke rehabilitation. *NeuroRx* 2006, 3(4):474-481.
45. Khedr EM, Ahmed MA, Fathy N, Rothwell JC: Therapeutic trial of repetitive transcranial magnetic stimulation after acute ischemic stroke. *Neurology* 2005, 65(3):466-468.
46. Fregni F, Boggio PS, Valle AC, Rocha RR, Duarte J, Ferreira MJ, Wagner T, Fecteau S, Rigonatti SP, Riberto M *et al*: A sham-controlled trial of a 5-day course of repetitive transcranial magnetic stimulation of the unaffected hemisphere in stroke patients. *Stroke* 2006, 37(8):2115-2122.
47. Harris-Love ML, Cohen LG: Noninvasive cortical stimulation in neurorehabilitation: a review. *Arch Phys Med Rehabil* 2006, 87(12 Suppl 2):S84-93.

48. Huang YZ, Edwards MJ, Rounis E, Bhatia KP, Rothwell JC: Theta burst stimulation of the human motor cortex. *Neuron* 2005, 45(2):201-206.
49. Berthier ML, Green C, Higueras C, Fernández I, Hinojosa J, Martín MC: A randomized, placebo-controlled study of donepezil in poststroke aphasia. *Neurology* 2006, 67(9):1687-1689.
50. Cramer SC: Repairing the human brain after stroke: I. Mechanisms of spontaneous recovery. *Ann Neurol* 2008, 63(3):272-287.
51. Cramer SC: An overview of therapies to promote repair of the brain after stroke. *Head Neck* 2011, 33 Suppl 1:S5-7.
52. Taub E, Uswatte G, Pidikiti R: Constraint-Induced Movement Therapy: a new family of techniques with broad application to physical rehabilitation--a clinical review. *J Rehabil Res Dev* 1999, 36(3):237-251.
53. Miltner WH, Bauder H, Sommer M, Dettmers C, Taub E: Effects of constraint-induced movement therapy on patients with chronic motor deficits after stroke: a replication. *Stroke* 1999, 30(3):586-592.
54. Kleim JA, Lussnig E, Schwarz ER, Comery TA, Greenough WT: Synaptogenesis and Fos expression in the motor cortex of the adult rat after motor skill learning. *J Neurosci* 1996, 16(14):4529-4535.
55. Kleim JA, Pipitone MA, Czerlanis C, Greenough WT: Structural stability within the lateral cerebellar nucleus of the rat following complex motor learning. *Neurobiol Learn Mem* 1998, 69(3):290-306.
56. Kleim JA, Barbay S, Cooper NR, Hogg TM, Reidel CN, Remple MS, Nudo RJ: Motor learning-dependent synaptogenesis is localized to functionally reorganized motor cortex. *Neurobiol Learn Mem* 2002, 77(1):63-77.
57. Crosson B, Moore AB, Gopinath K, White KD, Wierenga CE, Gaiefsky ME, Fabrizio KS, Peck KK, Soltysik D, Milsted C *et al*: Role of the right and left hemispheres in recovery of function during treatment of intention in aphasia. *J Cogn Neurosci* 2005, 17(3):392-406.
58. Humm JL, Kozlowski DA, James DC, Gotts JE, Schallert T: Use-dependent exacerbation of brain damage occurs during an early post-lesion vulnerable period. *Brain Res* 1998, 783(2):286-292.
59. Biernaskie J, Chernenko G, Corbett D: Efficacy of rehabilitative experience declines with time after focal ischemic brain injury. *J Neurosci* 2004, 24(5):1245-1254.
60. Cumming TB, Thrift AG, Collier JM, Churilov L, Dewey HM, Donnan GA, Bernhardt J: Very early mobilization after stroke fast-tracks return to walking: further results from the phase II AVERT randomized controlled trial. *Stroke* 2011, 42(1):153-158.
61. Indredavik B, Bakke F, Slordahl SA, Rokseth R, Hâheim LL: Treatment in a combined acute and rehabilitation stroke unit: which aspects are most important? *Stroke* 1999, 30(5):917-923.
62. Maulden SA, Gassaway J, Horn SD, Smout RJ, DeJong G: Timing of initiation of rehabilitation after stroke. *Arch Phys Med Rehabil* 2005, 86(12 Suppl 2):S34-s40.
63. Musicco M, Emberti L, Nappi G, Caltagirone C: Early and long-term outcome of rehabilitation in stroke patients: the role of patient characteristics, time of initiation, and duration of interventions. *Arch Phys Med Rehabil* 2003, 84(4):551-558.

64. Leao AAP: SPREADING DEPRESSION OF ACTIVITY IN THE CEREBRAL CORTEX. *Journal of Neurophysiology* 1944, 7(6):359-390.
65. Leao AA: Further observations on the spreading depression of activity in the cerebral cortex. *J Neurophysiol* 1947, 10(6):409-414.
66. Basarsky TA, Duffy SN, Andrew RD, MacVicar BA: Imaging spreading depression and associated intracellular calcium waves in brain slices. *J Neurosci* 1998, 18(18):7189-7199.
67. Martins-Ferreira H, Nedergaard M, Nicholson C: Perspectives on spreading depression. *Brain Res Brain Res Rev* 2000, 32(1):215-234.
68. Dani JW, Chernjavsky A, Smith SJ: Neuronal activity triggers calcium waves in hippocampal astrocyte networks. *Neuron* 1992, 8(3):429-440.
69. Canals S, Makarova I, López-Aguado L, Largo C, Ibarz JM, Herreras O: Longitudinal depolarization gradients along the somatodendritic axis of CA1 pyramidal cells: a novel feature of spreading depression. *J Neurophysiol* 2005, 94(2):943-951.
70. Kraig RP, Nicholson C: Extracellular ionic variations during spreading depression. *Neuroscience* 1978, 3(11):1045-1059.
71. Fabricius M, Lauritzen M: Examination of the role of nitric oxide for the hypercapnic rise of cerebral blood flow in rats. *Am J Physiol* 1994, 266(4 Pt 2):H1457-1464.
72. Kager H, Wadman WJ, Somjen GG: Conditions for the triggering of spreading depression studied with computer simulations. *J Neurophysiol* 2002, 88(5):2700-2712.
73. Eikermann-Haerter K, Lee JH, Yuzawa I, Liu CH, Zhou Z, Shin HK, Zheng Y, Qin T, Kurth T, Waeber C *et al*: Migraine mutations increase stroke vulnerability by facilitating ischemic depolarizations. *Circulation* 2012, 125(2):335-345.
74. Dreier JP: The role of spreading depression, spreading depolarization and spreading ischemia in neurological disease. *Nat Med* 2011, 17(4):439-447.
75. Fischer P, Tamim I, Sugimoto K, Morais A, Imai T, Takizawa T, Qin T, Schlunk F, Endres M, Yaseen MA *et al*: Spreading Depolarizations Suppress Hematoma Growth in Hyperacute Intracerebral Hemorrhage in Mice. *Stroke* 2023, 54(10):2640-2651.
76. Grafstein B: Mechanism of spreading cortical depression. *J Neurophysiol* 1956, 19(2):154-171.
77. Leis JA, Bekar LK, Walz W: Potassium homeostasis in the ischemic brain. *Glia* 2005, 50(4):407-416.
78. Nozari A, Dilekoz E, Sukhotinsky I, Stein T, Eikermann-Haerter K, Liu C, Wang Y, Frosch MP, Waeber C, Ayata C *et al*: Microemboli may link spreading depression, migraine aura, and patent foramen ovale. *Ann Neurol* 2010, 67(2):221-229.
79. Enger R, Tang W, Vindedal GF, Jensen V, Johannes Helm P, Sprengel R, Looger LL, Nagelhus EA: Dynamics of Ionic Shifts in Cortical Spreading Depression. *Cereb Cortex* 2015, 25(11):4469-4476.
80. Maneepark M, Srikiatkhachorn A, Bongsebandhu-phubhakdi S: Involvement of AMPA receptors in CSD-induced impairment of LTP in the hippocampus. *Headache* 2012, 52(10):1535-1545.
81. Shatillo A, Salo RA, Giniatullin R, Gröhn OH: Involvement of NMDA receptor subtypes in cortical spreading depression in rats assessed by fMRI. *Neuropharmacology* 2015, 93:164-170.

82. Hansen AJ, Zeuthen T: Extracellular ion concentrations during spreading depression and ischemia in the rat brain cortex. *Acta Physiol Scand* 1981, 113(4):437-445.
83. Heinemann U, Lux HD: Ceiling of stimulus induced rises in extracellular potassium concentration in the cerebral cortex of cat. *Brain Res* 1977, 120(2):231-249.
84. Lothman E, Lamanna J, Cordingley G, Rosenthal M, Somjen G: Responses of electrical potential, potassium levels, and oxidative metabolic activity of the cerebral neocortex of cats. *Brain Res* 1975, 88(1):15-36.
85. Matsuura T, Bures J: The minimum volume of depolarized neural tissue required for triggering cortical spreading depression in rat. *Exp Brain Res* 1971, 12(3):238-249.
86. Brinley FJ, Jr., Kandel ER, Marshall WH: Potassium outflux from rabbit cortex during spreading depression. *J Neurophysiol* 1960, 23:246-256.
87. Hansen AJ, Quistorff B, Gjedde A: Relationship between local changes in cortical blood flow and extracellular K+ during spreading depression. *Acta Physiol Scand* 1980, 109(1):1-6.
88. Nicholson C, ten Bruggencate G, Stöckle H, Steinberg R: Calcium and potassium changes in extracellular microenvironment of cat cerebellar cortex. *J Neurophysiol* 1978, 41(4):1026-1039.
89. Vyskocil F, Kritz N, Bures J: Potassium-selective microelectrodes used for measuring the extracellular brain potassium during spreading depression and anoxic depolarization in rats. *Brain Res* 1972, 39(1):255-259.
90. Nicholson C, Bruggencate GT, Steinberg R, Stöckle H: Calcium modulation in brain extracellular microenvironment demonstrated with ion-selective micropipette. *Proc Natl Acad Sci U S A* 1977, 74(3):1287-1290.
91. Gidö G, Katsura K, Kristian T, Siesjö BK: Influence of plasma glucose concentration on rat brain extracellular calcium transients during spreading depression. *J Cereb Blood Flow Metab* 1993, 13(1):179-182.
92. Dreier JP, Fabricius M, Ayata C, Sakowitz OW, Shuttleworth CW, Dohmen C, Graf R, Vajkoczy P, Helbok R, Suzuki M *et al*: Recording, analysis, and interpretation of spreading depolarizations in neurointensive care: Review and recommendations of the COSBID research group. *J Cereb Blood Flow Metab* 2017, 37(5):1595-1625.
93. Frostig RD, Chen-Bee CH: Frontiers in Neuroscience

Visualizing Adult Cortical Plasticity Using Intrinsic Signal Optical Imaging. In: *In Vivo Optical Imaging of Brain Function.* Edited by Frostig RD. Boca Raton (FL): CRC Press/Taylor & Francis

94. Masino SA, Kwon MC, Dory Y, Frostig RD: Characterization of functional organization within rat barrel cortex using intrinsic signal optical imaging through a thinned skull. *Proc Natl Acad Sci U S A* 1993, 90(21):9998-10002.
95. Prakash N, Cohen-Cory S, Frostig RD: RAPID and opposite effects of BDNF and NGF on the functional organization of the adult cortex in vivo. *Nature* 1996, 381(6584):702-706.
96. Polley DB, Chen-Bee CH, Frostig RD: Two directions of plasticity in the sensory-deprived adult cortex. *Neuron* 1999, 24(3):623-637.

97. Chen JW, O'Farrell AM, Toga AW: Optical intrinsic signal imaging in a rodent seizure model. *Neurology* 2000, 55(2):312-315.
98. Ba AM, Guiou M, Pouratian N, Muthialu A, Rex DE, Cannestra AF, Chen JW, Toga AW: Multiwavelength optical intrinsic signal imaging of cortical spreading depression. *J Neurophysiol* 2002, 88(5):2726-2735.
99. Clarkson AN, López-Valdés HE, Overman JJ, Charles AC, Brennan KC, Thomas Carmichael S: Multimodal examination of structural and functional remapping in the mouse photothrombotic stroke model. *J Cereb Blood Flow Metab* 2013, 33(5):716-723.
100. Johnston DG, Denizet M, Mostany R, Portera-Cailliau C: Chronic in vivo imaging shows no evidence of dendritic plasticity or functional remapping in the contralesional cortex after stroke. *Cereb Cortex* 2013, 23(4):751-762.
101. He Q, Arroyo ED, Smukowski SN, Xu J, Piochon C, Savas JN, Portera-Cailliau C, Contractor A: Critical period inhibition of NKCC1 rectifies synapse plasticity in the somatosensory cortex and restores adult tactile response maps in fragile X mice. *Mol Psychiatry* 2019, 24(11):1732-1747.
102. Fox PT, Raichle ME: Focal physiological uncoupling of cerebral blood flow and oxidative metabolism during somatosensory stimulation in human subjects. *Proc Natl Acad Sci U S A* 1986, 83(4):1140-1144.
103. Malonek D, Dirnagl U, Lindauer U, Yamada K, Kanno I, Grinvald A: Vascular imprints of neuronal activity: relationships between the dynamics of cortical blood flow, oxygenation, and volume changes following sensory stimulation. *Proc Natl Acad Sci U S A* 1997, 94(26):14826-14831.
104. Akgören N, Fabricius M, Lauritzen M: Importance of nitric oxide for local increases of blood flow in rat cerebellar cortex during electrical stimulation. *Proc Natl Acad Sci U S A* 1994, 91(13):5903-5907.
105. Li J, Iadecola C: Nitric oxide and adenosine mediate vasodilation during functional activation in cerebellar cortex. *Neuropharmacology* 1994, 33(11):1453-1461.
106. Takano T, Tian GF, Peng W, Lou N, Libionka W, Han X, Nedergaard M: Astrocyte-mediated control of cerebral blood flow. *Nat Neurosci* 2006, 9(2):260-267.
107. Dana H, Chen TW, Hu A, Shields BC, Guo C, Looger LL, Kim DS, Svoboda K: Thy1-GCaMP6 transgenic mice for neuronal population imaging in vivo. *PLoS One* 2014, 9(9):e108697.
108. Zhao HT, Tuohy MC, Chow D, Kozberg MG, Kim SH, Shaik MA, Hillman EMC: Neurovascular dynamics of repeated cortical spreading depolarizations after acute brain injury. *Cell Rep* 2021, 37(1):109794.
109. Marvin JS, Shimoda Y, Magloire V, Leite M, Kawashima T, Jensen TP, Kolb I, Knott EL, Novak O, Podgorski K *et al*: A genetically encoded fluorescent sensor for in vivo imaging of GABA. *Nat Methods* 2019, 16(8):763-770.
110. Marvin JS, Borghuis BG, Tian L, Cichon J, Harnett MT, Akerboom J, Gordus A, Renninger SL, Chen TW, Bargmann CI *et al*: An optimized fluorescent probe for visualizing glutamate neurotransmission. *Nat Methods* 2013, 10(2):162-170.
111. Feng J, Dong H, Lischinsky JE, Zhou J, Deng F, Zhuang C, Miao X, Wang H, Li G, Cai R *et al*: Monitoring norepinephrine release in vivo using next-generation GRAB(NE) sensors. *Neuron* 2024, 112(12):1930-1942.e1936.

112. Gulbinaite R, Nazari M, Rule ME, Bermudez-Contreras EJ, Cohen MX, Mohajerani MH, Heimel JA: Spatiotemporal resonance in mouse primary visual cortex. *Curr Biol* 2024, 34(18):4184-4196.e4187.
113. Ziebarth T, Pape N, Nelson JSE, van Alphen FIM, Kalia M, Meijer HGE, Rose CR, Reiner A: Atypical plume-like events contribute to glutamate accumulation in metabolic stress conditions. *iScience* 2025, 28(4):112256.
114. Garcia JP, Armbruster M, Sommer M, Nunez-Beringer A, Dulla CG: Glutamate uptake is transiently compromised in the perilesional cortex following controlled cortical impact. *Cereb Cortex* 2025, 35(2).
115. Shepard GM: The legacy of Camillo Golgi for modern concepts of brain organization. *J Hist Neurosci* 1999, 8(2):209-214.
116. García-López P, García-Marín V, Freire M: The discovery of dendritic spines by Cajal in 1888 and its relevance in the present neuroscience. *Prog Neurobiol* 2007, 83(2):110-130.
117. DeFelipe J: The dendritic spine story: an intriguing process of discovery. *Front Neuroanat* 2015, 9:14.
118. Yuste R: From the neuron doctrine to neural networks. *Nat Rev Neurosci* 2015, 16(8):487-497.
119. Hodge RD, Bakken TE, Miller JA, Smith KA, Barkan ER, Graybuck LT, Close JL, Long B, Johansen N, Penn O *et al*: Conserved cell types with divergent features in human versus mouse cortex. *Nature* 2019, 573(7772):61-68.
120. Kandel ER, Koester JD, Mack SH, Siegelbaum SA. In: *Principles of Neural Science, 6e.* New York, NY: McGraw Hill; 2021.
121. Süudhof TC: Neurotransmitter release. *Handb Exp Pharmacol* 2008(184):1-21.
122. Panzeri S, Petersen RS, Schultz SR, Lebedev M, Diamond ME: The role of spike timing in the coding of stimulus location in rat somatosensory cortex. *Neuron* 2001, 29(3):769-777.
123. Laughlin SB, Sejnowski TJ: Communication in neuronal networks. *Science* 2003, 301(5641):1870-1874.
124. Harris JJ, Jolivet R, Attwell D: Synaptic energy use and supply. *Neuron* 2012, 75(5):762-777.
125. Furshpan EJ, Potter DD: Mechanism of nerve-impulse transmission at a crayfish synapse. *Nature* 1957, 180(4581):342-343.
126. Spray DC, Harris AL, Bennett MV: Voltage dependence of junctional conductance in early amphibian embryos. *Science* 1979, 204(4391):432-434.
127. Spray DC, Harris AL, Bennett MV: Gap junctional conductance is a simple and sensitive function of intracellular pH. *Science* 1981, 211(4483):712-715.
128. Loewi O: Über humorale übertragbarkeit der Herznervenwirkung. *Pflüger's Archiv für die gesamte Physiologie des Menschen und der Tiere* 1921, 189(1):239-242.
129. DeFelipe J, Marco P, Busturia I, Merchán-Pérez A: Estimation of the number of synapses in the cerebral cortex: methodological considerations. *Cereb Cortex* 1999, 9(7):722-732.
130. Roberts E, Frankel S: gamma-Aminobutyric acid in brain: its formation from glutamic acid. *J Biol Chem* 1950, 187(1):55-63.
131. Krnjević K, Schwartz S: The action of gamma-aminobutyric acid on cortical neurones. *Exp Brain Res* 1967, 3(4):320-336.

132. Curtis DR, Hösli L, Johnston GA: A pharmacological study of the depression of spinal neurones by glycine and related amino acids. *Exp Brain Res* 1968, 6(1):1-18.
133. Curtis DR, Watkins JC: Analogues of glutamic and gamma-amino-n-butyric acids having potent actions on mammalian neurones. *Nature* 1961, 191:1010-1011.
134. Curtis DR, Watkins JC: Acidic amino acids with strong excitatory actions on mammalian neurones. *J Physiol* 1963, 166(1):1-14.
135. Dingledine R, Borges K, Bowie D, Traynelis SF: The glutamate receptor ion channels. *Pharmacol Rev* 1999, 51(1):7-61.
136. Mayer ML, Westbrook GL, Guthrie PB: Voltage-dependent block by Mg2+ of NMDA responses in spinal cord neurones. *Nature* 1984, 309(5965):261-263.
137. Nowak L, Bregestovski P, Ascher P, Herbet A, Prochiantz A: Magnesium gates glutamate-activated channels in mouse central neurones. *Nature* 1984, 307(5950):462-465.
138. Olsen RW, Tobin AJ: Molecular biology of GABAA receptors. *Faseb j* 1990, 4(5):1469-1480.
139. Hill DR, Bowery NG: 3H-baclofen and 3H-GABA bind to bicuculline-insensitive GABA B sites in rat brain. *Nature* 1981, 290(5802):149-152.
140. Bowery NG, Hill DR, Hudson AL: Characteristics of GABAB receptor binding sites on rat whole brain synaptic membranes. *Br J Pharmacol* 1983, 78(1):191-206.
141. Dutar P, Nicoll RA: A physiological role for GABAB receptors in the central nervous system. *Nature* 1988, 332(6160):156-158.
142. Lynch JW: Native glycine receptor subtypes and their physiological roles. *Neuropharmacology* 2009, 56(1):303-309.
143. Neher E, Sakaba T: Multiple roles of calcium ions in the regulation of neurotransmitter release. *Neuron* 2008, 59(6):861-872.
144. Grienberger C, Konnerth A: Imaging calcium in neurons. *Neuron* 2012, 73(5):862-885.
145. Dana H, Sun Y, Mohar B, Hulse BK, Kerlin AM, Hasseman JP, Tsegaye G, Tsang A, Wong A, Patel R *et al*: High-performance calcium sensors for imaging activity in neuronal populations and microcompartments. *Nat Methods* 2019, 16(7):649-657.
146. Catterall WA: Voltage-gated calcium channels. *Cold Spring Harb Perspect Biol* 2011, 3(8):a003947.
147. Catterall WA, Few AP: Calcium channel regulation and presynaptic plasticity. *Neuron* 2008, 59(6):882-901.
148. Südhof TC: Neurotransmitter release: the last millisecond in the life of a synaptic vesicle. *Neuron* 2013, 80(3):675-690.
149. Rizzuto R, Pozzan T: Microdomains of intracellular Ca2+: molecular determinants and functional consequences. *Physiol Rev* 2006, 86(1):369-408.
150. Berridge MJ: Neuronal calcium signaling. *Neuron* 1998, 21(1):13-26.
151. Kano M, Garaschuk O, Verkhratsky A, Konnerth A: Ryanodine receptor-mediated intracellular calcium release in rat cerebellar Purkinje neurones. *J Physiol* 1995, 487(1):1-16.
152. Zaidi M, Shankar VS, Towhidul Alam AS, Moonga BS, Pazianas M, Huang CL: Evidence that a ryanodine receptor triggers signal transduction in the osteoclast. *Biochem Biophys Res Commun* 1992, 188(3):1332-1336.

153. Schwab Y, Mouton J, Chasserot-Golaz S, Marty I, Maulet Y, Jover E: Calcium-dependent translocation of synaptotagmin to the plasma membrane in the dendrites of developing neurones. *Brain Res Mol Brain Res* 2001, 96(1-2):1-13.
154. Kennedy MB: Regulation of neuronal function by calcium. *Trends Neurosci* 1989, 12(11):417-420.
155. Gallin WJ, Greenberg ME: Calcium regulation of gene expression in neurons: the mode of entry matters. *Curr Opin Neurobiol* 1995, 5(3):367-374.
156. Yuste R, Denk W: Dendritic spines as basic functional units of neuronal integration. *Nature* 1995, 375(6533):682-684.
157. Mainen ZF, Malinow R, Svoboda K: Synaptic calcium transients in single spines indicate that NMDA receptors are not saturated. *Nature* 1999, 399(6732):151-155.
158. Lynch G, Larson J, Kelso S, Barrionuevo G, Schottler F: Intracellular injections of EGTA block induction of hippocampal long-term potentiation. *Nature* 1983, 305(5936):719-721.
159. Malenka RC, Lancaster B, Zucker RS: Temporal limits on the rise in postsynaptic calcium required for the induction of long-term potentiation. *Neuron* 1992, 9(1):121-128.
160. Lisman J: A mechanism for the Hebb and the anti-Hebb processes underlying learning and memory. *Proc Natl Acad Sci U S A* 1989, 86(23):9574-9578.
161. Cummings JA, Mulkey RM, Nicoll RA, Malenka RC: Ca2+ signaling requirements for long-term depression in the hippocampus. *Neuron* 1996, 16(4):825-833.
162. Malinow R, Malenka RC: AMPA receptor trafficking and synaptic plasticity. *Annu Rev Neurosci* 2002, 25:103-126.
163. Engert F, Bonhoeffer T: Dendritic spine changes associated with hippocampal long-term synaptic plasticity. *Nature* 1999, 399(6731):66-70.
164. Riedel G, Platt B, Micheau J: Glutamate receptor function in learning and memory. *Behav Brain Res* 2003, 140(1-2):1-47.
165. Hodgkin AL, Huxley AF: Action potentials recorded from inside a nerve fibre. *Nature* 1939, 144(3651):710-711.
166. Neher E, Sakmann B: Single-channel currents recorded from membrane of denervated frog muscle fibres. *Nature* 1976, 260(5554):799-802.
167. Frerking M, Borges S, Wilson M: Variation in GABA mini amplitude is the consequence of variation in transmitter concentration. *Neuron* 1995, 15(4):885-895.
168. Carvelli L, McDonald PW, Blakely RD, DeFelice LJ: Dopamine transporters depolarize neurons by a channel mechanism. *Proc Natl Acad Sci U S A* 2004, 101(45):16046-16051.
169. Hartveit E: Membrane currents evoked by ionotropic glutamate receptor agonists in rod bipolar cells in the rat retinal slice preparation. *J Neurophysiol* 1996, 76(1):401-422.
170. Chieng B, Azriel Y, Mohammadi S, Christie MJ: Distinct cellular properties of identified dopaminergic and GABAergic neurons in the mouse ventral tegmental area. *J Physiol* 2011, 589(Pt 15):3775-3787.
171. Planert H, Berger TK, Silberberg G: Membrane properties of striatal direct and indirect pathway neurons in mouse and rat slices and their modulation by dopamine. *PLoS One* 2013, 8(3):e57054.

172. Du J, Reznikov LR, Price MP, Zha XM, Lu Y, Moninger TO, Wemmie JA, Welsh MJ: Protons are a neurotransmitter that regulates synaptic plasticity in the lateral amygdala. *Proc Natl Acad Sci U S A* 2014, 111(24):8961-8966.
173. Royer S, Paré D: Bidirectional synaptic plasticity in intercalated amygdala neurons and the extinction of conditioned fear responses. *Neuroscience* 2002, 115(2):455-462.
174. Denk W, Strickler JH, Webb WW: Two-photon laser scanning fluorescence microscopy. *Science* 1990, 248(4951):73-76.
175. Tsien RY: New calcium indicators and buffers with high selectivity against magnesium and protons: design, synthesis, and properties of prototype structures. *Biochemistry* 1980, 19(11):2396-2404.
176. Nakai J, Ohkura M, Imoto K: A high signal-to-noise Ca(2+) probe composed of a single green fluorescent protein. *Nat Biotechnol* 2001, 19(2):137-141.
177. Göppert-Mayer M: Über Elementarakte mit zwei Quantensprüngen. *Annalen der Physik* 1931, 401(3):273-294.
178. Kaiser W, Garrett CGB: Two-Photon Excitation in Ca${\mathrm{F}}_{2}$: ${\mathrm{Eu}}^{2+}$. *Physical Review Letters* 1961, 7(6):229-231.
179. Gosnell TR, Taylor AJ: Selected Papers on Ultrafast Laser Technology: SPIE Optical Engineering Press; 1991.
180. Svoboda K, Yasuda R: Principles of two-photon excitation microscopy and its applications to neuroscience. *Neuron* 2006, 50(6):823-839.
181. Guild JB, Xu C, Webb WW: Measurement of group delay dispersion of high numerical aperture objective lenses using two-photon excited fluorescence. *Appl Opt* 1997, 36(1):397-401.
182. Lichtman JW, Conchello JA: Fluorescence microscopy. *Nat Methods* 2005, 2(12):910-919.
183. Helmchen F, Denk W: Deep tissue two-photon microscopy. *Nat Methods* 2005, 2(12):932-940.
184. Marvin JS, Scholl B, Wilson DE, Podgorski K, Kazemipour A, Müller JA, Schoch S, Quiroz FJU, Rebola N, Bao H *et al*: Stability, affinity, and chromatic variants of the glutamate sensor iGluSnFR. *Nat Methods* 2018, 15(11):936-939.
185. Akerboom J, Rivera JD, Guilbe MM, Malavé EC, Hernandez HH, Tian L, Hires SA, Marvin JS, Looger LL, Schreiter ER: Crystal structures of the GCaMP calcium sensor reveal the mechanism of fluorescence signal change and aid rational design. *J Biol Chem* 2009, 284(10):6455-6464.
186. Chen TW, Wardill TJ, Sun Y, Pulver SR, Renninger SL, Baohan A, Schreiter ER, Kerr RA, Orger MB, Jayaraman V *et al*: Ultrasensitive fluorescent proteins for imaging neuronal activity. *Nature* 2013, 499(7458):295-300.
187. Steinmetz NA, Buetfering C, Lecoq J, Lee CR, Peters AJ, Jacobs EAK, Coen P, Ollerenshaw DR, Valley MT, de Vries SEJ *et al*: Aberrant Cortical Activity in Multiple GCaMP6-Expressing Transgenic Mouse Lines. *eNeuro* 2017, 4(5).
188. Traynelis SF, Wollmuth LP, McBain CJ, Menniti FS, Vance KM, Ogden KK, Hansen KB, Yuan H, Myers SJ, Dingledine R: Glutamate receptor ion channels: structure, regulation, and function. *Pharmacol Rev* 2010, 62(3):405-496.
189. Paoletti P, Bellone C, Zhou Q: NMDA receptor subunit diversity: impact on receptor properties, synaptic plasticity and disease. *Nat Rev Neurosci* 2013, 14(6):383-400.

190. Bito L, Davson H, Levin E, Murray M, Snider N: The concentrations of free amino acids and other electrolytes in cerebrospinal fluid, in vivo dialysate of brain, and blood plasma of the dog. *J Neurochem* 1966, 13(11):1057-1067.
191. Delgado JM, DeFeudis FV, Roth RH, Ryugo DK, Mitruka BM: Dialytrode for long term intracerebral perfusion in awake monkeys. *Arch Int Pharmacodyn Ther* 1972, 198(1):9-21.
192. Dietze S, Kuschinsky K: Determination of extracellular glutamate after local K+ stimulation in the striatum of non-anaesthetised rats after treatment with dopaminergic drugs--studies using microdialysis. *J Neural Transm Gen Sect* 1992, 90(1):1-11.
193. Bourdelais AJ, Kalivas PW: Modulation of extracellular gamma-aminobutyric acid in the ventral pallidum using in vivo microdialysis. *J Neurochem* 1992, 58(6):2311-2320.
194. Imperato A, Di Chiara G: Trans-striatal dialysis coupled to reverse phase high performance liquid chromatography with electrochemical detection: a new method for the study of the in vivo release of endogenous dopamine and metabolites. *J Neurosci* 1984, 4(4):966-977.
195. Ungerstedt U, Pycock C: Functional correlates of dopamine neurotransmission. *Bull Schweiz Akad Med Wiss* 1974, 30(1-3):44-55.
196. Desrayaud S, Boschi G, Rips R, Scherrmann JM: Dose-dependent delivery of colchicine to the rat hippocampus by microdialysis. *Neurosci Lett* 1996, 205(1):9-12.
197. Waga J: Ganciclovir delivery through an intravitreal microdialysis probe in rabbit. *Acta Ophthalmol Scand* 2000, 78(3):369-371.
198. Qu Y, Van der Gucht E, Massie A, Vandenbussche E, Vandesande F, Arckens L: In vivo microdialysis in the visual cortex of awake cat. III: histological verification. *Brain Res Brain Res Protoc* 2001, 7(1):52-60.
199. Georgieva J, Luthman J, Mohringe B, Magnusson O: Tissue and microdialysate changes after repeated and permanent probe implantation in the striatum of freely moving rats. *Brain Res Bull* 1993, 31(5):463-470.
200. Huff JK, Bresnahan JF, Davies MI: Preliminary evaluation of several disinfection/sterilization techniques for use with microdialysis probes. *Life Sci* 2003, 73(3):275-287.
201. Westergren I, Nyström B, Hamberger A, Johansson BB: Intracerebral dialysis and the blood-brain barrier. *J Neurochem* 1995, 64(1):229-234.
202. Groothuis DR, Ward S, Schlageter KE, Itskovich AC, Schwerin SC, Allen CV, Dills C, Levy RM: Changes in blood-brain barrier permeability associated with insertion of brain cannulas and microdialysis probes. *Brain Res* 1998, 803(1-2):218-230.
203. Timmerman W, Westerink BH: Brain microdialysis of GABA and glutamate: what does it signify? *Synapse* 1997, 27(3):242-261.
204. Lada MW, Vickroy TW, Kennedy RT: Evidence for neuronal origin and metabotropic receptor-mediated regulation of extracellular glutamate and aspartate in rat striatum in vivo following electrical stimulation of the prefrontal cortex. *J Neurochem* 1998, 70(2):617-625.
205. Shiraishi M, Kamiyama Y, Hüttemeier PC, Benveniste H: Extracellular glutamate and dopamine measured by microdialysis in the rat striatum during blockade of synaptic transmission in anesthetized and awake rats. *Brain Res* 1997, 759(2):221-227.

206. Hu Y, Mitchell KM, Albahadily FN, Michaelis EK, Wilson GS: Direct measurement of glutamate release in the brain using a dual enzyme-based electrochemical sensor. *Brain Res* 1994, 659(1-2):117-125.
207. Kulagina NV, Shankar L, Michael AC: Monitoring glutamate and ascorbate in the extracellular space of brain tissue with electrochemical microsensors. *Anal Chem* 1999, 71(22):5093-5100.
208. Oldenziel WH, Beukema W, Westerink BH: Improving the reproducibility of hydrogel-coated glutamate microsensors by using an automated dipcoater. *J Neurosci Methods* 2004, 140(1-2):117-126.
209. Qin S, Van der Zeyden M, Oldenziel WH, Cremers TI, Westerink BH: Microsensors for in vivo Measurement of Glutamate in Brain Tissue. *Sensors (Basel)* 2008, 8(11):6860-6884.
210. Aggarwal A, Liu R, Chen Y, Ralowicz AJ, Bergerson SJ, Tomaska F, Mohar B, Hanson TL, Hasseman JP, Reep D *et al*: Glutamate indicators with improved activation kinetics and localization for imaging synaptic transmission. *Nat Methods* 2023, 20(6):925-934.
211. Helassa N, Dürst CD, Coates C, Kerruth S, Arif U, Schulze C, Wiegert JS, Geeves M, Oertner TG, Török K: Ultrafast glutamate sensors resolve high-frequency release at Schaffer collateral synapses. *Proc Natl Acad Sci U S A* 2018, 115(21):5594-5599.
212. Xie Y, Chan AW, McGirr A, Xue S, Xiao D, Zeng H, Murphy TH: Resolution of High-Frequency Mesoscale Intracortical Maps Using the Genetically Encoded Glutamate Sensor iGluSnFR. *J Neurosci* 2016, 36(4):1261-1272.
213. Hordeaux J, Hinderer C, Goode T, Buza EL, Bell P, Calcedo R, Richman LK, Wilson JM: Toxicology Study of Intra-Cisterna Magna Adeno-Associated Virus 9 Expressing Iduronate-2-Sulfatase in Rhesus Macaques. *Mol Ther Methods Clin Dev* 2018, 10:68-78.
214. Xiong W, Wu DM, Xue Y, Wang SK, Chung MJ, Ji X, Rana P, Zhao SR, Mai S, Cepko CL: AAV cis-regulatory sequences are correlated with ocular toxicity. *Proc Natl Acad Sci U S A* 2019, 116(12):5785-5794.
215. Chan YK, Wang SK, Chu CJ, Copland DA, Letizia AJ, Costa Verdera H, Chiang JJ, Sethi M, Wang MK, Neidermyer WJ, Jr. *et al*: Engineering adeno-associated viral vectors to evade innate immune and inflammatory responses. *Sci Transl Med* 2021, 13(580).
216. Wang CS, Chanaday NL, Monteggia LM, Kavalali ET: Probing the segregation of evoked and spontaneous neurotransmission via photobleaching and recovery of a fluorescent glutamate sensor. *Elife* 2022, 11.
217. Matthews EA, Sun W, McMahon SM, Doengi M, Halka L, Anders S, Müller JA, Steinlein P, Vana NS, van Dyk G *et al*: Optical analysis of glutamate spread in the neuropil. *Cereb Cortex* 2022, 32(17):3669-3689.
218. Turan F, Yilmaz Ö, Schünemann L, Lindenberg TT, Kalanithy JC, Harder A, Ahmadi S, Duman T, MacDonald RB, Winter D *et al*: Effect of modulating glutamate signaling on myelinating oligodendrocytes and their development-A study in the zebrafish model. *J Neurosci Res* 2021, 99(11):2774-2792.
219. Unger F, Konnerth A, Zott B: Population imaging of synaptically released glutamate in mouse hippocampal slices. *STAR Protoc* 2021, 2(4):100877.
220. Desai NS, Rutherford LC, Turrigiano GG: BDNF regulates the intrinsic excitability of cortical neurons. *Learn Mem* 1999, 6(3):284-291.

221. Cope DW, Di Giovanni G, Fyson SJ, Orbán G, Errington AC, Lorincz ML, Gould TM, Carter DA, Crunelli V: Enhanced tonic GABAA inhibition in typical absence epilepsy. *Nat Med* 2009, 15(12):1392-1398.
222. Fling BW, Benson BL, Seidler RD: Transcallosal sensorimotor fiber tract structure-function relationships. *Hum Brain Mapp* 2013, 34(2):384-395.
223. Palmer LM, Schulz JM, Murphy SC, Ledergerber D, Murayama M, Larkum ME: The cellular basis of GABA(B)-mediated interhemispheric inhibition. *Science* 2012, 335(6071):989-993.
224. Wang Y, Chen Z, Ma G, Wang L, Liu Y, Qin M, Fei X, Wu Y, Xu M, Zhang S: A frontal transcallosal inhibition loop mediates interhemispheric balance in visuospatial processing. *Nat Commun* 2023, 14(1):5213.
225. Brickley SG, Mody I: Extrasynaptic GABA(A) receptors: their function in the CNS and implications for disease. *Neuron* 2012, 73(1):23-34.
226. Tennant KA, Taylor SL, White ER, Brown CE: Optogenetic rewiring of thalamocortical circuits to restore function in the stroke injured brain. *Nat Commun* 2017, 8:15879.
227. Tremblay R, Lee S, Rudy B: GABAergic Interneurons in the Neocortex: From Cellular Properties to Circuits. *Neuron* 2016, 91(2):260-292.
228. Pi HJ, Hangya B, Kvitsiani D, Sanders JI, Huang ZJ, Kepecs A: Cortical interneurons that specialize in disinhibitory control. *Nature* 2013, 503(7477):521-524.
229. Urban-Ciecko J, Barth AL: Somatostatin-expressing neurons in cortical networks. *Nat Rev Neurosci* 2016, 17(7):401-409.
230. Soares C, Trotter D, Longtin A, Béïque JC, Naud R: Parsing Out the Variability of Transmission at Central Synapses Using Optical Quantal Analysis. *Front Synaptic Neurosci* 2019, 11:22.
231. Hao Y, Toulmé E, König B, Rosenmund C, Plested AJR: Targeted sensors for glutamatergic neurotransmission. *Elife* 2023, 12.
232. Tian L, Hires SA, Mao T, Huber D, Chiappe ME, Chalasani SH, Petreanu L, Akerboom J, McKinney SA, Schreiter ER *et al*: Imaging neural activity in worms, flies and mice with improved GCaMP calcium indicators. *Nat Methods* 2009, 6(12):875-881.
233. Gulisano M, Broccoli V, Pardini C, Boncinelli E: Emx1 and Emx2 show different patterns of expression during proliferation and differentiation of the developing cerebral cortex in the mouse. *Eur J Neurosci* 1996, 8(5):1037-1050.
234. Guo H, Hong S, Jin XL, Chen RS, Avasthi PP, Tu YT, Ivanco TL, Li Y: Specificity and efficiency of Cre-mediated recombination in Emx1-Cre knock-in mice. *Biochem Biophys Res Commun* 2000, 273(2):661-665.
235. Lauritzen M, Dreier JP, Fabricius M, Hartings JA, Graf R, Strong AJ: Clinical relevance of cortical spreading depression in neurological disorders: migraine, malignant stroke, subarachnoid and intracranial hemorrhage, and traumatic brain injury. *J Cereb Blood Flow Metab* 2011, 31(1):17-35.
236. Empl L, Chovsepian A, Chahin M, Kan WYV, Fourneau J, Van Steenbergen V, Weidinger S, Marcantoni M, Ghanem A, Bradley P *et al*: Selective plasticity of callosal neurons in the adult contralesional cortex following murine traumatic brain injury. *Nat Commun* 2022, 13(1):2659.
237. Madisen L, Zwingman TA, Sunkin SM, Oh SW, Zariwala HA, Gu H, Ng LL, Palmiter RD, Hawrylycz MJ, Jones AR *et al*: A robust and high-throughput Cre

reporting and characterization system for the whole mouse brain. *Nat Neurosci* 2010, 13(1):133-140.
238. Armbruster M, Dulla CG, Diamond JS: Effects of fluorescent glutamate indicators on neurotransmitter diffusion and uptake. *Elife* 2020, 9.
239. Aggarwal A, Negrean A, Chen Y, Iyer R, Reep D, Liu A, Palutla A, Xie ME, MacLennan BJ, Hagihara KM *et al*: Glutamate indicators with increased sensitivity and tailored deactivation rates. *bioRxiv* 2025:2025.2003.2020.643984.

6. Acknowledgements

Although passion is important for enjoying your work, it is the people around you who can truly make the experience special.

First and foremost, I would like to express my sincere gratitude to my supervisor, Professor Nikolaus Plesnila. Working under his guidance, I have grown professionally and personally. Working in his laboratory has taught me to appreciate the value of our research and the importance of respecting and supporting my colleagues, a lesson that I will always carry with me. Thanks to Professor Plesnila's supervision, I never felt alone on my journey, a privilege not all students are fortunate enough to have.

I am also deeply grateful to Dr. Severin Filser. His mentorship has been invaluable to my development. Even though we no longer work in the same laboratory, he has continued to support me and provide invaluable advice, showing that he cared as much about my PhD as I did.

I would also like to thank the members of my TAC committee: Dr. Attardo, Dr. Balbi and Dr. Griesbeck. Their insightful feedback during our meetings helped me to design and execute my experiments to the best of my ability.

I would also like to thank the GSN for allowing me to be part of such a wonderful community. I have always felt supported by fellow students and staff equally, all of whom have approached every problem, and every day, with kindness.

I would also like to thank every member of Professor Plesnila's laboratory. Over the years, we have shared our passion for neuroscience and formed strong bonds. In particular, I would like to thank Josh for our friendship, for tackling challenging experiments together and for the unforgettable metal concerts we have enjoyed. I would also like to thank Berni for our thoughtful conversations and for always being honest with me, even when criticism was needed.

I would like to express my sincere gratitude to my colleagues at the ISD. Special thanks go to Daniel for our enjoyable experiments and the laughter we shared, not to mention his endless supply of pálinka. I would also like to thank Stefan for our engaging conversations and Philip for his wonderful sense of humor.

Finally, I would like to thank the people who have been closest to me over the years. Naima, thank you for being by my side through every moment, both joyful and challenging, and for being the best person I ever met. My heartfelt thanks also go to my family for their constant support from the very beginning of this journey, and for the steady supply of Sardinian food over the years.

Without all of you, I would not have enjoyed this journey as fully as I did.

Thank you so much!

7.Curriculum vitae

Education

01/2021- current	**Institute for Stroke and Dementia Research (ISD)** Graduate School of Systemic Neuroscience (GSN) Ludwig-Maximilians-University, Munich Laboratory of Prof. Dr. Nikolaus Plesnila PhD Student
09/2017–09/2019	**University of Cagliari, Italy** Master's degree in Neuropsychobiology grade: 110/110 cum laude
09/2014–10/2017	**University of Cagliari, Italy** Bachelor's degree in Toxicology grade: 107/110
2011	**High school diploma**

Scientific training

Since 01/2021	**Institute for Stroke and Dementia Research (ISD)** Graduate School of Systemic Neuroscience (GSN) Ludwig-Maximilians-University, Munich Laboratory of Prof. Dr. Nikolaus Plesnila PhD Student
04/2020–12/2020	**DZNE, Munich** Translational Brain Research Lab (Prof. Dr. Jochen Herms) Pre-doctoral student
09/2019–02/2020	**National institutes of Health, USA** NIAAA, Laboratory for Integrative Neuroscience (Dr. David Lovinger) Research Intern
10/2017-09/2019	**University of Cagliari, Italy** Laboratory of Electrophysiology (Prof. Enrico Sanna) Master's student

8.List of publications

Accepted publication

Jie Luo, Muge Molbay, Ying Chen, Izabela Horvath, …, **Gian Marco Calandra**, …, Hendrik Dietz & Ali Erturk. Nanocarrier imaging at single-cell resolution across entire mouse bodies with deep learning. Nat Biotechnol. 2025 Jan 14. doi: 10.1038/s41587-024-02528-1. Epub ahead of print. PMID: 39809933.

Groschup B, **Calandra GM**, Raitmayr C, Shrouder J, Llovera G, Zaki AG, Burgstaller S, Bischof H, Eroglu E, Liesz A, Malli R, Filser S, Plesnila N. Probing intracellular potassium dynamics in neurons with the genetically encoded sensor lc-LysM GEPII 1.0 in vitro and in vivo. Sci Rep. 2024 Jun 14;14(1):13753. doi: 10.1038/s41598-024-62993-1. PMID: 38877089; PMCID: PMC11178854.

Shrouder JJ, **Calandra GM**, Filser S, Varga DP, Besson-Girard S, Mamrak U, Dorok M, Bulut-Impraim B, Seker FB, Gesierich B, Laredo F, Wehn AC, Khalin I, Bayer P, Liesz A, Gokce O, Plesnila N. Continued dysfunction of capillary pericytes promotes no-reflow after experimental stroke in vivo. Brain. 2024 Mar 1;147(3):1057-1074. doi: 10.1093/brain/awad401. PMID: 38153327.

Sitzia G, Abrahao KP, Liput D, **Calandra GM**, Lovinger DM. Distinct mechanisms of CB1 and $GABA_B$ receptor presynaptic modulation of striatal indirect pathway projections to mouse globus pallidus. J Physiol. 2023 Jan;601(1):195-209. doi: 10.1113/JP283614. Epub 2022 Dec 8. PMID: 36412169; PMCID: PMC10107704.

Biggio F, Mostallino MC, Talani G, Locci V, Mostallino R, **Calandra G**, Sanna E, Biggio G. Social enrichment reverses the isolation-induced deficits of neuronal plasticity in the hippocampus of male rats. Neuropharmacology. 2019 Jun;151:45-54. doi: 10.1016/j.neuropharm.2019.03.030. Epub 2019 Mar 29. PMID: 30935859.

9.Declaration of Author Contribution

Study I: Stroke leads to contralateral neuronal suppression

Gian Marco Calandra[#]**,** Susana Valero-Freitag[#], Alessio Ricci, Severin Filser, Athanasios Lourbopoulos, Fatma B Seker, Bernhard K Groschup, Benno Gesierich, Joshua J Shrouder, Antonia Wehn, Igor Khalin, Marco Düring, Martin Dichgans, Arthur Liesz, Farida Hellal & Nikolaus Plesnila

GMC and SVF contributed equally to the study. GMC, SVF, SF, FH, and NP contributed to the study design. GMC and SF developed the in vivo functional imaging methodologies used in this manuscript. GMC, SVF, FH, BKG, AR, AW, IK, and FBS conducted the experiments, acquired and quantified the data, and performed the statistical analyses. AL, BG, and UM provided technical support. GMC, SF, and NP implemented and finalized the manuscript, which was initially drafted by SVF and FH, with input and revisions from all authors.

My contribution to this manuscript in detail: Together with Severin Filser and Nikolaus Plesnila, I designed the study and the experiments focused on in vivo functional imaging. Together with Severin Filser I established the *in vivo* functional imaging methodology in the laboratory. I performed chronic cranial window implantation, stereotactic intracortical injections of AAVs, and chronic in vivo calcium imaging under both baseline and evoked conditions. I subsequently analyzed the acquired data, building upon the study initiated by Susana Valero-Freitag. The data I contributed are presented in Figures 5 and 6. Together with Nikolaus Plesnila, I implemented the manuscript previously written by Susana Valero-Freitag.

Study II: A novel glutamate reporter line for whole-brain monitoring of glutamate dynamics

Gian Marco Calandra[#], Dániel Péter Varga[#], Paul Feyen, Francesco Gubinelli, Benedikt Wefers, Peter Makra, Joshua J Shrouder, Lena Burbulla, Wolfgang Wurst, Andrea Cattaneo, Jochen Herms, Arthur Liesz, Severin Filser & Nikolaus Plesnila

GMC and DPV contributed equally to the study. GMC, DPV, SF, and NP conceived and designed the study. BW engineered the transgenic line. GMC, DPV, PF, FG, and JS contributed to the experiments. GMC, DPV, SF, and NP drafted the manuscript.

My contribution to this manuscript in detail: Together with Daniel Peter Varga, Severin Filser, Paul Feyen, and Nikolaus Plesnila, I designed the study and the experiments. I performed in vivo multimodal imaging, including widefield mesoscale imaging and two-photon microscopy, to assess cortical glutamate dynamics in both physiological and pathophysiological contexts. Additionally, I conducted immunohistological preparations. Together with Daniel Peter Varga I performed the analysis of the acquired data. Alongside Daniel Peter Varga, Severin Filser, and Nikolaus Plesnila, I interpreted the results and contributed to drafting the manuscript. The data I contributed are presented in Figure 1, 2, 3, 4, and 5, as well as Supplementary Figure 1.

Munich, Germany

Date

Gian Marco Calandra	Prof. Dr. Nikolaus Plesnila
	(Supervisor)